UNIVERSITY OF CALIFORNIA,
IRVINE

Investigations of the Inner Dark Matter Density Profiles of Dwarf Galaxies using Multiple Chemodynamical Populations and Rotation Curves.

DISSERTATION

submitted in partial satisfaction of the requirements
for the degree of

DOCTOR OF PHILOSOPHY

in Physics

by

Andrew Bishop Pace

Dissertation Committee:
Professor Manoj Kaplinghat, Chair
Professor James S. Bullock
Professor Michael Cooper

2016

DEDICATION

To my parents, Barbara Bishop and Brent Pace

TABLE OF CONTENTS

LIST OF FIGURES

LIST OF TABLES

ACKNOWLEDGMENTS

I first and foremost want to thank my adviser, Manoj Kaplinghat.

My many collaborators have been instrumental in my pursuit of a graduate degree. I would like to acknowledge: Gregory D. Martinez, Ricardo R. Muñoz, Coral Wheeler, James Bullock, Michael Boylan-Kolchin, Sean Fillingham, Michael Cooper, Haibo Yu, Sean Tulin, Evan Kirby, and Josh Simon.

I would additionally like to thank my parents, brothers, friends, family, and fellow graduate students. Without your support this would not have been possible.

My research has been funded by NSF PHY-1214648, and a Graduate Assistance in Areas of National Need (GAANN) fellowship.

Portions of this work were published in Monthly Notices of the Royal Astronomical Society.

CURRICULUM VITAE

Andrew Bishop Pace

Education

Doctor of Philosophy in Physics **2016**
University of Califonia, Irvine *Irvine, California*

Advisor: Manoj Kaplinghat

Bachelor of Science in Physics and Astronomy **2010**
University of Califonia, Irvine *Irvine, California*

Research Experience

Graduate Research Assistant **2011–2016**
University of California, Irvine *Irvine, California*

Undergraduate Research Assistant **2009–2011**
University of California, Irvine *Irvine, California*

Teaching Experience

Teaching Assistant **2011–2014**
University of California, Irvine *Irvine, California*

COSMOS Teaching Assistant **Summers, 2014–2015**
University of California, Irvine *Irvine, California*

Awards

GAANN Fellowship **2015–2016**
AGS Travel Grant **Spring 2015**

Outreach and Service

UCI Observatory **2011–2012**
assisted with public visitor nights

COSMOS **Summers 2014 – 2015**
Science summer school for high school students

Associated Graduate Students **2015- 2016**
Council member, internal committee, and symposium committee

Physics Graduate Caucus **2012 - 2016**
physics graduate student advocacy organization

REFEREED JOURNAL PUBLICATIONS

Evidence for substructure in Ursa Minor dwarf spheroidal galaxy using a Bayesian object detection method **2014**

with Greg Martinez, Manoj Kaplinghat, and Ricardo Muñoz, MNRAS, 442, 1718,

ABSTRACT OF THE DISSERTATION

Investigations of the Inner Dark Matter Density Profiles of Dwarf Galaxies using Multiple Chemodynamical Populations and Rotation Curves.

By

Andrew Bishop Pace

Doctor of Philosophy in Physics

University of California, Irvine, 2016

Professor Manoj Kaplinghat, Chair

The Λ cold dark matter (DM) model successfully explains the distribution of large scale structure and the cosmic microwave background but, there are several problems concerning the distribution of DM on sub-galactic scales. Robust measurements of the distribution of DM in low mass dwarf galaxies are key to understand the true nature of DM. In this work, we present two new techniques for characterizing the kinematics of dispersion supported systems. The first method identifies localized kinematic substructure in line-of-sight velocity data while the second separates global stellar populations utilizing metallicty, line-of-sight velocity, and spatial information. We apply the first method to the dwarf spheroidal galaxy Ursa Minor and find two localized kinematic substructures at high significance. We present new Keck/DEIMOS spectroscopic observations of Ursa Minor, motivated by the previous detection, which form the largest spectroscopic data set of Ursa Minor. With the new data, we identify two chemodynamical stellar population at high significance with distinct kinematic, metallicity, and spatial distributions. By utilizing the dynamics of multiple stellar populations we break halo profile degeneracies and find the DM slope is more consistent with a 'cored' halo than a 'cuspy' halo. We present a complementary study comparing a large sample of literature rotation curves to dark matter halos influenced by baryonic processes. The analysis suggests that baryonic processes are an inconsistent solution to the 'core-cusp' problem.

Chapter 1

Introduction

The modern Λ cold dark matter (ΛCDM) paradigm postulates that dark matter halos are the sites of galaxy formation (White & Rees 1978; Blumenthal et al. 1984) and that the matter density of the universe is made up of roughly 25% ordinary baryonic matter and 75% dark matter (Planck Collaboration et al. 2015). This model successfully explains the distribution of matter on large scales (e.g. the 2dF Galaxy Redshift Survey; Percival et al. 2001) and the correlations of temperature fluctuations in the cosmic microwave background (Planck Collaboration et al. 2015).

The ΛCDM model provides a natural explanation for the distribution of structure on large scales but there are several unresolved problems concerning the structural properties of halos on galactic scales. Cosmological collision-less (dark matter-only) N-Body simulations produce dark matter halos that contain steep central 'cusps' ($\rho \sim r^{-1}$; for small r) (Navarro et al. 1996b, 1997; Bullock et al. 2001; Diemand et al. 2007; Macciò et al. 2007; Stadel et al. 2009; Zhao et al. 2009; Navarro et al. 2010; Klypin et al. 2011; Dutton & Macciò 2014; Klypin et al. 2016). In contrast, observations of galactic rotation curves prefer shallower central regions or 'cores' ($\rho \sim r^{\alpha}$; $\alpha > -1$) (Flores & Primack 1994; Moore 1994; Salucci & Burkert 2000; Swaters et al. 2003; Gentile et al. 2004; Spekkens et al. 2005; Simon et al. 2005; de Blok et al. 2008; Oh et al. 2011a; Adams et al.

2014; Oh et al. 2015). There is some observational evidence that galaxy clusters (Newman et al. 2013b,c) and dwarf spheroidal galaxies (Walker & Peñarrubia 2011a) contain cores. This discrepancy concerning the dark matter density inner slopes is known as the 'core-cusp' problem.

The 'too-big-to-fail' (TBTF) problem concerns the over-abundance of massive, dense (sub-)halos in dark matter-only simulations compared with the abundance of observed (satellite-)galaxies (Boylan-Kolchin et al. 2011a, 2012a). The subhalos in simulations of Milky Way sized halos are significantly more dense than their observed counterparts (Boylan-Kolchin et al. 2011a; Purcell & Zentner 2012; Jiang & van den Bosch 2015). Stated another manner, there is a lack of observed satellites with maximum dark matter circular velocities ($V_{\rm max}$) between $V_{\rm max} \sim 30 - 55\,{\rm km\,s^{-1}}$ (Boylan-Kolchin et al. 2012a; Cautun et al. 2014; Jiang & van den Bosch 2015). Similar conclusions are found for the M31 satellites (Tollerud et al. 2014), Local Group ($D \lesssim 1.2$ Mpc) objects (Kirby et al. 2014; Garrison-Kimmel et al. 2014b), and field galaxies (Ferrero et al. 2012; Miller et al. 2014; Papastergis et al. 2015; Klypin et al. 2015; Papastergis & Shankar 2015). In the local field, the TBTF problem becomes apparent at $V_{\rm max} \lesssim 25\,{\rm km\,s^{-1}}$ (Papastergis et al. 2015) even when accounting for baryonic effects (Papastergis & Shankar 2015). The inner regions of many observed galactic rotation curves contain less enclosed mass (both baryonic and dark matter) than is indicative of simulated galaxies with similar maximum observed circular velocity ($V_{\rm obs,\,max}$) (McGaugh et al. 2007; Oman et al. 2015, 2016). These discrepancies indicate that it is unclear whether the galaxies and halos are correctly matched in smaller halos.

The 'core-cusp' and TBTF problems were identified with dark matter-only simulations and the inclusion of baryonic processes is a natural solution. The formation of the galactic disk will steepen the central regions of the dark matter halo via adiabatic contraction (Blumenthal et al. 1986; Ryden & Gunn 1987; Tissera & Dominguez-Tenreiro 1998; Gnedin et al. 2004; Gustafsson et al. 2006). Supernova feedback creates cores by driving stellar winds (Navarro et al. 1996a; Gnedin & Zhao 2002; Mo & Mao 2004; Governato et al. 2010), driving the bulk motion of the gas (Mashchenko et al. 2006, 2008), and by creating fluctuations in the potential (Read & Gilmore 2005; Pontzen

& Governato 2012). The transfer of angular momentum between infalling baryonic clumps and the dark matter halo could produce shallower central regions (dynamical friction) (El-Zant et al. 2001; Tonini et al. 2006; Romano-Díaz et al. 2008; Cole et al. 2011; Del Popolo & Le Delliou 2014; Nipoti & Binney 2015). The central densities can be lowered from stellar feedback and tidal stripping (if a satellite) (Pontzen & Governato 2012; Zolotov et al. 2012; Brooks et al. 2013; Madau et al. 2014; Brooks & Zolotov 2014; Arraki et al. 2014). The precise scales and effects of these solutions are debated and other avenues have been considered.

There is a variety of work on non-standard dark matter physics that affects small scale structure without influencing large scale structure. For example, self-interacting dark matter (Spergel & Steinhardt 2000; Firmani et al. 2000) can lower the central densities and create dark matter cores (e.g. Rocha et al. 2013; Vogelsberger et al. 2014b; Kaplinghat et al. 2014; Elbert et al. 2015; Fry et al. 2015). Recent work suggests that the TBTF problem could be alleviated on the dwarf galaxy scales with warm dark matter (Lovell et al. 2012; Abazajian 2014; Lovell et al. 2014; Horiuchi et al. 2016). Warm dark matter can create cores but the particle mass ranges that create large cores also erase observed substructure (Macciò et al. 2012a). Late-decaying (Wang et al. 2014), scalar field (Robles et al. 2015), and late forming (Agarwal et al. 2015) dark matter are examples of other recently explored dark matter models with potential solutions to the small scale problems.

Accurate measurements of the distribution of dark matter in lower mass galaxies is key to distinguishing between baryonic and dark matter solutions. In this dissertation, we present new techniques to better characterize the kinematics and dynamics of dwarf galaxies (both Milky Way satellites and isolated galaxies). The local group dwarf spheroidal galaxies (dSph) are among the lowest mass dark matter halos and the earliest snapshots of structure formation. Their close proximity allows in-depth analysis of their chemical evolution, dynamics, and structure (see reviews by Mateo 1998; McConnachie 2012). The galaxies are generally divided into two groups based on their discovery: the classical and ultra-faint galaxies, where the latter were discovered post-SDSS. The dSph population of the Milky Way have a wide range of luminosities ($10^{3-7} L_{\odot}$), half-light

radii ($40-1000$ pc Mateo 1998; Simon & Geha 2007a; Martin et al. 2008; McConnachie 2012), and the dynamical mass-to-light ratios (8-4000 $M_{\odot}/L_{\odot}$ Walker et al. 2009b; Wolf et al. 2010; Simon et al. 2011; Martinez et al. 2011). The MW dSphs are highly dark matter dominated systems (Gilmore et al. 2007; Simon & Geha 2007b; Wolf et al. 2010; Kirby et al. 2014), accordingly they are excellent laboratories to distinguish between baryonic and dark matter solution to the core-cusp problem.

The MW dSphs are dispersion supported systems with roughly constant line-of-sight velocity dispersions and viral masses of order $10^{8-9} M_{\odot}$ (Walker et al. 2007). The precise shape of the mass profile is unconstrained due to unknown stellar anisotropy[1]; this effect is known as the mass-anisotropy degeneracy (Binney & Mamon 1982; Merritt 1987; Łokas 2002; Binney & Tremaine 2008). The mass-anisotropy degeneracy is inherent to modeling line-of-sight velocity data but the uncertainties are minimized at the stellar half-light radius (Walker et al. 2009c; Wolf et al. 2010). The minimization at the stellar half-light radii was recently confirmed[2] with the EAGLE simulations (Campbell et al. 2016). The degeneracy can be broken if additional data is utilized proper motions (Wilkinson et al. 2002; Strigari et al. 2007), or 3D positions (Richardson et al. 2014) or if higher order velocity moments (Merrifield & Kent 1990; Richardson & Fairbairn 2013, 2014; Jardel et al. 2013; Jardel & Gebhardt 2013; Breddels & Helmi 2013). The additional data is difficult to measure and higher order moments suffer from the unknown distribution of stellar binaries. With the standard modeling techniques utilizing 2nd order velocity moments (line-of-sight velocity dispersion), dark matter cores and cusps cannot be distinguished from one another[3].

We explore an alternative method which looks at kinematic substructure. Several dSphs show evidence of localized photometric and kinematic substructure which may be star clusters or disrupted star clusters. For example, Sextans has localized kinematically distinct population either near its

[1]The stellar orbits are unconstrained due to available measurements only in the line-of-sight direction. The data is consistent with orbits in the radial or tangential directions.

[2]Also tested in Walker & Peñarrubia (2011a); Laporte et al. (2013); Kowalczyk et al. (2013); Lyskova et al. (2015).

[3]For the Fornax dSph, there is independent argument that it contains a 'cored' dark matter halo. Fornax contains five globular clusters (Mackey & Gilmore 2003); their survival is at odds for a cuspy halo (Oh et al. 2000) and they can survive in cored dark matter halo (Goerdt et al. 2006; Sánchez-Salcedo et al. 2006).

center (Kleyna et al. 2004; Battaglia et al. 2011a) or near its core radius (Walker et al. 2006). In Ursa Minor, a secondary peak in seen in photometry although the significance is low (Irwin & Hatzidimitriou 1995; Kleyna et al. 1998; Bellazzini et al. 2002a; Palma et al. 2003a). The secondary peak has kinematics distinct from Ursa Minor (Kleyna et al. 2003). The survival of the kinematic substructure in a dSph in Ursa Minor is potential evidence that it contains a 'cored' dark matter halo (Kleyna et al. 2003; Lora et al. 2012)

Motivated by hints of localized kinematic substructure, we construct a new Bayesian methodology for detecting localized kinematic substructure in dSphs. In chapter 2, we present and test the Bayesian methodology and apply is to a Ursa Minor spectroscopic data set from Muñoz et al. (2005b). We detect two kinematic substructures at high significance and they are candidates for either disrupted star clusters or dark matter sub-subhalos. A verification of either interpretation has important implications for dark matter theory.

The stars within an individual dSph cover a wide range of metallicity, which is indicative of self-enrichment processes (Shetrone et al. 1998; Tolstoy et al. 2001; Kirby et al. 2011). All Milky Way dSphs contain an old (>10-12 Gyr) stellar population and the star formation histories of bright ($L > 10^5$) dSphs are extended or contain additional bursts (Weisz et al. 2014). For example, Carina experienced episodic star formation (Smecker-Hane et al. 1994; Hurley-Keller et al. 1998). Fornax (Buonanno et al. 1999), Leo I (Caputo et al. 1999), and Sextans (Lee et al. 2009) all have extended periods of star formation.

There is evidence of the bright dSphs containing multiple distinct chemodynamical populations [4]. The bright dSphs seem to be consistent with a scenario where a centrally concentrated metal rich population forms separately from the older, more extended and comparitively metal poor population. For example, many bright dSphs show clear evidence for spatial segregation of the red and blue horizontal branch stars (Harbeck et al. 2001; Tolstoy et al. 2004; Slater et al. 2015). With

[4]These stellar populations are global whereas the method to be presented in Chapter 2 discusses *localized* substructure.

the assembly of large high resolution spectroscopic data sets which accurately measure the both velocity and chemical abundances, multiple stellar populations have been uncovered in several dSphs (Tolstoy et al. 2004; Battaglia et al. 2006a, 2008a; Walker & Peñarrubia 2011a; Hendricks et al. 2014; Kordopatis et al. 2016).

If a dSph has multiple stellar populations, the mass measurement at each stellar half-light radii will break the mass-anisotropy (Battaglia et al. 2008a; Walker & Peñarrubia 2011a). Multi-component dSphs have been examined with a variety of methods including: two-component Spherical Jeans modeling (Ibata et al. 2006a; Battaglia et al. 2008a), estimation of the slope via mass measurement at half-light radii (Walker & Peñarrubia 2011a), the projected virial theorem (Agnello & Evans 2012; Amorisco et al. 2013), Michie-King distribution functions (Amorisco & Evans 2012a), and a generalized distribution function (Strigari et al. 2014). With the exception of Strigari et al. (2014), the previous two-component analyses infer the inner slope of the mass profile to be shallower than the expectations from ΛCDM simulations.

The stellar populations were first identified by dividing spectroscopic data sets with a metallicity cuts (Tolstoy et al. 2004; Battaglia et al. 2006a; Ibata et al. 2006a; Battaglia et al. 2008a). A better method is to consider separation of the stellar populations by constructing distributions in metallicity, spatial, and velocity space as the metallicity distributions may overlap (Walker & Peñarrubia 2011a; Amorisco & Evans 2012c). There are clear detections of multiple stellar populations in Fornax (Tolstoy et al. 2004; Battaglia et al. 2006b; Walker & Peñarrubia 2011a; Amorisco et al. 2013; Hendricks et al. 2014) and Sculptor (Battaglia et al. 2008b; Walker & Peñarrubia 2011a) dSphs. Sextans also displays signs of chemo-dynamical ordering (Bellazzini et al. 2001; Battaglia et al. 2011b). There is conflicting evidence in Carina (for: Wilkinson et al. (2006); Koch et al. (2006); Fabrizio et al. (2015); Kordopatis et al. (2016); and against: Walker & Peñarrubia (2011a)). There are similar claims in Canes Venatici I (Ibata et al. 2006b) and Boötes I (Koposov et al. 2011) not seem in other the data sets of Simon & Geha (2007a); Ural et al. (2010a) and Muñoz et al. (2006); Martin et al. (2007) respectively. With mock data, Ural et al. (2010a) argued that at least 100 stars

are required to differentiate two populations.

Ch. 3 presents a Bayesian methodology for identifying multiple stellar populations in dSph galaxies with metallicity, spatial, and line-of-sight velocity data. This includes a novel approach to Milky Way background removal and builds on previous analysis by assuming axisymmetry (instead of spherical symmetry). To complement the analysis a new spectroscopic data set in Ursa Minor is presented utilizing the Keck/DEIMOS instrument. The data set contains $\sim$ 800 Ursa Minor members with velocity and [Fe/H] measurements. We detect two global populations at high significance with distinct metallicity, spatial, and velocity distributions. We utilize the method of Walker & Peñarrubia (2011a) to find the dark matter inner slope is more consistent with a 'cored' halo than a 'cuspy' halo. We compare all dSphs with multiple populations to the predicted subhalos of Milky Way like systems. The 'too big to fail problem' is well established in this space (Boylan-Kolchin et al. 2011a, 2012a). By robustly identifying additional dSphs with multiple stellar populations, we can improve comparisons between observations and the predictions of the ΛCDM model in low mass systems.

In Chapter 4, we present a complementary analysis that tests a (stellar) mass dependent halo profile with a large literature sample of rotation curves. The sample contains over 200 galaxies but is heterogeneous in the deviation of rotation curves and stellar masses. The (stellar) mass dependent profile from Di Cintio et al. (2014b) is able to explain most rotation curves in the sample therefore solving the 'core-cusp' problem. However, the fits do not reproduce the well established stellar-mass-halo-mass relationship from abundance matching at low masses or the halo mass-concentration relation. This suggests that baryonic processes are an inconsistent solution to the 'core-cusp' problem.

Chapter 2

Evidence for substructure in Ursa Minor dwarf spheroidal galaxy using a Bayesian object detection method

Based on Pace et al. (2014)

2.1 Summary

We present a method for identifying localized secondary populations in stellar velocity data using Bayesian statistical techniques. We apply this method to the dwarf spheroidal galaxy Ursa Minor and find two secondary objects in this satellite of the Milky Way. One object is kinematically cold with a velocity dispersion of 4.25 ± 0.75 km s^{-1} and centered at $(9.1' \pm 1.5, 7.2' \pm 1.2)$ in relative RA and DEC with respect to the center of Ursa Minor. The second object has a large velocity offset of $-12.8^{+1.75}_{-1.5}$ km s^{-1} compared to Ursa Minor and centered at $(-14.0'^{+2.4}_{-5.8}, -2.5'^{+0.4}_{-1.0})$. The kinematically cold object has been found before using a smaller data set but the prediction that this cold object has a velocity dispersion larger than 2.0 km s^{-1} at 95% C.L. differs from previous

work. We use two and three component models along with the information criteria and Bayesian evidence model selection methods to argue that Ursa Minor has additional localized secondary populations. The significant probability for a large velocity dispersion in each secondary object raises the intriguing possibility that each has its own dark matter halo, that is, it is a satellite of a satellite of the Milky Way.

2.2 Additional Background

Among the classical dSphs, only Draco has a lower V-band luminosity but Ursa Minor is twice as extended as Draco (in terms of its half-light radius) (Irwin & Hatzidimitriou 1995; Palma et al. 2003a). Its observed and derived properties are summarized in Table 2.1. Ursa Minor is also likely the most massive satellite in terms of its dark matter halo, apart from the Magellanic clouds and the disrupting Sagittarius dSph. These properties make Ursa Minor an ideal target to search for substructure. The V_{max} at infall for the subhalo hosting Ursa Minor should be greater than 25 km/s but probably no larger than about 50 km/s (Boylan-Kolchin et al. 2012a) and thus we can expect Ursa Minor to have a sub-subhalo with V_{max} in the range of $8-16\,\mathrm{km\,s^{-1}}$.

Several photometric studies with different magnitude limits and overall extent observed, have reported additional localized stellar components of the stellar distribution that deviates from a smooth density profile (Olszewski & Aaronson 1985; Kleyna et al. 1998; Palma et al. 2003a), particularly near the center (Demers et al. 1995; Eskridge & Schweitzer 2001). To the northwest of the center, a secondary peak in the spatial distribution is seen in contours and isopleths (Irwin & Hatzidimitriou 1995; Kleyna et al. 1998; Bellazzini et al. 2002a; Palma et al. 2003a). However, different studies have concluded that this secondary peak is inconclusive or of low significance (Irwin & Hatzidimitriou 1995; Kleyna et al. 1998; Bellazzini et al. 2002a; Palma et al. 2003a). Smaller scale stellar substructure is, however, seen with higher significance (Eskridge & Schweitzer 2001; Bellazzini et al. 2002a). Combining proper motion information with shallow photometric data in

the central 20 arcmin of Ursa Minor, Eskridge & Schweitzer (2001) claim that the distribution of stars in Ursa Minor shows high significance for stellar substructure in clumps of $\sim 3'$ in size. Bellazzini et al. (2002a) used the presence of a secondary peak in the distribution of the distance to the 200th neighboring star to argue that the surface density profile of Ursa Minor is not smooth. In addition, the stellar density is not symmetric along the major axis with the density falling more rapidly on the Western side (Eskridge & Schweitzer 2001; Palma et al. 2003a) Statistically significant S-shaped morphology is also seen in contours of the red giant branch stars (Palma et al. 2003a). Some authors argue that these features could point towards tidal interactions (Eskridge & Schweitzer 2001; Palma et al. 2003a).

Simulations also predict that subhalos should have their own subhalos ("sub-subhalos", e.g., Shaw et al. 2007; Kuhlen et al. 2008; Springel et al. 2008; Diemand et al. 2008). While their presence in cold dark matter simulations has been verified, the mass function of these sub-subhalos hasn't been well-quantified. The subhalo mass function is seen to follow a universal profile when scaled to the virial mass of the host halo. If the sub-subhalos follow the same pattern, then we expect to see a sub-subhalo with $V_{max} \simeq 0.3 V_{max}(\text{subhalo})$ (Springel et al. 2008). We are motivated by this fact to search for stellar content that could be associated with these sub-subhalos.

Spectroscopic studies of Ursa Minor (Hargreaves et al. 1994; Armandroff et al. 1995; Kleyna et al. 2003; Wilkinson et al. 2004; Muñoz et al. 2005a) have shown a relatively flat velocity dispersion profile of $\sigma \approx 8 - 12\,\mathrm{km\,s^{-1}}$. Kleyna et al. (2003) (K03) used a two component model to test whether the second peak in photometry had a counterpart in velocity data. They found a second kinematically distinct population with $\sigma = 0.5\,\mathrm{km\,s^{-1}}$ and $\Delta\bar{v} = -1\,\mathrm{km\,s^{-1}}$. Our results lends support to this discovery by K03 but we do not agree on the magnitude of the velocity dispersion of the substructure. We discuss this in greater detail later.

K03 argued through numerical simulations that the stellar clump they discovered could survive if the dark matter halo of Ursa Minor had a large core (about 0.85 kpc) but not a cusp like the prediction for inner parts of halos of $1/r$ from CDM simulations (Navarro et al. 1997). Additional

numerical simulations including the Ursa Minor stellar clump have confirmed this result (Lora et al. 2012). Similar conclusions have been reached using the observed projected spatial distribution of the five globular clusters in Fornax dSph (Mackey & Gilmore 2003). The survival of these old globular clusters has been interpreted as evidence that the dark matter halo of Fornax may have a large core in stark contrast to the predictions of dark-matter-only CDM simulations (Goerdt et al. 2006; Sánchez-Salcedo et al. 2006; Cowsik et al. 2009; Cole et al. 2012). Thus, the study of the properties of the substructure in Ursa Minor has far reaching implications for the dark matter halo of this dSph and by extension the properties of the dark matter particle. Our study is complementary to the recent studies using the presence of multiple stellar populations in Fornax and Sculptor that also seem to point towards a cored dark matter density profile (Battaglia et al. 2008b; Walker & Peñarrubia 2011b; Amorisco & Evans 2012b).

Current methods for finding kinematic substructure in the dSphs has relied on likelihood comparison parameter tests (Kleyna et al. 2003; Ural et al. 2010b), non-parametric Nadaraya-Watson estimator (Walker et al. 2006), or metalicity cuts and kinematics (Battaglia et al. 2011a), but not Bayesian methods. Hobson & McLachlan (2003) presented a Bayesian method for finding objects in noisy data. The object detection method is able to find two or more objects using only a two component model in photometric data. This method can be extended to include spectroscopic line-of-sight velocity data to search for objects using kinematics, as well as structural properties. We apply this method to Ursa Minor to search for counterparts to stellar substructure (Irwin & Hatzidimitriou 1995; Kleyna et al. 1998) and the kinematically cold feature found by K03. In the next subsection we discuss the localized velocity dispersions and average velocities. In section 2, we present the object detection method and model selection techniques used to quantify whether detection is real or not. In section 3, we present our results and access the significance of them. In section 4, we discuss the implications of localized substructures and we conclude in section 5.

Table 2.1: Observed and derived properties of Ursa Minor.

Parameter	Value
Distance [1]	77 ± 4 kpc
Luminosity [1]	$3.9^{+1.7}_{-1.3} \times 10^5 \mathrm{L}_{\odot,\mathrm{V}}$
Core radius [1]	$17.9' \pm 2.1$
Tidal radius [1]	$77.9' \pm 8.9$
Half-light radius [1]	0.445 ± 0.044 kpc
Deprojected half-light radius [1] ($r_{1/2}$)	0.588 ± 0.058 kpc
Average velocity dispersion [2]	11.61 ± 0.63 km s^{-1}
Mean velocity [2]	-247 ± 0.8 km s^{-1}
Dynamical mass within $r_{1/2}$ [1]	$5.56^{+0.79}_{-0.72} \times 10^7 M_\odot$
Mass-to-light ratio within $r_{1/2}$ [1]	$290^{+140}_{-90} M_\odot/\mathrm{L}_\odot$
Ellipticity [3]	0.56 ± 0.05
Center (J2000.0) [4]	$(15^h09^m10^s.2, 67°12'52'')$
Position angle [5]	49.4°

Note: References are as follows 1. Wolf et al. (2010) and references therein 2. This paper 3. Mateo (1998) 4. Kleyna et al. (2003) 5. Kleyna et al. (1998)

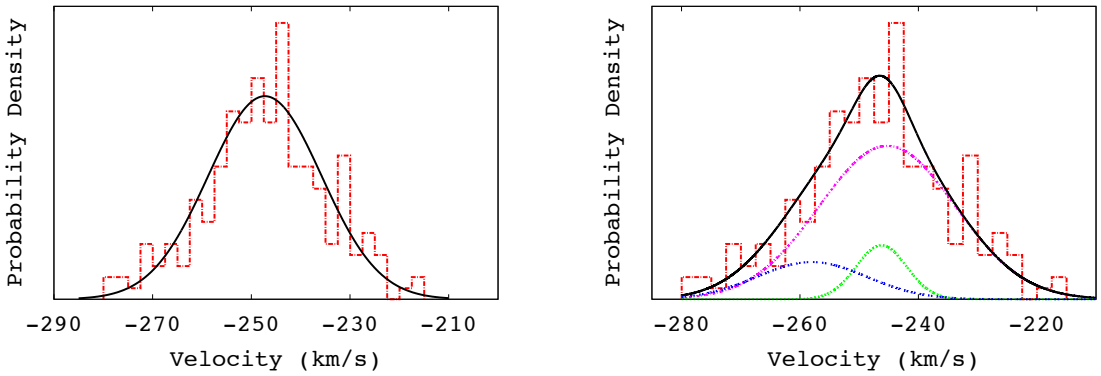

Figure 2.1: The binned line-of-sight velocity data (red dashed) in Ursa Minor. *Right:* Over-plotted is the most probable Gaussian with $\sigma = 11.51$ and an $\bar{\mathrm{v}} = -247.25$ (black solid) from the null model (single Gaussian component). *Left:* The line-of-sight velocity distributions of the secondary objects and primary populations.The lines correspond to the velocity dispersions of different populations found with the Bayesian object detection method; velocity offset object (blue dot-dot-space), cold object (green dotted), primary distribution (purple dot-dash), and the total (black solid). Each component is weighted by its average number of stars found using the Bayesian object detection method. When spatial information is taken into account, the additional kinematic components provide a better fit to the Ursa Minor data.

2.2.1 Data and Motivation for more Complex Models

The spectroscopic data we used contains 212 Ursa Minor member stars (Muñoz et al. 2005a); the sample that K03 used to discover the cold feature contained 134 stars. In Figure 2.1, we show the line-of-sight velocities binned with the best fit single component Gaussian (right) and the combined fit from our object detection model (left). When positional information is included in addition to the velocity information, both models have comparable χ^2. The mean, dispersion, and positional information of these Gaussian distributions were derived from our Bayesian object detection that is the subject of this paper. As a prelude to our final results, we note that the centers of all three populations (the primary and two secondaries) found through the object detection method are spatially segregated.

Before we develop the Bayesian methodology and model comparison methods to show the significance of (or lack thereof), we would like to dissect the data to see if secondary populations are visible as strong local deviations in either mean velocity or velocity dispersion. To this end, we grid a $50' \times 30'$ region around the center of Ursa Minor finely and for each grid point, we find the average velocity $\overline{\mathrm{v}}$ and velocity dispersion σ in a $5' \times 5'$ bin using the expectation-maximization (EM) method (see Equations 12b and 13 of Walker et al. (2009a)). We disregard grid points where there are fewer than 7 stars in the bin. We have plotted the smoothed σ and $\overline{\mathrm{v}}$ maps created using this method in Figure 2.2. The velocity dispersion map is the upper left panel and the average velocity map is the upper right panel. The data is rotated such that the major axis is aligned with the abscissa ($\theta = 49.4^\circ$, see Table 1 for the photometric properties of Ursa Minor we use). There are two interesting features evident: in the σ map, roughly centered at $(11', -4')$, the σ drops below $6\,\mathrm{km\,s^{-1}}$ whereas the globally, $\sigma = 11.5\,\mathrm{km\,s^{-1}}$, and in the $\overline{\mathrm{v}}$ map centered at $(-13', 6')$, the $\overline{\mathrm{v}}$ evidently differs from Ursa Minor's overall average ($\Delta|\overline{\mathrm{v}}| > 10\ \mathrm{km\,s^{-1}}$). We have also plotted the number density (lower left panel) and the positions of the stars (lower right panel) in Figure 2.2 to and σ maps are that the kinematic peculiarities are not artifacts due to a low number of stars The number density map is created the same way as the $\overline{\mathrm{v}}$ and σ maps and it shows that both features

are in regions that are reasonably sampled. In the plot with the positions of the stars, we have also indicated the most probable locations for the centers and the extent of the the two features as found by our Bayesian object detection method. We caution the reader that the plotted extents (tidal radii) of the these features have large error bars see Table 2.2).

The center of the dip in σ (upper left panel of Figure 2.2) is near the spectroscopic feature found by K03 and the secondary density peak seen in the photometry by several authors (Irwin & Hatzidimitriou 1995; Kleyna et al. 1998; Bellazzini et al. 2002a; Palma et al. 2003a). The average velocity feature we see does not correspond to any previous noted photometry or kinematic features. However, we note that the stellar isodensity contours of Ursa Minor are significantly asymmetric (Kleyna et al. 1998; Palma et al. 2003a) and could hide both features.

We now turn to describing our Bayesian object detection method for finding secondary objects and model selection methods for assessing their significance.

2.3 Methodology: Theory

This paper has two primary objectives: to present a statistical methodology for detecting discrete features within a kinematic data set and apply this methodology to the Milky Way satellite galaxy Ursa Minor. In this section we detail the statistical techniques used to detect kinematic objects within the Ursa Minor data set. The pertinent question we are addressing is whether statistically distinct kinematic objects can be detected within a galaxy's stellar line-of-sight kinematic data and, if such an object is detected, how certain can we be that this object is an actual physical attribute of the system. Thus we require that any methodology used to detect multiple smaller composite objects within the kinematic data set have two important properties. First, any proposed algorithm must be able to discern an unspecified numbers of statistically separable features within the a galaxy's kinematic data set. And second, this methodology must allow for some kind of

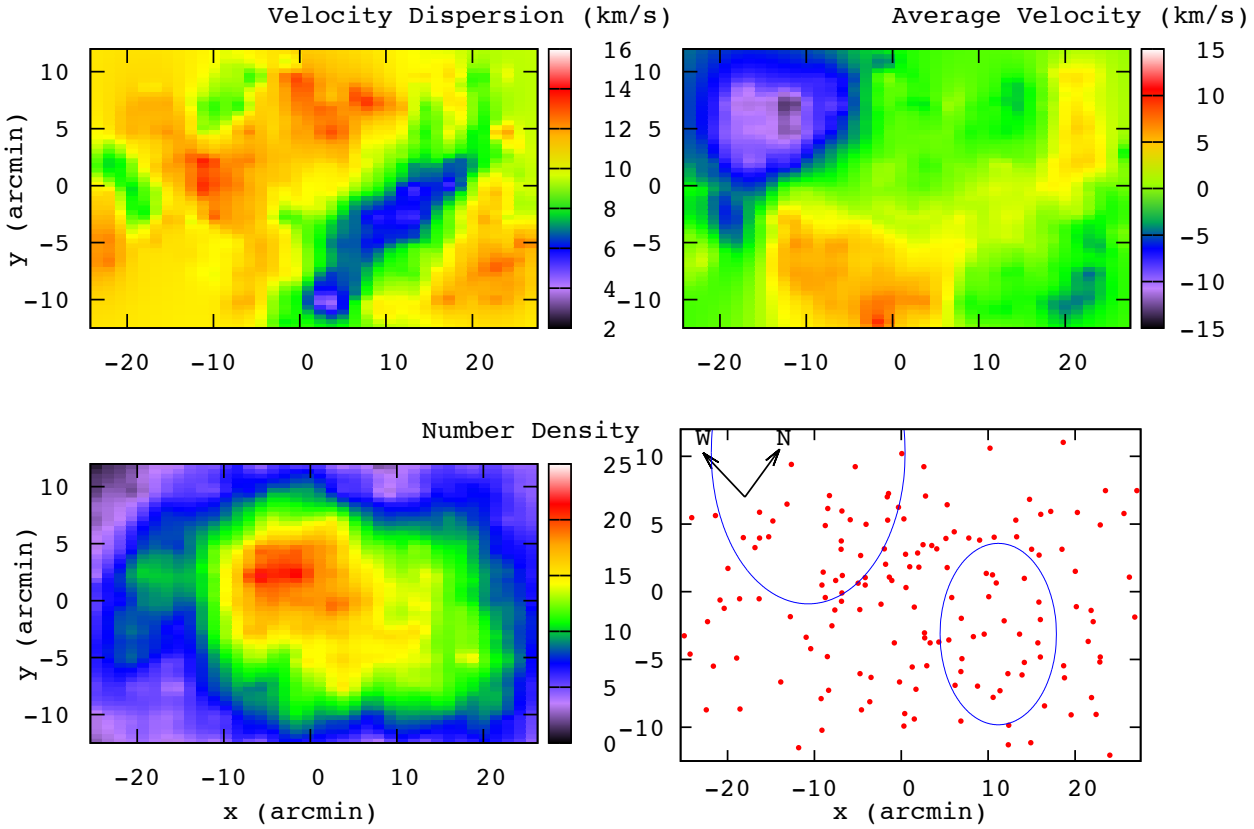

Figure 2.2: The local kinematics of Ursa Minor using the Muñoz et al. (2005a) data set. *Upper Left:* A map of the velocity dispersion of Ursa Minor. A portion of the lower right quadrant drops below 6 $\mathrm{km\,s^{-1}}$ while the rest of the galaxy is relatively uniform. *Upper Right:* The average velocity of Ursa Minor found concurrently with the velocity dispersion. In the upper left quadrant the deviation $\Delta\bar{v} > 10-15$ $\mathrm{km\,s^{-1}}$ relative to Ursa Minor while the rest of the galaxy does not differ more than 5 $\mathrm{km\,s^{-1}}$. To make the contour plots, the velocity dispersion and the average velocity were found within a $5' \times 5'$ bin ($5' \simeq 110$ pc for a distance of 77 kpc). *Lower Left:* The stellar density profile of the stars in the Muñoz et al. (2005a) data set. *Lower Right:* The most probable locations and sizes (tidal radii) of the two objects using the Bayesian object detection method in Ursa Minor. Both of these locations correspond to the deviations seen in the average velocity and velocity dispersion maps. The coordinate system used here is such that the x-axis lines up with the major axis which has a position angle of 49.4° (Kleyna et al. 1998). The adopted center for Ursa Minor was RA = $15^h09^m10^s.2$, DEC = $+67°12'52$" (J2000.0) (K03). For the entire sample, we obtain a mean velocity $\bar{v} = -247.25$ $\mathrm{km\,s^{-1}}$ and velocity dispersion $\sigma = 11.51$ $\mathrm{km\,s^{-1}}$.

determination of the significance of a proposed object detection.

To meet these criteria, we employ a Bayesian object detection technique first introduced by Hobson & McLachlan (2003). In our implementation, the data distribution is modeled with two separate components: a background distribution referred to as the primary distribution, in our case, the Ursa Minor dSph ($\mathscr{P}_p$), and a 'secondary' distribution ($\mathscr{P}_s$) which is interpreted here as a feature or object of the Ursa Minor data set. Thus, the actual distribution is of the form:

$$\mathscr{P}(d_i|\mathscr{M}) = (1-F)\,\mathscr{P}_p(d_i|\mathscr{M}_p) + F\,\mathscr{P}_s(d_i|\mathscr{M}_s) \tag{2.1}$$

where F is the total fraction of stars in the secondary population, d_i represents an individual element of the Ursa Minor data set $\mathscr{D}$ ($\mathscr{D} = \{d_i\}$), and $\mathscr{M}$ denotes the parameter set of the respective distribution's model. A major benefit of this type of analysis is that data sets with multiple features will cause the secondary population parameter posteriors to become multi-modal where each individual mode represents a unique feature. This enables us to search for an arbitrary number of objects without requiring an overly complicated probability distribution. In addition, the local Bayesian evidences of each mode can be used as a selection criterion. The evidence $Z \equiv \mathscr{P}(\mathscr{D}|H)$ is equal to the integral of the product of the likelihood, $\mathscr{L}(\mathscr{M}) \equiv \mathscr{P}(\mathscr{D}|\mathscr{M},H) = \prod_i \mathscr{P}(d_i|\mathscr{M},H)$, and prior probability, $Pr(\mathscr{M}) \equiv \mathscr{P}(\mathscr{M}|H)$:

$$\mathscr{P}(\mathscr{D}|H) = Z = \int \mathscr{L}(\mathscr{M}) Pr(\mathscr{M}) d\mathscr{M} \quad . \tag{2.2}$$

The evidence is the average likelihood value before the input of data. Here, the probability density of the parameter set $\mathscr{M}$ (*i.e.*, $\mathscr{P}(\mathscr{M}|\mathscr{D},H)$), or posterior, is related to the evidence by the Bayes' theorem

$$\mathscr{P}(\mathscr{M}|\mathscr{D},H) = \frac{\mathscr{P}(\mathscr{D}|\mathscr{M},H) Pr(\mathscr{M})}{Z} \quad , \tag{2.3}$$

Later, we use the evidence as a criterion for selecting between two models, or hypotheses (H): One

that assumes a 'secondary' feature represented by equation 2.1 (H_1) and another 'null hypothesis' that only assumes the background distribution $\mathscr{P}_p$ (H_0). In section 2.3.2 we use both models directly in the ratio of evidences, or Bayes factor, and indirectly in the determination of the the Kullback-Leibler divergence, a quantity the quantifies the amount of information gained from the assumption of one hypothesis over another. Through a large set of Monte Carlo simulations, these criteria are then used to derive confidence levels on the exclusion of the null hypothesis.

To calculate the evidence and sample the posterior space, a Bayesian multi-nested sampling technique was utilized (Skilling 2004a; Feroz & Hobson 2008; Feroz et al. 2009). The nested sampling method calculates the evidence of a model and as a by product of the computation the posterior is also evaluated. The algorithm transforms the multi-dimensional evidence integral Equation 2.2, through the 'prior volume' X ($dX = \pi(\theta)d^D\theta$), into a one-dimensional integral. If the inverse of the prior volume exists and is a monotonically decreasing function of the 'prior volume', the evidence integral can be transformed into $Z = \int_0^1 \mathscr{L}(X)dX$. This integral can be evaluated by sampling the likelihood in a decreasing sequence of prior volumes. The multi-nest algorithm breaks the prior volume into multi-dimensional ellipsoids which helps sample degenerate parameter spaces and speeds up computation. This sampling algorithm possesses all the capabilities required for this project: multi-modal posteriors can be explored efficiently, and the evidence is inherently evaluated (For a more in-depth explanation of the method see Feroz & Hobson (2008); Feroz et al. (2009)).

2.3.1 Likelihood

Our methodology utilizes a two component probability distribution similar to that in the K03 paper (also see Martinez et al. (2011)). We base the 'primary' (p) and 'secondary' (s) probability distributions on a Gaussian with mean velocity $\overline{v}_{p,s}$, using the velocity errors ε_i, and the assumption of

a constant velocity dispersion, $\sigma_{p,s}$, as the spread:

$$\mathscr{P}_{p,s}(v_i, R_i|\mathscr{M}_{p,s}) = \frac{\exp\left[-\frac{1}{2}\frac{(v_i-\bar{v}_{p,s})^2}{(\sigma_{p,s}^2+\varepsilon_i^2)}\right]}{\sqrt{2\pi(\sigma_{p,s}^2+\varepsilon_i^2)}}\frac{\rho_{p,s}(R_i)}{N_{p,s}} \tag{2.4}$$

Here, $\rho_{p,s}(R)$ is the 2-D stellar number density normalized to the total number in the population ($N_{p,s}$).

Unfortunately, because of spatial selection biases, $\rho_{p,s}(R)$ is difficult to model. To account for this uncertainty, we consider only the 'conditional' likelihood (see Martinez et al. (2011) for details):

$$\mathscr{P}_{p,s}(v_i|R_i, \mathscr{M}) = \mathscr{P}_{p,s}(v_i, R_i|\mathscr{M})/(\rho_{p,s}(R_i)/N_{p,s}). \tag{2.5}$$

With this, equation 2.1 becomes:

$$\mathscr{P}(v_i|R_i, \mathscr{M}) = (1-f(R_i))\mathscr{P}_p(v_i|R_i, \mathscr{M}_p) + f(R_i)\mathscr{P}_s(v_i|R_i, \mathscr{M}_s) \tag{2.6}$$

where $f(R_i)$ is now the 'local' fraction of stars in the secondary population defined by

$$f(R_i) = \frac{I_s(R_i|\mathscr{M}_s)}{I_s(R_i|\mathscr{M}_s) + \alpha I_p(R_i|\mathscr{M}_p)} \tag{2.7}$$

Here, we have introduced the variable $\alpha = N_s/N_p$. Instead of varying α directly, we found that, in some instances, using total fraction as a free parameter simplifies the analysis [1]:

$$F_{total} = \frac{\int I_s \,\mathrm{d}x\mathrm{d}y}{\int I_s \,\mathrm{d}x\mathrm{d}y + \alpha \int I_p \,\mathrm{d}x\mathrm{d}y}. \tag{2.8}$$

For the primary population, we assume a 2-D king stellar density profile whose parameters are

[1] We also tried a constant fraction within the location of the second population. In all three parameterizations of α the same objects are found.

fixed to the observed photometry. The secondary object's density profile is taken to be a top-hat[2]. Our Bayesian object detection model constituted of 8 parameters: 2 primary kinematic parameters, 2 secondary kinematic parameters, the x and y center and tidal radius for the secondary population and the total fraction. The parameters, priors, and posteriors are listed in the first row of Table 2.2.

2.3.2 Model Selection

Even with accurate probability density modeling and thorough parameter space exploration, any object detection methodology will have fairly limited capabilities if the significance of a detection cannot be determined. In this section, we introduce three commonly used model selection techniques to quantitatively derive confidence levels between the multiple component and single component (null model) hypotheses. The techniques used are: theBayes Factor (B_{01} or $\ln B_{01}$), a direct calculation of the Kullback-Leibler divergence (D_{KL}) (Kullback & Leibler 1951), and Deviance information criterion (DIC) (Spiegelhalter et al. 2002) [3]. For a general review of of model selection in cosmology, particularly Bayesian methods, see Liddle et al. (2006); Trotta (2008). For a review of the use of information criterion in cosmology see Takeuchi (2000); Liddle (2007).

The Bayes factor is the ratio of the evidence of two models or hypotheses. It is defined as:

$$B_{01} = \frac{\mathscr{P}(\mathscr{D}|H_1)}{\mathscr{P}(\mathscr{D}|H_0)}. \tag{2.9}$$

where H_0 and H_1 are the two different hypotheses. The general rule of thumb is that $B_{01} > 1$ favors hypothesis H_1 and $B_{01} < 1$ favors hypothesis H_0. The significance of B_{01} is usually computed as

[2] Additional stellar profiles were used for the secondary population including a King, and Plummer profile. Both objects were still detected. The scale radii for the King and Plummer stellar profiles were unconstrained.

[3] Two other common information criterion are the Akaike information criterion (AIC) (Akaike 1974) and the Bayesian information criterion (BIC). These information criterion are Gaussian approximations to the D_{KL} and Bayes factor respectively. We do not use these as we have a direct calculation of them.

Parameter	Type	Prior (Units)	Cold Spot	Velocity Offset
Model parameters from Bayesian object detection method				
σ_s	flat	Cuts 1/2 (see caption)	$3.5^{+1.75}_{-2.25}$	$8.75^{+1.5}_{-2.25}$
σ_p	flat	0 to 20 $\mathrm{km\,s^{-1}}$	11.75 ± 0.5	10.75 ± 0.5
$\overline{\mathrm{v}}_s$	flat	Cuts 1/2 (see caption)	$-246.75^{+1.75}_{-2.0}$	$-258.75^{+2.0}_{-1.75}$
$\overline{\mathrm{v}}_p$	flat	-242 to -252 $\mathrm{km\,s^{-1}}$	-247.5 ± 0.75	-245.25 ± 0.75
x_{cen}	flat	-0.6 to 0.6 kpc	$0.25^{+0.04}_{-0.06}$	-0.24 ± 0.09
y_{cen}	flat	-0.4 to 0.4 kpc	$-0.07^{+0.03}_{-0.07}$	0.23 ± 0.02
r_{tidal}	flat in $\log_{10}$	10 to 300 (pc)	151^{+53}_{-28}	251^{+24}_{-22}
F_{total}	flat in $\log_{10}$	10^{-5} to 1	$0.79^{+0.21}_{-0.16}$	$0.32^{+0.47}_{-0.26}$
Secondary Population Model Parameters from simultaneous 3-component modeling				
x_{cen}	flat	-0.24 ± 0.1 kpc	0.26 ± 0.02	$-0.23^{+0.095}_{-0.035}$
y_{cen}	flat	0.23 ± 0.1 kpc	-0.07 ± 0.01	0.22 ± 0.02
r_{tidal}	flat in $\log_{10}$	10 to 300 pc	151^{+151}_{-10}	269^{+26}_{-24}
σ_s	flat	Cuts 1/2 (see caption)	4.25 ± 0.75	9.25 ± 1.25
σ_p	flat	0 to 20 $\mathrm{km\,s^{-1}}$	11.5 ± 0.5	11.5 ± 0.5
$\overline{\mathrm{v}}_s$	flat	Cuts 1/2 (see caption)	-246.25 ± 1.0	-258.0 ± 1.5
$\overline{\mathrm{v}}_p$	flat	-252 to -242 $\mathrm{km\,s^{-1}}$	$-245.25^{+0.75}_{-0.5}$	$-245.25^{+0.75}_{-0.5}$
f_{local}	derived	–	70% (15.8/22.5)	85 % (27.0/31.6)

Table 2.2: Parameters, Priors, and Posteriors. σ_s and σ_p are the velocity dispersions of the secondary and primary populations. $\overline{\mathrm{v}}_s$ and $\overline{\mathrm{v}}_p$ are the average velocities of the secondary and primary populations. x_{cen} and y_{cen} refer to the x and y centers of the secondary population. Note that the data was rotated such that the x axis and the major axis are parallel. r_{tidal} is the tidal radius in a top hat model for the secondary population. F_{total} is the ratio of stars in the secondary population to the total population. For the first section, the 4th and 5th columns denote the values when detecting the two objects individually. The two cuts indicated in the table as "Cuts 1 and 2" are defined as follows. Cut 1 is $0 \leq \sigma \leq 10\,\mathrm{km\,s^{-1}}$ and $-252 \leq \overline{\mathrm{v}} \leq -242\,\mathrm{km\,s^{-1}}$ to find the cold spot object. Cut 2 is $0 \leq \sigma \leq 20\,\mathrm{km\,s^{-1}}$ and $-267 \leq \overline{\mathrm{v}} \leq -237\,\mathrm{km\,s^{-1}}$ to find the velocity offset object. In the second section, the 4th and 5th column denote the values calculated for the two objects simultaneously using a 3-component model. The coordinates x_{cen} and y_{cen} of the objects were only allowed to vary within ± 0.1kpc of the value obtained from the Bayesian object detection method. f_{local} is the weighted average fraction of secondary population stars in each secondary object's location.

$\ln B_{01}$ with $\ln B_{01} < 1$, $1 < \ln B_{01} < 2.5$, $2.5 < \ln B_{01} < 5, \ln B_{01} > 5$ corresponding to inconclusive, weak, moderate and strong evidence, respectively, in favor of hypothesis H_1 (as advocated by Trotta (2008)). The Bayes factor has the advantage that it is an output of our sampling algorithm but, it inherently penalizes the model with a larger parameter space. This penalization encodes Occam's razor in the Bayes factor.

The D_{KL} represents the information gain by switching from the posterior distribution of H_0 to the posterior distribution of H_1. The D_{KL} is written:

$$D_{KL}(\mathscr{P}_1, \mathscr{P}_0) = \int \ln\left(\frac{\mathscr{P}(\mathscr{M}|\mathscr{D}, H_1)}{\mathscr{P}(\mathscr{M}|\mathscr{D}, H_0)}\right) \mathscr{P}(\mathscr{M}|\mathscr{D}, H_1) d\mathscr{M} \quad , \tag{2.10}$$

where $\mathscr{P}_0, \mathscr{P}_1$ are the posterior distributions under hypotheses H_0 and H_1, respectively.

The DIC (Spiegelhalter et al. 2002), is related to the amount of information gained through the full posterior as opposed to assuming only the prior probability distribution (i.e., $D_{KL}(\mathscr{P}, \Pr)$):

$$\mathrm{DIC} \equiv -2\widehat{D_{KL}}(\mathscr{P}, \Pr) + 2\mathscr{C}_b \tag{2.11}$$

where $\mathscr{C}_b \equiv \overline{\chi^2(\mathscr{M})} - \chi^2(\overline{\mathscr{M}})$, $\chi^2 \equiv -2\ln(\mathscr{L})$, and $\widehat{D_{KL}}(\mathscr{P}, \Pr) \equiv \ln(\mathscr{L}(\overline{\mathscr{M}})) - \ln(Z)$ (Trotta 2008).

We also introduce the total membership as a physically interpretable model selection method tailored for the problem at hand. The membership that a star is part of the secondary population is derived from the posterior by the ratio of the secondary likelihood to total likelihood (Martinez et al. 2011). For the ith star, the membership is:

$$m_i = \frac{f(R_i)\mathscr{P}_s(v_i|R_i, \mathscr{M}_s)}{(1 - f(R_i))\mathscr{P}_p(v_i|R_i, \mathscr{M}_p) + f(R_i)\mathscr{P}_s(v_i|R_i, \mathscr{M}_s)} \tag{2.12}$$

As the membership is derived from the posterior, each star will have its own probability distribution. Our data set contains 212 stars and so to simplify the analysis we use the average membership

of each star's probability distribution.

A global model selection parameter, the total average membership, can be found and interpreted as the average number of stars contained in the secondary population. We find (see Figure 2.3-2.4) that the membership correlates with each of the other model selection parameters (i.e., a model with high evidence will have high membership and a model with low evidence will have low membership).

2.3.3 Testing the Method with Mock Data

We created 100 mock data sets containing a second population to test whether known secondary objects could be detected using our object detection method. The second populations were located at either (0.2, -0.1) or (-0.23, 0.24) kpc (roughly the locations of the cold and velocity offset objects). The kinematic and structural parameters of this second population were selected to mimic the cold and velocity offset objects. The positions and velocity errors from the Ursa Minor data set were used to simulate observational errors. To pick which population a star is assigned to, the local fraction was found via Equation 2.8 and membership was randomly assigned with the second population weighted by the local fraction. The primary population parameters were the best fit values from Ursa Minor photometry and the kinematics of the entire sample: $r_{tidal} = 1.745$ kpc, $r_{core} = 0.401$ kpc, ellipticity $\varepsilon_p = 0.56$, $\sigma = 11.5$ $\mathrm{km\,s^{-1}}$, and $\overline{\mathrm{v}} = -247$ $\mathrm{km\,s^{-1}}$. The second population's base parameters were: $\varepsilon_s = 0$, $\theta_s = 0.0$, $F_{total} = 60/212$, $r_{core} = 0.05$kpc, $\Delta\overline{\mathrm{v}}_s = 0$ $\mathrm{km\,s^{-1}}$, $\sigma = 4\,\mathrm{km\,s^{-1}}$, $r_{tidal} = 0.15$kpc for (0.2, -0.1) location. For the (-0.23, 0.24) location, we used a slightly larger value for tidal radius, $r_{tidal} = 0.25$kpc. We note that both populations were created assuming an underlying King profile but the object detection used a top-hat model when finding the second population, identically to how the objects were found in the actual data. Each individual mock data set had 1-3 secondary parameters that deviated from the base parameters to test how each parameter affected the detection. In some sets we did not expect to find the secondary

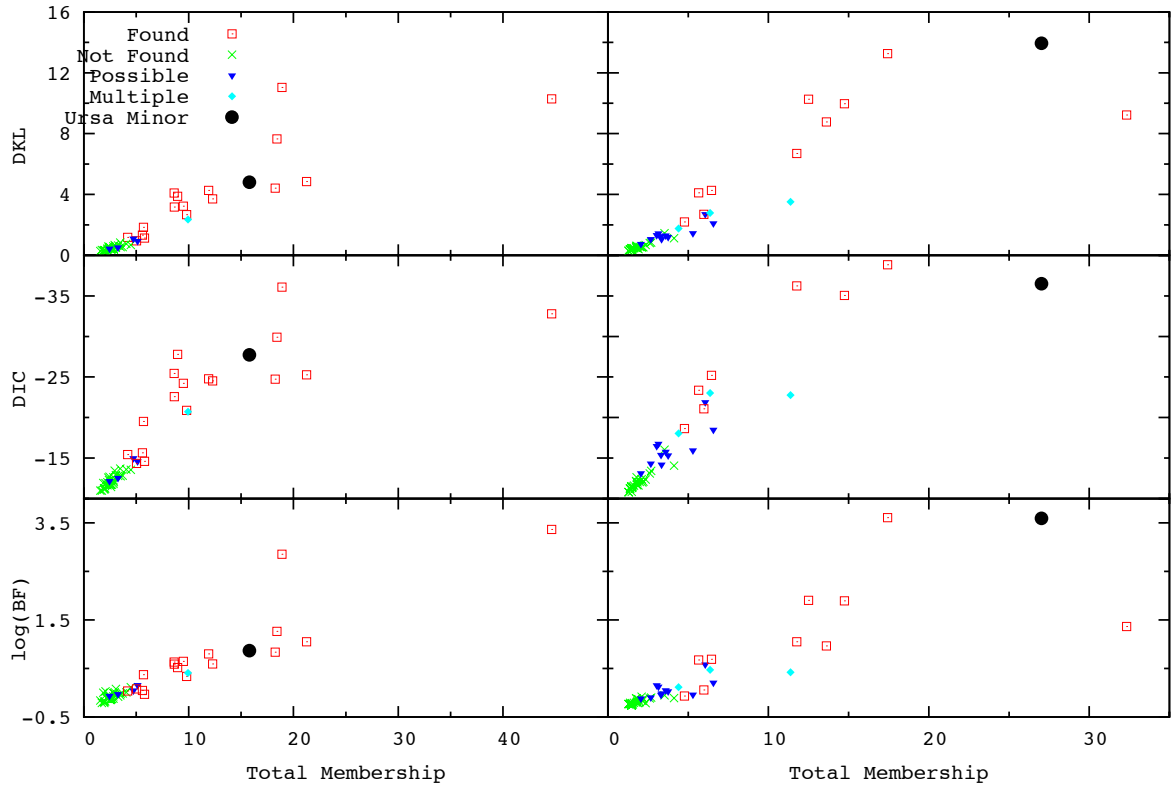

Figure 2.3: Model selection tests using D_{KL}, DIC, $\log BF = \ln \mathrm{B}_{01}$ (cf., §2.3.2 for definitions) for 50 mock data sets located at (0.2, -0.1). Also shown for comparison are the results for the actual Ursa Minor data set. A more negative DIC favors the secondary object hypothesis more strongly, while the same is true for larger values of D_{KL} and Bayes factor. **Left column**: Figures in column 1 show the results of the analysis of the mock data sets in exactly the same way as the real data set was analyzed to look for the cold object with cuts on mean velocity and dispersion given by $0 \leq \sigma \leq 10\,\mathrm{km\,s^{-1}}$ and $-252 \leq \bar{\mathrm{v}} \leq -242\,\mathrm{km\,s^{-1}}$ (Cut 1). The top panel shows D_{KL}, the middle panel DIC and the bottom panel the logarithm of the Bayes factor (written in the text as $\ln B_{01}$. Mock data sets that had second populations with significant differences in their kinematics with respect to the background population were found with our object detection method. The symbols are labeled/colored according to whether the x and y posterior is peaked compared to the background around the locations of the secondary populations: peaked/found (red square), not peaked/ not found (green x), possible peaks (blue triangle) and multiple peaks (light blue diamond). The results for the actual Ursa Minor data set is shown as filled black circle. **Right column**: This panel has the same symbols and colors as the left most column. The difference here is that the velocity cuts used are broader (and the same as that used to find the velocity offset object). The cuts are $0 \leq \sigma \leq 20\,\mathrm{km\,s^{-1}}$ and $-267 \leq \bar{\mathrm{v}} \leq -237\,\mathrm{km\,s^{-1}}$ (Cut 2).

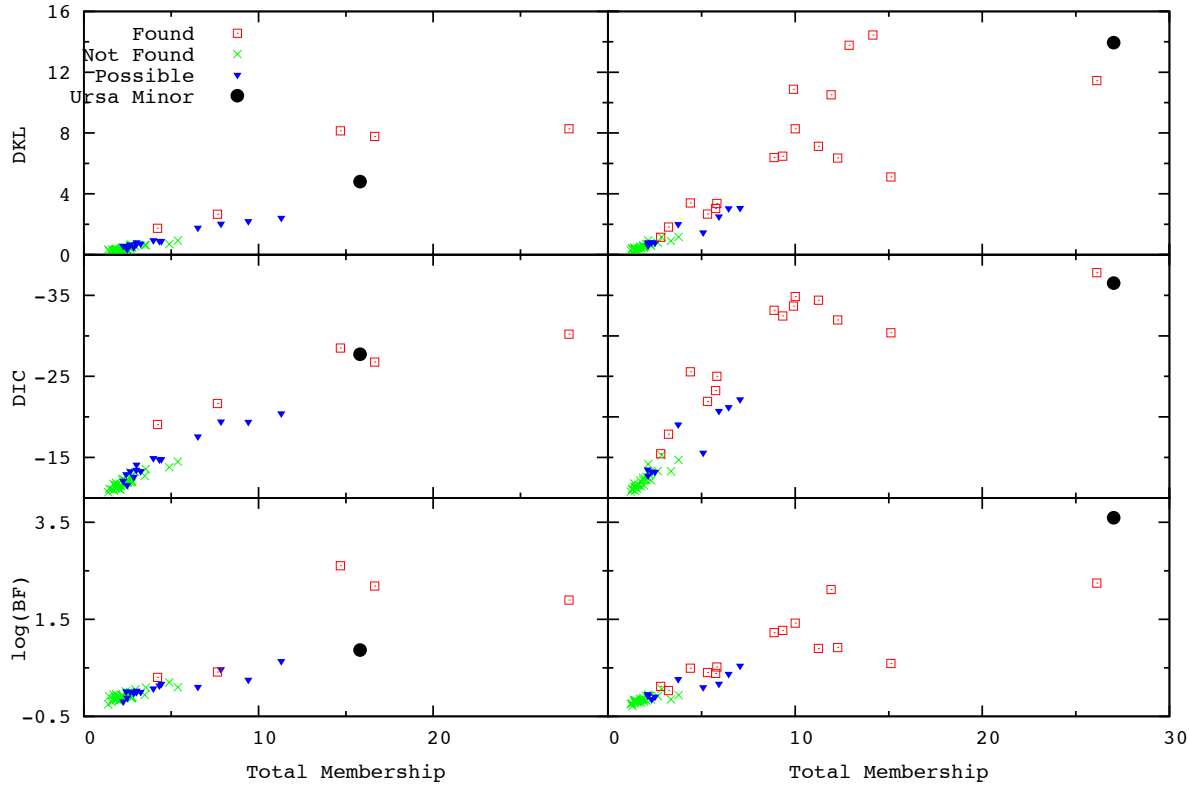

Figure 2.4: Model selection tests using D_{KL}, DIC, $\ln B_{01}$ for 50 mock sets located at (-0.24, 0.23) and the Ursa Minor data. The layout is the same as Figure 2.3. The third column from left displays the results from the scrambled mock data sets instead of the null hypothesis mock data sets plotted in Figure 2.3.

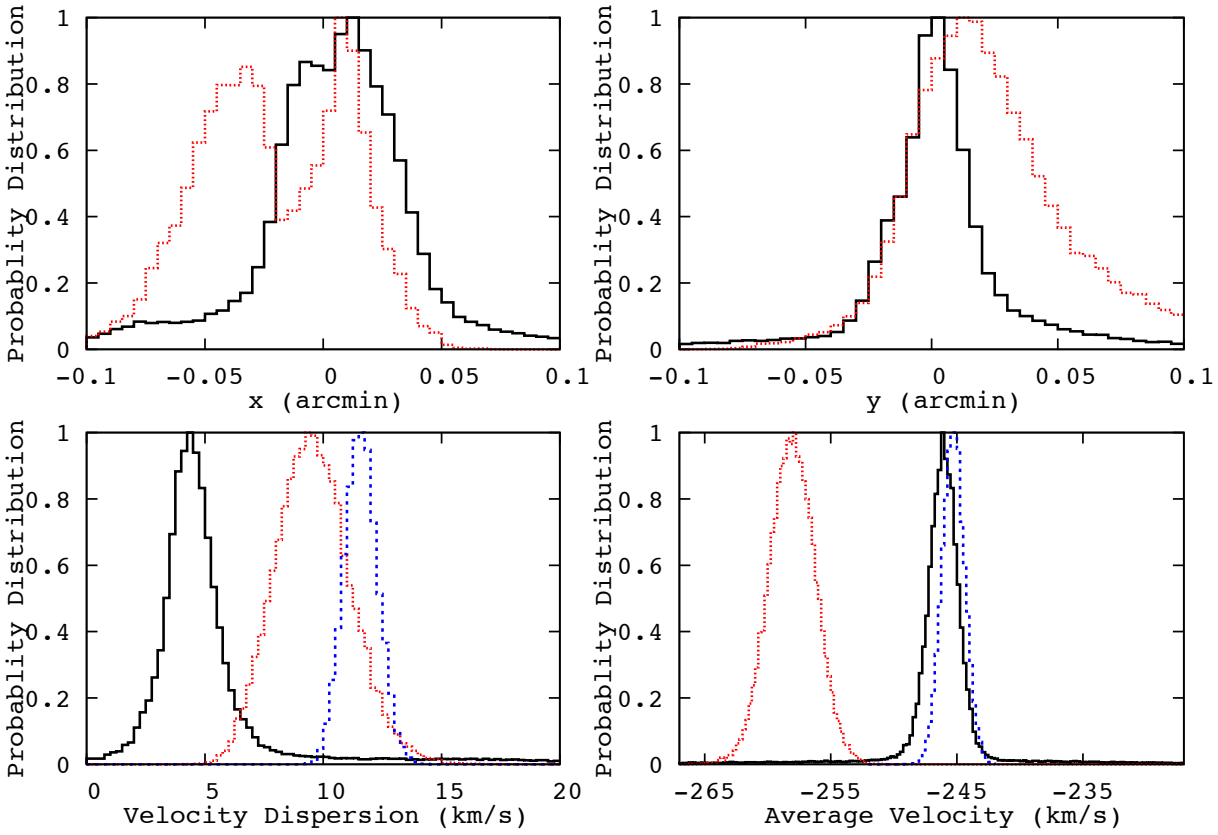

Figure 2.5: The posteriors for the secondary populations in Ursa Minor using the three-parameter model. The secondary populations are fixed at $(0.25, -0.07)$kpc and $(+0.24, 0.23)$kpc and allowed to vary 0.1kpc in both coordinates. They correspond to the cold (black solid) and the velocity offset (red dots) objects, respectively. *Upper Left:* The x coordinate posteriors for of the secondary populations. *Upper Right:* The y coordinate posteriors for the secondary populations. *Lower Left:* The velocity dispersion posteriors of the cold object (black solid), velocity offset object (red dotted), and the primary (blue dashed). *Lower Right:* The average velocity posteriors of the cold object (black solid), velocity offset object (red dotted), and the primary (blue dashed). The secondary populations have distinct kinematic properties and are both localized.

population, for example, if they had small tidal radius or small secondary population fraction.

The results for model selection of the D_{KL}, DIC, $\ln B_{01}$, and total membership using two different kinematic priors are summarized in Figure 2.3 (secondary population located at (0.2, -0.1)) and Figure 2.4 (secondary population located at (-0.23, 0.24)). In both figures, the two columns show different kinematic priors with the left column showing the cuts to find kinematically cold objects ($0 \leq \sigma \leq 10\,\mathrm{km\,s^{-1}}$, $-252 \leq \bar{v} \leq -242\,\mathrm{km\,s^{-1}}$) and the right column has the cuts to find objects with a significant velocity offset ($0 \leq \sigma \leq 20\,\mathrm{km\,s^{-1}}$, $-267 \leq \bar{v} \leq -237\,\mathrm{km\,s^{-1}}$); this cut will also find the kinematically cold objects, but in the Ursa Minor case the velocity offset object was significantly more likely and tended to dominate the posterior. The symbols for these columns are labeled/colored according to whether the x and y posterior was peaked (compared to the back ground) around the location of the secondary population: peaked/"found" (red square), not peaked/"not found" (green x), "possible" peaks (blue triangle), double peaked with one correct (light blue diamond). Results for the actual Ursa Minor data with corresponding cuts are shown as filled black circle. The "possible" peaks are posteriors where there was a peak near the second population's center, a small/medium peak somewhere else in the posterior, or a small peak at the correct location. The double peaked data had one peak at the correct location and a second at another location. The "possible" sets tended to span the border between "found" and "not found" and were not easily categorized otherwise. This definition of "found"/"not found" corresponds to higher likelihood values at the locations of secondary populations (similar to the K03 method).

Both Figures show a clear trend between the "found" and "not found" sets in all the model selection methods. Note that more negative DIC corresponds to favoring the more complicated model. Sets that are "not found" by the object detection have model selection criteria that is equivalent to the model selection criteria of null hypothesis mock data sets (i.e., sets made with no second population), cf., Section 2.4.1. Most importantly, the model selection criteria for the two objects found in Ursa Minor data also lie in the "found" section of the mock data's selection criteria. From the analysis of these mock data sets we conclude that our method is fully capable of detecting the

cold and velocity offset, and the model selection criteria favor the favor presence of two additional components in Ursa Minor.

2.4 Results

We have found two objects in the Ursa Minor data set of Muñoz et al. (2005a) using a Bayesian object detection method. The first object, referred to as the "cold object" here, is kinematically cold, $\sigma_{cold} = 3.5^{+1.8}_{-2.3}\,\mathrm{km\,s^{-1}}$, with an average velocity close to that of the full Ursa Minor sample, $\overline{\mathrm{v}}_{cold} = -246.8^{+1.8}_{-2.0}\,\mathrm{km\,s^{-1}}$. The location coincides with the location of the K03 stellar clump. The second object, referred to as the velocity offset object, has a large average velocity offset compared to the mean velocity of Ursa Minor, $\overline{\mathrm{v}}_{vo} = -258.8^{+2.0}_{-1.8}\,\mathrm{km\,s^{-1}}$ with a dispersion of $\sigma_{vo} = 8.8^{+1.5}_{-2.3}\,\mathrm{km\,s^{-1}}$. The kinematics and structural properties are summarized in the first section of Table 2.2. The model selection tests for the cold object are: Total Membership $= 15.8$, $D_{KL} = 4.8$, $DIC = -26.1$, $\ln B_{01} = 0.9$. The model selection tests for the velocity offsets object are: Total Membership $= 27.0$, $D_{KL} = 13.9$, $DIC = -36.5$, $\ln B_{01} = 3.6$. In Figures 2.3- 2.4 the results of model selection test are plotted along side the mock set distributions (filled black dot) All of the model selections tests favor the additional secondary objects with moderate to high significance except for the Bayes factor which has weak to moderate significance for the cold and velocity offset objects [4]. This significance is based on the recommendations of Trotta (2008); Ghosh et al. (2006); Spiegelhalter et al. (2002). However, it is important to judge the significance of the information criteria and the Bayes factor for the problem at hand. We do this by generating null data sets and deriving the information criteria and Bayes factor in the same way as the real data is handled. When this test is performed, we find that the confidence levels of both objects are above the 98% C. L. (see Table 2.2). In addition, all of the model selection values, for both locations/objects, lie in the "found" region of the mock sets of Figure 2.3 -2.4 .

[4] Assuming a uniform prior on the tidal radius of the objects instead of a prior in $\log_{10}$ increases the B_{01} to 1.4 and 5.7 for the cold and velocity offset spots respectively.

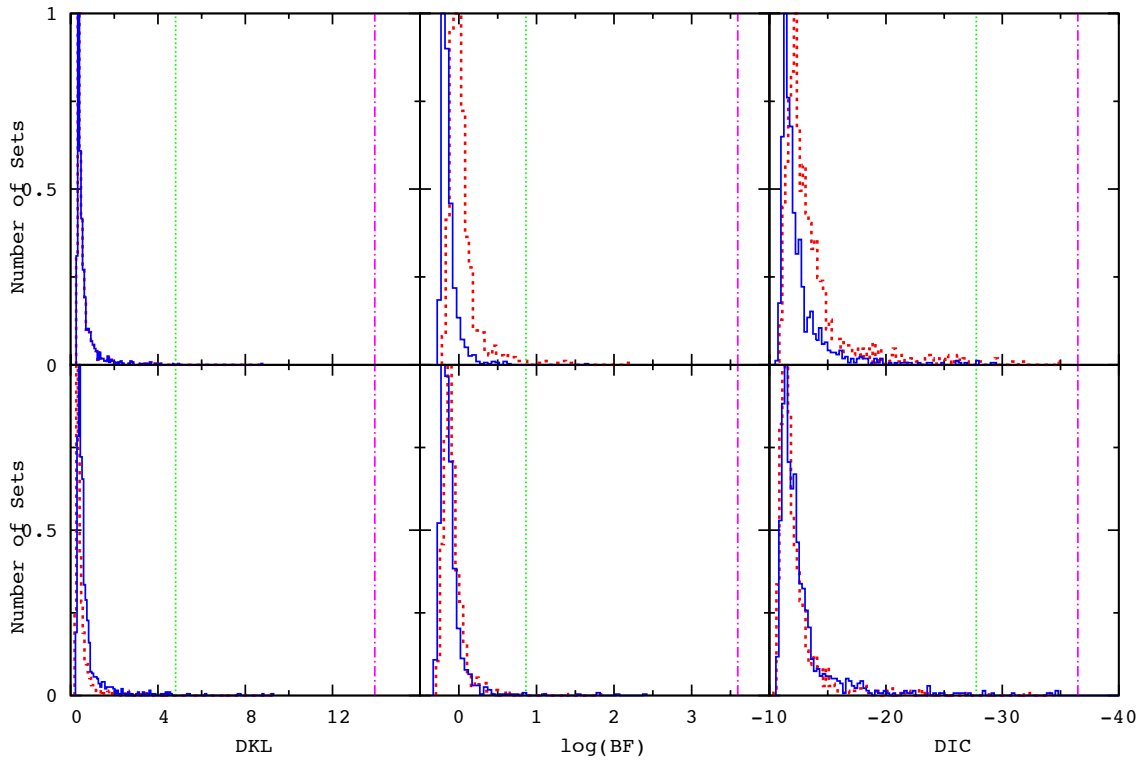

Figure 2.6: Histograms of D_{KL}, DIC and Bayes factor from analyses of 1000 null hypothesis mock data (top rows) and 1000 scrambled data sets (bottom rows) with Cut 1 (red dotted) and Cut 2 (blue solid). The vertical lines show the D_{KL}, DIC and Bayes factor values for the actual Ursa Minor data set with Cut 1 (green dotted) and Cut 2 (magenta dot-dashed). The inferred confidence levels for the Ursa Minor data is $\geq 98.5\%$ for all tests.

2.4.1 Significance of Information Criteria and Bayes' Factor

In order to assess the significance of the model selection tests, knowledge of the false positive rate is helpful. We make use of two types of tests for false positives: null hypothesis mock data sets and scrambled data sets. Null hypothesis mock data sets are constructed by redrawing the line-of-sight velocities from a Gaussian with Ursa Minor kinematics[5]. To simulate positional and velocity errors, the positions of stars and the line-of-sight velocity errors were kept. The scrambled sets were constructed by repicking a random observed line-of-sight velocity and line-of-sight velocity

[5]We used $\bar{v} = -247.0\,\mathrm{km\,s^{-1}}$ and $\sigma = 11.5\,\mathrm{km\,s^{-1}}$.

error pair, without replacement, for each star in the data set. 1000 null hypothesis mock data sets and scrambled data sets were constructed and analyzed with our object detection method.

The results of the object detection method and our employed model selection tests for the null hypothesis mock data sets and the scrambled mock data sets are shown in the Figures 2.6. The top and bottom rows refer to the null hypothesis and scrambled tests respectively. The D_{KL} (right column), DIC (middle column), and $\ln B_{01}$ (left column) are binned and the maximum is normalized to unity. The analysis with the cuts to find cold objects ($0 \leq \sigma \leq 10\,\mathrm{km\,s^{-1}}$, $-252 \leq \bar{v} \leq -242\,\mathrm{km\,s^{-1}}$) is shown in red, while that with cuts to find objects with significant velocity offset ($0 \leq \sigma \leq 20\,\mathrm{km\,s^{-1}}$, $-267 \leq \bar{v} \leq -237\,\mathrm{km\,s^{-1}}$) is shown in blue. The model selection results for the real Ursa Minor data are plotted as vertical lines: cold object with green dotted line and velocity offset object with purple dash-dot line. The confidence levels of the model selection criteria for the null hypothesis mock data sets and scrambled data sets are above the 98.5% c. l. with every model selection criteria. They are summarized in Table 2.3. Even though the $\ln B_{01}$ shows weak evidence for the cold object according to standard definitions, it is still above the 95% confidence level for both the null hypothesis mock data sets and scrambled data sets.

2.4.2 Narrowing down secondary population parameters using a 3-component model

In the detection phase, the kinematic properties of one object is determined while the other is part of the background. To reliably calculate the kinematic properties of each secondary object we introduce a model with two secondary populations fixed within 0.1 kpc from the best-fit center locations. Equation 3.15 is modified to include a third component. Two normalization parameters are required, $\alpha_2 = \frac{N_2}{N_1}$, and $\alpha_p = \frac{N_p}{N_1}$ where N_1 and N_2 denote the normalization of the first and second object. The results for the kinematic parameters are: $\sigma_{cold} = 4.3 \pm 0.8\,\mathrm{km\,s^{-1}}$, $\bar{v}_{cold} = -246.3 \pm 1.0\,\mathrm{km\,s^{-1}}$, $\sigma_{vo} = 9.3 \pm 1.3\,\mathrm{km\,s^{-1}}$, and $\bar{v}_{vo} = -258.0 \pm 1.5\,\mathrm{km\,s^{-1}}$, respectively. These values are in full agreement with the values obtained using the two-component (Bayesian object detection) method.

The normalization ratios, as defined, are not easily interpreted. So we introduce a derived parameter, local fraction or f_{local}, that is defined as the weighted average of stars with memberships greater than 50% in the secondary population compared to the total number of stars within the secondary object's tidal radius. In short, it is a measure of the fraction of secondary stars in each object's location. We derive $f_{local,cold} = 15.8/22.5$ or 70% and $f_{local,vo} = 27.0/31.6$ or 85%. Clearly, we are able to find these objects only because they seem to have a high local fraction. The kinematics and structural properties of the secondary population model are summarized in the second section of Table 2.2. In upper left and right panels of Figure 2.5, we have plotted the posteriors for the x and y centers, respectively, for the cold (black solid) and velocity offset objects (red dotted). The centers for the cold and velocity offset object are $(0.25, -0.07)$ kpc and $(+0.24, 0.23)$ kpc and the two panels show the deviation from the "fixed" centers. The lower right (lower left) panel of Figure 2.5 is the posterior of the σ_s ($\bar{v}_s$) for the cold (black solid), velocity offset objects (red dotted), and primary (blue dashed). The Bayes factor of this model is 10.0. The 3 component model is highly favored compared to the null model.

Table 2.3: Confidence Levels computed from null hypothesis and scrambled mock data sets. The inferred C.L.. refers to the number of null hypothesis mock data sets and scrambled data sets sets that have a model selection value lower than that of the actual Ursa Minor data. The 95% C.L. value is defined such that 95% of the null hypothesis or scrambled data sets have a value below this. Both additional populations found in the Ursa Minor data are above the 98% C.L. for all the model selection methods. The two cuts indicated in the table as "Cuts 1 and 2" are defined as follows. Cut 1 is $0 \leq \sigma \leq 10\,\mathrm{km\,s^{-1}}$ and $-252 \leq \bar{v} \leq -242\,\mathrm{km\,s^{-1}}$ used to find the cold spot object in the data. Cut 2 is $0 \leq \sigma \leq 20\,\mathrm{km\,s^{-1}}$ and $-267 \leq \bar{v} \leq -237\,\mathrm{km\,s^{-1}}$ used to find the velocity offset object in the data.

Test using null hypothesis mock data sets

	Total Average Membership	Information Entropy D_{KL}	Information Entropy DIC	Bayesian Evidence $\ln B_{01}$
Value at 95% C.L. from null hypothesis mock data sets using Cut 1	5.25	1.28	-16.35	0.17
Cold object values from data (inferred C. L.)	15.82 (99.8%)	4.82 (99.7%)	-26.08 (99.5%)	0.87 (99.7%)
Value at 95% C.L. from null hypothesis mock data sets using Cut 2	4.49	1.84	-17.79	0.13
Velocity offset object values from data (inferred C.L.)	27.02 (> 99.9 %)	13.93 (> 99.9 %)	-36.49 (99.9 %)	3.59 (> 99.9 %)

Test using scrambled data sets

	Total Average Membership	Information Entropy D_{KL}	Information Entropy DIC	Bayesian Evidence $\ln B_{01}$
Value at 95% C.L. from scrambled mock data sets using Cut 1	6.99	2.22	-20.45	0.40
Cold object values from data (inferred C. L.)	15.82 (99.7%)	4.82 (99.1%)	-26.08 (98.5%)	0.87 (99.0%)
Value at 95% C.L. from scrambled mock data sets using Cut 2	3.89	1.46	-16.30	0.07
Velocity offset object values from data (inferred C.L.)	27.02 (> 99.9 %)	13.93 (> 99.9 %)	-36.49 (> 99.9 %)	3.59 (> 99.9 %)

An increased prior volume for the centers and tidal radius in the 3-component model changes the posteriors for the structural parameters of the velocity offset object but does not change it's kinematics. By only allowing more freedom in the location of the centers (200 pc versus 100 pc) the posteriors of both centers gain tails. An increase in the maximum tidal radius (in the prior) of the objects (500 pc from 300 pc) increases the size of the velocity offset object and moves its center roughly 150 pc away from the center of Ursa Minor while the same change introduces tails in the posterior of the cold object. This change is from several stars in the outer region of Ursa Minor that have consistent kinematics with the velocity offset object. Given these results, it is fair to say that the the size and center of the secondary objects are not known with high precision and more data will help considerably. However, our conclusions regarding kinematics seem to be robust.

2.4.3 Perspective Motion

Line-of-sight velocity measurements for the Milky Way satellites receive a small contribution from x and y direction velocities of the star (where z is along the line-of-sight to the center of the galaxy), and this contribution increases with distance from the center (Feast et al. 1961; Kaplinghat & Strigari 2008). A similar contribution could also arise due to solid-body rotation or some other physical mechanism (such as tides) that leads to a velocity gradient. Motivated by the large velocity-offset we found, we ask whether the inclusion of this effect changes our conclusions. The observed line-of-sight velocity of a star may be written as,

$$v_{\rm los} = v_z - v_x x/D - v_y y/D \tag{2.13}$$

where D is the distance to the galaxy and (x,y) are the projected coordinates on the sky. This method has been applied to the dSph's Carina, Fornax, Sculptor, and Sextans with results that agree HST and ground based proper motion measurements (Walker et al. 2008). Observations from the HST find a proper motion for Ursa Minor of $(\mu_\alpha, \mu_\delta) = (-50 \pm 17, 22 \pm 16)\,{\rm mas\,century}^{-1}$ (Pi-

atek et al. 2005). The proper motion we find assuming only a single kinematics population is $(\mu_\alpha, \mu_\delta) = (529 \pm 848, -280 \pm 449)\,\mathrm{mas\,century}^{-1}$, which is an order of magnitude larger (when comparing the mean) than the HST measurement and has enormous error bars. To see how much of an effect that the secondary objects have on this calculation we repeat the measurement and remove stars from the sample in three ways: remove stars with high membership in the velocity offset object, high membership in both objects, or remove all stars in the object's location. The proper motions are measured to be: $(\mu_\alpha, \mu_\delta) = (117 \pm 90, 163 \pm 127)\,\mathrm{mas\,century}^{-1}$, $(\mu_\alpha, \mu_\delta) = (-84 \pm 79, -185 \pm 174)\,\mathrm{mas\,century}^{-1}$, and $(\mu_\alpha, \mu_\delta) = (-67 \pm 60, -203 \pm 181)\,\mathrm{mas\,century}^{-1}$ respectively. These comparisons provide clear proof that it is hard to estimate the tangential velocity with perspective motion if there are secondary populations in the data set.

To investigate this issue further we run a three-component model to detect the two secondary objects when including perspective motion. We add this effect into our likelihood function by changing the model velocity for all three components (cf., $\bar{v}_{p,s}$ in Equation 2.4) to $v_{\mathrm{los},i}$ given by Equation 2.13 with x_i and y_i for each star measured from the center of Ursa Minor. Each component has its own v_z but v_x and v_y are the same for all three components. Note that the actual tangential velocity of the two secondary components is now implicitly tied to the v_z value – there is no hope of disentangling them given the small projection on the sky of the secondary components. We then impose the same constraints on the center as before (cf., §2.4.2). We find results that are consistent with those we found in §2.4.2 in the absence of perspective motion: $x_{cold} = 0.245^{+0.03}_{-0.04}$kpc, $y_{cold} = -0.065^{+0.015}_{-0.025}$kpc and $x_{vo} = -0.275^{+0.04}_{-0.035}$kpc, $y_{vo} = 0.24 \pm 0.025$kpc. The kinematic properties are the same as without perspective motion except with larger error bars. Thus the three-component model with the prior on the centers provides a different fit and favors the presence of the secondary objects over perspective motion. Had perspective motion or a velocity gradient or rotation been a better fit to the likelihood instead of either of the objects, this would not have been the case since the likelihood allows for the freedom to dial down the fraction of stars in the secondary objects. In this three-component fit, the mean velocity of Ursa Minor is $(-311 \pm 212, -548^{+357}_{-324}, -245.5 \pm 0.75)\ \mathrm{km\,s}^{-1}$, in good agreement with the results obtained when stars in the locations populated

by the secondary populations are removed.

We also explored the effect of using the Bayesian object detection method with perspective motion. This could lead to faulty results (and we show below that it does) because the velocity offset spot has a large impact on the determination of the background parameters – specifically the perspective motion. With the velocity cuts to find the cold object, we find a mean velocity for Ursa Minor of $(-100^{+100}_{-100}, -1125^{+275}_{-250}, -247.5^{+0.5}_{-0.5})\,\mathrm{km\,s^{-1}}$ and a dispersion in the line-of-sight velocity of $11.0 \pm 0.5\,\mathrm{km\,s^{-1}}$. The dispersion of the cold object is now consistent with zero at about 1-σ, 3.25 ± 3.0 $\mathrm{km\,s^{-1}}$ and the location of the centers is now much less well-determined. However, the values obtained for the perspective motion are unphysically large and hence this is clearly not the correct model to be considering. With the $\pm 20\,\mathrm{km\,s^{-1}}$ velocity cut (to find the velocity offset object), we find a mean velocity for Ursa Minor of $(-200^{+150}_{-150}, -1175^{+400}_{-400}, -247^{+1.0}_{-1.25})\,\mathrm{km\,s^{-1}}$ and 10.75 ± 0.5 $\mathrm{km\,s^{-1}}$ for its dispersion in the line-of-sight velocity. The center, as with the other object, is no longer tightly constrained, and the hint for deviation in mean velocity for this object is muted ($-258^{+7.5}_{-4.5}$ $\mathrm{km\,s^{-1}}$). Thus, we arrive at the conclusion (unsurprisingly) that *varying background parameters* in Bayesian object detection methods can lead to faulty results in data sets containing multiple signals if those signals have a significant effect on the determination of the background parameters. In particular, for this analysis we saw that the presence of the velocity offset spot affects the magnitude and the direction of the inferred tangential motion and hence the object detection method has trouble fitting one secondary location and perspective motion. But with two localized secondary populations and perspective motion the method still picks out both secondary objects. Thus, the three component model is preferred by this data set.

A tangential velocity measured using perspective motion could also be hiding a possible solid-body rotation. An order of magnitude estimate of this rotation speed would be $v_{rot} = \frac{R_e}{D}\sqrt{v_x^2 + v_y^2}$ ($R_e = 445 \pm 44\,\mathrm{pc}, D = 77 \pm 4\,\mathrm{kpc}$). Using the results presented in this section, we calculate: $v_{rot} \sim 7\,\mathrm{km\,s^{-1}}$ with entire data set, and $v_{rot} \sim 4\,\mathrm{km\,s^{-1}}$ when the velocity offset population is removed, and when both secondary populations are removed or when all stars near the secondary

populations are removed. The rotation speeds are all comparable but in each estimate the rotation is about a different axis. The summary of our results from this section is that a larger data set is required to simultaneously constrain properties of the secondary populations and rotation or proper motion. The results of our three-component analysis suggest that the data prefer the presence of both secondary objects to perspective motion (or a rotation that masquerades as it).

2.5 Discussion

We discuss how our results compare to previous work and possible explanations for our results. K03 utilized a likelihood test comparing two (Ursa Minor dSph plus a secondary population) and one component kinematic models to estimate the locations of secondary populations and to find the best fit parameters of the secondary populations. They discovered a stellar clump (a likelihood ratio of $\sim 10^4$) located at (10′,4′) (on-sky frame relative to the Ursa Minor center) with kinematic parameters, $\sigma = 0.5$ km s^{-1}, $v_s = -1$ km s^{-1} and clump fraction of 0.7 (fraction of stars in the second population). The kinematically cold object found with our object detection method is centered at $(10.8' \pm 1.8, 5.5' \pm 0.9)$ (on-sky frame relative to Ursa Minor center), has a size of $6.7' \pm 0.5$, with kinematic properties $\sigma = 4.25 \pm 0.75$ km s^{-1}, and $\Delta\bar{v} = -1.1^{+1.5}_{-1.25}$ km s^{-1}. The difference between our results and those of K03 lie in the velocity dispersion of the cold object. We have considerably more stars (in total 212 to 134 of K03) and are therefore able to infer the dispersion with much greater confidence. We find the mean value for the velocity dispersion to be close to 4 km s^{-1}, similar to the dispersion of Segue 1 dSph (Simon et al. 2011). In addition, our methodology allows us to compute error bars on model parameters.

The main uncertainty in our estimates of the dispersion for cold and velocity offset objects is the presence of perspective motion or solid-body rotation. Perspective motion by itself cannot explain these secondary populations. A three-component analysis (i.e., main Ursa Minor population and both secondary populations) with the coordinates of the centers fixed to within 100 pc and in-

cluding perspective motion (with unconstrained tangential velocity) prefers the presence of both the secondary populations. In this analysis, the velocity dispersions of the cold or velocity offset objects are not significantly different from the values obtained without including perspective motion.

To estimate the luminosity of the secondary objects, we use the total membership of the objects with the assumption that the stars were drawn uniformly from the three distributions of Ursa Minor. We find the luminosity of the cold and velocity offset objects to be $4 \times 10^4\, L_\odot$ and $6 \times 10^4\, L_\odot$. The luminosity of the K03 object is $1.5 \times 10^4\, L_\odot$, and given the uncertainties we would chalk this down as agreement between the two analyses. The dynamical mass within half-light radius of dispersion supported systems can be estimated to about 20% accuracy using the line-of-sight velocity dispersions and the half-light radius (Walker et al. 2009b; Wolf et al. 2010). Assuming that the ratio of $r_{1/2}/r_{tidal}$ of the objects is the same as that of Ursa Minor, we find $M_{1/2} = 6 \times 10^5\, M_\odot$, and $M_{1/2} = 5 \times 10^6\, M_\odot$ for the cold and velocity offset object. From this $M/L(r_{1/2}) \approx 30\, M_\odot/L_\odot$ and $M/L(r_{1/2}) \approx 175\, M_\odot/L_\odot$ for the cold and velocity offset objects. If we use this same estimator to find the velocity dispersions assuming the objects are relaxed systems with only stellar components and $M/L = 2$ (as in K03), we estimate a velocity dispersion of $\sigma = 1.0$ km s^{-1} for both the cold and velocity offset objects. This differs from the velocity dispersion found through our object detection method by 4 σ and 6.6 σ for the cold and velocity offset objects, respectively. Note that the estimator for $M_{1/2}$ assumes that the system is dynamical equilibrium, which may not be the case here. If our current results hold up with the addition of more data, then either these objects have highly inflated velocity dispersions due to the influence of motion in binary stellar systems or tidal disruption, or these objects really do have a much larger mass than inferred from their luminosities. In the latter case, we would have found a satellite of Ursa Minor, the first detection of a satellite of a satellite galaxy. We discuss each of these possibilities briefly below.

Contribution of binary orbital motion to the line-of-sight velocities can inflate the observed line-of-sight velocities of stars (Aaronson & Olszewski 1987; Hargreaves et al. 1996; Olszewski et al.

1996; Minor et al. 2010; McConnachie & Côté 2010). A galaxy with a lower intrinsic velocity dispersion has a higher chance of having its observed dispersion inflated. A dSph with a velocity dispersion between 4 and 10 $\mathrm{km\,s^{-1}}$ is highly unlikely to be inflated by more than 30% (Minor et al. 2010) (for an application of this method see Simon et al. (2011); Martinez et al. (2011)). The objects we have found have observed velocity dispersions in this range. Assuming both objects are inflated by 30%, their actual intrinsic velocity dispersion would be between $2.5-3.3$ $\mathrm{km\,s^{-1}}$ and 7.1 $\mathrm{km\,s^{-1}}$ respectively, for the cold and velocity offset objects. These velocity dispersions are still much higher than 1 $\mathrm{km\,s^{-1}}$ (that is expected for a relaxed stellar system, i.e. a globular cluster). It is unlikely that binary orbital motion alone can account for the large velocity dispersions inferred from this data set for both secondary populations. With multi-epoch data, we will be able test this hypothesis directly as was done for Segue 1 dSph (Martinez et al. 2011).

To assess the effect of tidal disruption from Ursa Minor we calculate the Jacobi Radius, r_J, and compare r_J to the mean tidal radius estimated from our three-component analysis. To calculate the Jacobi radius, we consider both an NFW (Navarro et al. 1997) and a pseudo-isothermal (cored) profile for the halo of Ursa Minor. To set the NFW density profile of Ursa Minor, we pick NFW scale radius $r_s = 1$ kpc and estimate the density normalization ρ_s using $M_{1/2}$ values from Wolf et al. (2010) for a NFW profile. We find that if the actual distance of the center of the objects is equal to the projected distance from the center of Ursa Minor, then $r_J < r_t$. If the objects are further than about 1 kpc away, then $r_J > r_t$ with the NFW profile. The situation for a pseudo-isothermal profile $(1/(r^2+r_0^2))$ with $r_0 = 300$ pc is similar, with $r_J > r_t$ if the objects are further than about 1-2 kpc from the center of Ursa Minor. The r_J estimates indicate that tides from Ursa Minor could have an effect on these objects even if they are protected by their own dark matter halos. The survival of globular cluster sized objects in dSphs has far-reaching implications for the density profile of the host halo (Kleyna et al. 2003; Goerdt et al. 2006; Strigari et al. 2006; Cowsik et al. 2009; Lora et al. 2012). The objects we find are more extended and massive than the globular cluster sized objects considered in such work in the past. Thus these constraints will have to re-evaluated.

Generically, the estimated high dispersions of these objects and their survival are facts at odds with each other. The age of Ursa Minor ($\sim$ 12 Gyr) is much longer than the crossing time for stars inside Ursa Minor of $\sim$ 150 Myr (assuming a typical velocity of $10\,\mathrm{km\,s^{-1}}$). The crossing times for the stars in the cold and velocity offset object are $\sim$ 50 Myr. These objects have had time to make multiple orbits around Ursa Minor and it is hard to see how they could have survived given the short crossing times unless they have been recently captured by Ursa Minor and are now the process of tidal disrupted (which would account for the inflated velocity dispersion). However, this is not a likely scenario since Ursa Minor probably fell into the Milky Way early, between 8-11 Gyr (Rocha et al. 2011), and capturing a large object after that is unlikely. It is more reasonable to assume that these objects have survived for long because they were protected by a dark matter halo of their own. The reality is probably more complicated: these objects may have their own dark matter halos and at the same time are being tidally disrupted. These implications are intimately tied to the dark matter halo of Ursa Minor and pinning down the properties of these objects would help to decipher if the dark matter halo of Ursa Minor has a cusp or a core.

2.6 Conclusion

We have presented a method for finding multiple localized kinematically-distinct populations (stellar substructure) in line-of-sight velocity data. In the the nearby dwarf spheroidal galaxy Ursa Minor, we have found two secondary populations: "cold" and "velocity offset (vo)" objects. The estimated velocity dispersions are $\sigma_{cold} = 4.25 \pm 0.75$ km s^{-1} and $\sigma_{vo} = 9.25 \pm 1.25$ km s^{-1}, and the estimated mean velocities are $\bar{v}_{cold} = -246.25 \pm 1.0$ km s^{-1} and $\bar{v}_{vo} = -258.0 \pm 1.5$ km s^{-1}. They are located at $(0.25^{+0.04}_{-0.06}, -0.07^{+0.03}_{-0.07})$ kpc (cold object) and $(-0.24 \pm 0.09, 0.23 \pm 0.02)$ kpc (velocity offset object) with respect to the center of Ursa Minor. The location of the cold object matches that found earlier by Kleyna et al. (2003), but our results reveal that the velocity dispersion of this cold object could be large with a mean value close to 4 km s^{-1}. To assess the significance

of our detection's, we employed the Bayes Factor and information criteria D_{KL} and DIC supplemented with the analysis of mock data sets with secondary populations, null hypothesis mock data sets and scrambled data sets. The two secondary objects have $> 98.5\%$ C.L. in all the model selection tests employed.

If the velocity dispersions are as large as our Bayesian analysis seems to indicate, then these objects are likely undergoing tidal disruption or are embedded in a dark matter halo. The two possibilities are not exclusive of each other. If these objects are dark matter dominated, this would be the first detection of a satellite of a satellite galaxy.

As emphasized by Kleyna et al. (2003) the presence of localized substructure has important implications for inner density profile of the dark matter halo of Ursa Minor. The shape of the inner profile (cusp or core) has important implications for the properties of the dark matter particle with cold dark matter model predicting a cuspy inner density profile. If the stellar substructure is hosted by its own dark matter halo, then it has further implications for dark matter models since this would likely be the smallest bound dark matter structure discovered.

Acknowledgments

This research was supported in part by the National Science Foundation Grant 0855462 at UC Irvine. This research was supported in part by the Perimeter Institute of Theoretical Physics during a visit by M.K. Research at Perimeter Institute is supported by the Government of Canada through Industry Canada and by the Province of Ontario through the Ministry of Economic Development and Innovation. G.D.M. acknowledges support from the Wenner-Gren Foundations. R.R.M. acknowledges support from the GEMINI-CONICYT Fund, allocated to the project N°32080010, from CONICYT through project BASAL PFB-06 and the Fondo Nacional de Investigación Científica y Tecnológica (Fondecyt project N°1120013).

Chapter 3

Multiple Chemo-Dynamical Stellar Populations in the Ursa Minor Dwarf Spheroidal Galaxy

3.1 Summary

We present a Bayesian method to identify multiple stellar populations in dwarf spheroidal galaxies (dSph) utilizing line-of-sight velocity, metallicity, and positional stellar data without the assumption of spherical symmetry, building on the work of Walker & Peñarrubia (2011a). The method includes a novel method for Milky Way background removal. We apply this method to a new Keck/DEIMOS spectroscopic survey of Ursa Minor dSph. This survey contains over 800 dSph members, making this the largest spectroscopic sample containing both line-of-sight velocity and [Fe/H] measurements in Ursa Minor. Our Bayesian method detects two distinct chemo-dynamical stellar populations with high significance (in Bayes' factor, $\ln B = 41$). The kinematically colder population (radial velocity dispersion of $5.3^{+0.5}_{-0.5}\,\mathrm{km\,s^{-1}}$) is comparatively more metal rich and more

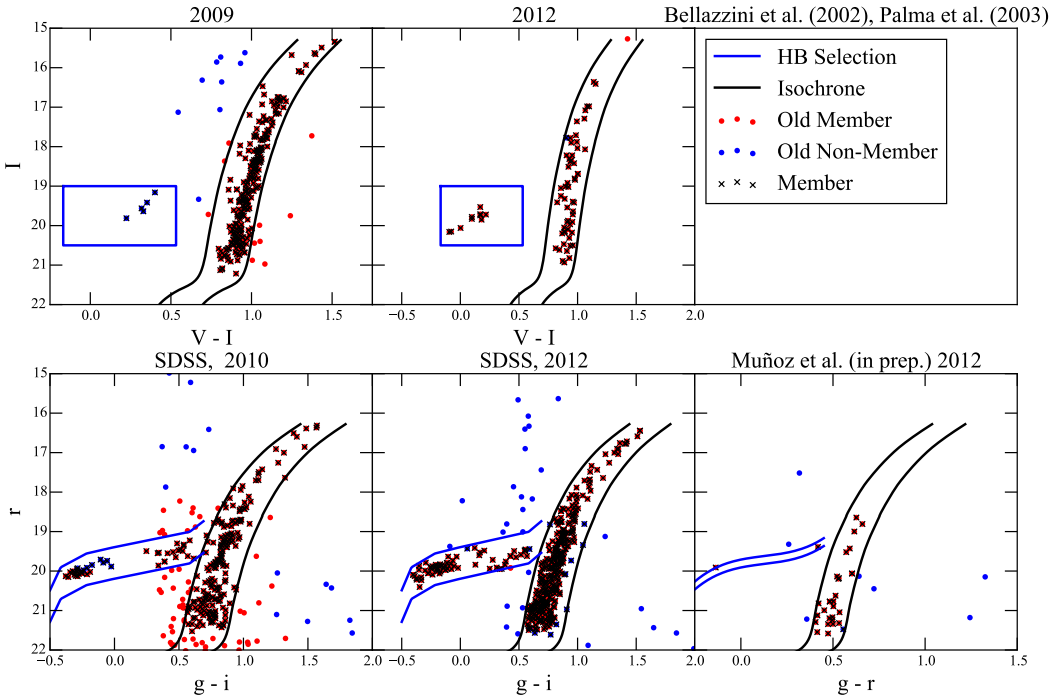

Figure 3.1: Color magnitude diagrams for all stars with spectroscopic measurements. Red and blue points correspond to target selection for potential Ursa Minor and Milky Way members respectively. Stars with black x's that pass the color-magnitude selection with consistent theoretical isochrones. Black lines are Dotter et al. (2008) 10 Gyr, [Fe/H]=-2 isochrones in different color-magnitude bands. Blue boxes and lines represent the horizontal branch selections. The 5 panels correspond to the photometric set utilized to select the star and the year in the title corresponds to the observing epoch. 903 stars pass the color-magnitude selection, of which there are 111 stars with 2 measurements and 9 stars with 3 measurements (see Section 3.2.6).

centrally concentrated than the hotter population ($13.9^{+1.0}_{-0.9}\,\mathrm{km\,s^{-1}}$). The hotter population is more spherically distributed than the colder population. We discuss systematics and peculiarities in both populations that prohibit a clean measurement of the mass slope. We provide a summary of the mass measurements of the separate chemo-dynamical populations for all the bright Milky Way dSphs and reaffirm the "too big to fail" problem.

Table 3.1: Observation Log

Slitmask	No. of Targets	Date	Airmass	Seeing	Exposures
Umi1[a]	125	2009 Feb 22	1.99	0.71″	3 × 1200 s
Umi2[a]	134	2009 Feb 22	1.79	1.00″	2 × 1200 s, 1400 s
Umi3[a]	137	2009 Feb 23	1.48	0.98″	3 × 1200 s
Umi6[a]	137	2009 Feb 23	1.57	0.93″	3 × 1200 s
Umima1	85	2010 May 11	1.50	0.78″	3×1200s
Umima2	27	2010 May 11	1.48	0.55″	3×1200s
Umima3	18	2010 May 11	1.52	0.67″	3×1200s
Umimi1	36	2010 May 12	1.50	0.64″	3×1200
Umimi2	12	2010 May 12	1.46	0.71″	3×1200
Umimi3	10	2010 May 12	1.50	0.84″	3×1200
Umix1	20	2010 May 11	1.64	0.82″	3×1200
Umix2	25	2010 May 11	1.81	0.87″	1×1200
		2010 May 12	1.81	0.91″	1×1500
Umix4	78	2010 May 12	1.64	0.82″	3×1200
uss-1	68	2012 April 19	1.58	1.1″	3×1020 s
	68	2012 April 23	1.60	0.8″	1×1020 s
uss-2	57	2012 April 19	1.74	1.0″	2×1020 s, 600 s
uss-3	74	2012 April 21	1.55	0.5″	3×960 s
uss-4	66	2012 April 21	1.70	0.7″	3×960 s, 480 s
uss-5	27	2012 April 21	1.49	0.5″	2×960 s
uss-6	13	2012 April 22	1.49	0.7″	2×960 s, 900 s
uss-7	17	2012 April 23	1.49	0.9″	2×1020 s
uss-8	57	2012 April 22	1.56	0.9″	2×1080 s, 1170 s
uss-9	24	2012 April 23	1.55	0.7″	1×1080 s, 1020 s
uss-10	65	2012 April 22	1.47	0.8″	3×1020 s
uss-11	56	2012 April 21	1.48	0.5″	3×960 s
uss-12	54	2012 April 23	1.47	0.9″	3×1020 s

a Observations by (Kirby et al. 2010).

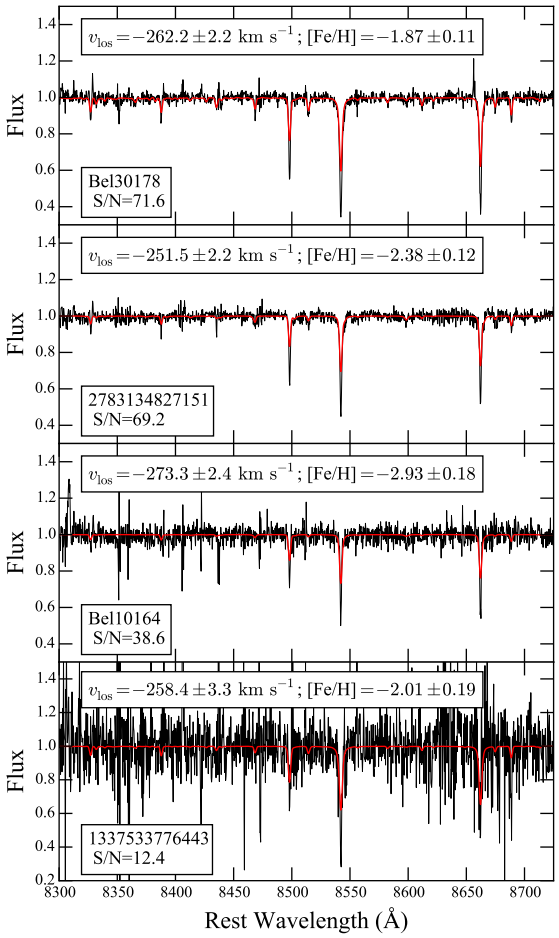

Figure 3.2: Examples of Keck/DEIMOS spectra focused in the wavelength region containing the calcium triplet. Overlaid are synthetic spectra in red. Denoted is the star id, S/N, velocity, and metallicity. The stars are arranged in order of decreasing S/N.

3.2 Data

3.2.1 Observations and Target Selection

Spectroscopic observations were carried out February 22–23 2009 (first presented by Kirby et al. 2010), May 11–12 2010, and April 20–22 2012 on the Keck/DEIMOS spectrograph (Faber et al. 2003). We used the 1200G diffraction grating, which has a groove spacing of 1200 mm^{-1} and a blaze wavelength of 7760 . The grating was tilted such that the typical central wavelength of a spectrum was 7800 , and the typical wavelength range was about 2600 . In practice, the wavelength range for each spectrum varied by up to 300 depending on the location of the slit along the dispersion axis. The grating was used in first order, and higher orders were blocked with the OG550 filter. DEIMOS has a flexure compensation system that keeps the wavelength calibration stable to within ~ 0.05 over a full night.

Spectroscopic targets were selected from various photometric catalogs. Where the slitmask design constraints forced a choice among multiple candidates, we prioritized stars on the red giant branch (RGB). Kirby et al. (2010) described the slitmask design for the 2009 observations. Targets were selected from Bellazzini et al.'s (2002b) photometric catalog in the V and I filters. We used the color–magnitude diagram (CMD) in conjunction with Yonsei-Yale isochrones (Demarque et al. 2004) to inform the selection. Targets were selected between a blue bound and red bound. The blue bound was 0.1 mag bluer in de-reddened $(V-I)_0$ than a 2 Gyr isochrone with $[\mathrm{Fe/H}] = -3.76$ and $[\alpha/\mathrm{Fe}] = 0.0$. The red bound was a 14 Gyr isochrones with $[\mathrm{Fe/H}] = +0.05$ and $[\alpha/\mathrm{Fe}] = +0.3$. Horizontal branch (HB) stars were also selected from a box in the CMD: $20.5 > I_0 > 19.0$ and $-0.20 < (V-I)_0 < 0.65$. Brighter stars were given higher priority.

Slitmasks from the 2010 observations were designed from SDSS *ugriz* photometry (Abazajian et al. 2009). Stars were selected to lie within a color range around a 14.1 Gyr, $[\mathrm{Fe/H}] = -1.63$, Padova isochrone (Girardi et al. 2004). The allowed range was 0.4 mag bluer and 0.3 mag redder

in $(g-r)_0$ color. We also selected HB stars from a box in the CMD: $21 > r_0 > 20$ and $-0.4 < (g-r)_0 < 0.0$. As for the 2009 observations, brighter stars were given higher priorities for spectroscopic selection.

Because there is no published photometric data set for Ursa Minor that covers the full extent of the galaxy and is sufficiently deep for our purposes, the spectroscopic target selection for the 2012 observing run relied on a number of different sources.

UMi has been observed by the Sloan Digital Sky Survey (SDSS), but the SDSS DR7 (Abazajian et al. 2009) coverage nearly bisects the galaxy along its major axis, with the southeast half of the galaxy included but no data in the northwest half. SDSS DR8 (Aihara et al. 2011a), in contrast, contains several stripes crossing the galaxy from southeast to northwest, with $\sim 20'$ gaps between each stripe. The difference in coverage between DR7 and DR8 is a result of different data quality criteria in the SDSS processing of those data sets (N. Padmanabhan 2012, private communication), but there is no evidence for systematic photometric errors in either the DR7 or DR8 imaging in this region. We therefore generated a combined SDSS DR7 + DR8 catalog for Umi, using DR7 measurements where available and DR8 elsewhere.[1]

In addition to SDSS, we used the wide-field Washington/DDO51 photometry of Palma et al. (2003b) the deeper VI imaging of Bellazzini et al. (2002b) in the center of the galaxy, and deep, wide-field gr imaging covering 1 deg^2 with CFHT/Megacam by Muñoz et al. (in prep.). These catalogs were merged with the SDSS data taking precedence, followed by stars in the Palma, Bellazzini, and Muñoz, in that order. For the latter three data sets, we applied zero point offsets to the astrometry so that the median position differences with respect to SDSS DR9 of all stars in common were zero.

Spectroscopic targeting priorities for stars in the SDSS, Bellazzini, and Muñoz data sets were

[1]DR8 contained an astrometry error of up to $0.25''$ for northern targets (Aihara et al. 2011b; Ahn et al. 2012), so for stars in the DR8 photometric catalog we used the corrected positions provided in the early release of DR9 (Ahn et al. 2012).

determined using $[\mathrm{Fe/H}] = -2$, 10 Gyr isochrones from Dotter et al. (2008). The RGB selection window was defined so as to include all obvious members of UMi near the center of the galaxy, with more generous color limits to the blue side of the RGB to allow for unusually metal-poor stars. We constructed a similar selection window for horizontal branch (HB) stars by generating a large number of synthetic HB stars with the online code provided by Dotter et al. (2007) using the same age and metallicity as for the RGB and then fitting a polynomial to determine the luminosity of the HB as a function of color. We assigned RGB candidates higher priorities than HB candidates, with relative priorities determined by magnitude within each category (where preference is given to brighter stars), and then added priority bonuses for stars already confirmed to be UMi members by Palma et al. (2003b) or the 2009/2010 Kirby data sets described above. Stars located within the bounds of either of the two possible substructures in UMi identified by Pace et al. (2014) were given the highest priorities, and then slitmasks were placed to ensure full coverage of both substructures.

3.2.2 Reductions

We reduced the DEIMOS data using the `spec2d` pipeline developed by the DEEP2 team (Cooper et al. 2012; Newman et al. 2013a). The pipeline cuts out the spectrally dispersed image of each slit from the raw data. The image is flat fielded, and a two-dimensional wavelength solution is calculated from an exposure of He, Ne, Ar, and Xe arc lamps. The stellar spectrum is extracted and made into a sky-subtracted, wavelength-calibrated, one-dimensional spectrum. We made some improvements to the pipeline appropriate for our purposes. For example, the procedure for defining the extraction window was optimized for extracting unresolved stars rather than extended galaxies (Simon & Geha 2007b).

3.2.3 Radial Velocity Measurements

We measured radial velocities for each star by comparing the spectra with a set of template spectra measured with DEIMOS. We adopted this procedure from Simon & Geha (2007b), who also obtained the template spectra that we used. The velocities were calculated from the wavelength shift in log space that minimized χ^2 between the target and template spectra. This procedure is similar to a cross-correlation (Tonry & Davis 1979), but it also takes into account variance in the observed spectrum.

We checked each radial velocity measurement by plotting the template spectrum on top of the target spectrum shifted into the rest frame. In several cases, the velocity measurement clearly failed, and the spectra did not line up. The typical cause was an artifact at the edge of the target spectrum. In these cases, we masked out the offending region of the spectrum and repeated the velocity measurement.

We calculated velocity errors by resampling the target spectrum 1000 times. In each Monte Carlo trial, we constructed a new spectrum by perturbing the original flux value. The magnitude of the perturbation was sampled from a Gaussian random distribution with a variance equal to the variance estimated for that pixel by `spec2d`. The velocity error was equal to the standard deviation of all of the Monte Carlo trials. Simon & Geha (2007b) found from repeat measurements of the same stars that this statistical error was an incomplete description of the total error. Following their example, we calculated the total error by adding a systematic error of 2.2 km s^{-1} in quadrature with the Monte Carlo statistical error.

3.2.4 Metallicity Measurements

We measured metallicities by comparing the continuum-normalized observed spectra to a grid of synthetic spectra. This procedure is identical to that of Kirby et al. (2008, 2010). We started

with a guess at the effective temperature, surface gravity, and metallicity of the star by combining the stars' colors and magnitudes with theoretical isochrones. The temperature and metallicity were allowed to vary to minimize χ^2 between the observed spectrum and the synthetic grid. Our measured value of [Fe/H][2] is the one that minimized χ^2.

Errors on [Fe/H] were estimated from the diagonal terms of the covariance matrix. This is an incomplete estimate of the error, largely due to covariance with temperature. Kirby et al. (2010) found that adding a systematic error of 0.11 dex in quadrature with the statistical error is an adequate estimate of the error. We adopted the same approach.

3.2.5 dSph Membership

We determine tentative membership with the combination of spectral line features and color-magnitude selection. Due to M dwarfs have strong, highly damped Na I doublets by virtue of their high surface gravities. Giants have weaker doublets. The equivalent width of the doublet increases very sharply for stars with $\log g > 4.5$ (see Figure 6 of Kirby et al. 2012). Therefore, we rejected any stars displaying strong Na I doublets with large damping wings.

Each observing epoch (2009, 2010, and 2012) had a different selection process (including both different photometric data and theoretical isochrones) to differentiate UMi and MW stars. We minimize some uncertainties by applying the same isochrones ($[\mathrm{Fe/H}] = -2$, 10 Gyr isochrones from Dotter et al. (2008)) to each photometric data set and utilizing g-i vs r color magnitude diagrams instead of g-r vs r for the 2010 SDSS selection. After examining the velocities we found the 2012 selection was too loose and the 2009, 2010 epochs too generous; we therefore adopt final color cuts in between. The final red giant branch (RGB) cuts are: 0.18 redder and 0.09 bluer from V-I for Bellazzini et al. (2002a); Palma et al. (2003a) stars, 0.20 redder and 0.15 bluer in g-i vs r for Abazajian et al. (2009); Aihara et al. (2011a) stars, and 0.06 redder, 0.12 bluer from a g-r vs

[2] $[\mathrm{Fe/H}] = \log \frac{n(\mathrm{Fe})/n(\mathrm{H})}{n_\odot(\mathrm{Fe})/n_\odot(\mathrm{H})}$ where n is atomic number density.

r for Muñoz et al. (in prep.) stars. Larger blue horizontal branch windows were applied: a box between $19 < \mathrm{I} < 20.5$ and $-0.2 < \mathrm{V} - \mathrm{I} < 0.5$ for Bellazzini et al. (2002a); Palma et al. (2003a) stars, 0.4 magnitude from the horizontal branch of M13 for (Abazajian et al. 2009; Aihara et al. 2011a) stars, and within 0.1 magitude if $0.0 < \mathrm{g} - \mathrm{r} < 0.55$ and 0.3 if $\mathrm{g} - \mathrm{r} < 0.0$ for Muñoz et al. (in prep.) stars. The stars: s0516520, s4958062, s0516121, 2783671763197, 2783671763111, 1337533907250, and 1338070515785 are removed due to spectral features. Any remaining Milky Way (MW) contaminants are removed statistically by including a MW foreground model (see Section 3.3.1).

3.2.6 Repeat Measurements

Due to the inhomogeneous nature of our photometric catalogs, we determine stars with multiple measurements by matching stars within $1''$ of one another. We find 107 stars with two spectral measurements and 9 stars with three measurements. We define the normalized difference as $\delta_{v,12} = (v_1 - v_2)\sqrt{\varepsilon_1^2 + \varepsilon_2^2}$. In Figure 3.3, we bin the normalized difference of the line-of-sight velocity and metallicity. Magenta and cyan bins refer to two and three repeated measurements respectively. Overlaid is the expected Gaussian distribution (with a dispersion of 1). The tails could be due to unresolved binary stars. We exclude the stars with $\delta_{v,12} > 10$ from the analysis. Two stars have repeated measurements from within the same observation epoch ('Bel10018' and 's9665803') while the last is between the 2010 and 2012 epochs.

In Figure 3.4, we compare the line-of-sight velocities and metallicities. The righthand panel compares the first to the second (or third) measurement. The middle panel displays a zoomed in region centered on the average velocity of the UMi. The left-hand panel compares metallicity measurements. In all panels, the one-to-one line is shown. The repeated measurements agree with one another within errors.

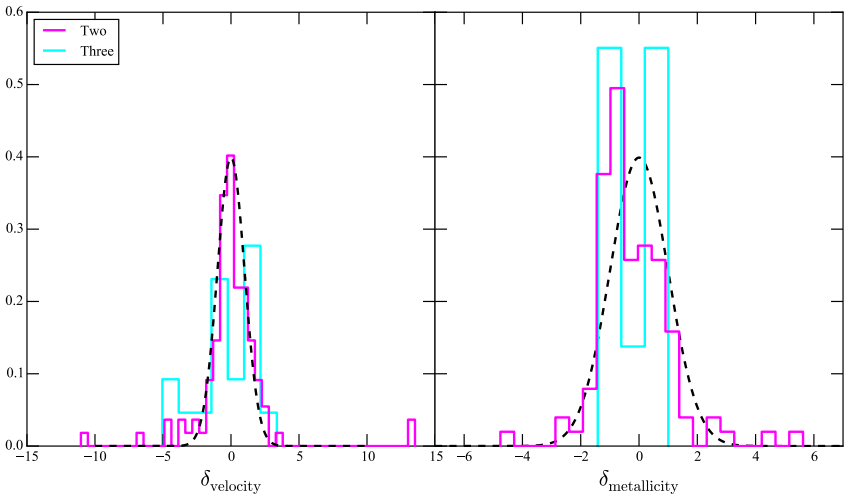

Figure 3.3: The binned line-of-sight velocity difference normalized by the average error for stars with repeated measurements ($\delta_{\rm velocity}$). The expected difference is Gaussian with a dispersion of 1. The outliers with a normalized difference greater than 10 are excluded from our analysis. The distribution is potentially widened due to binary stars.

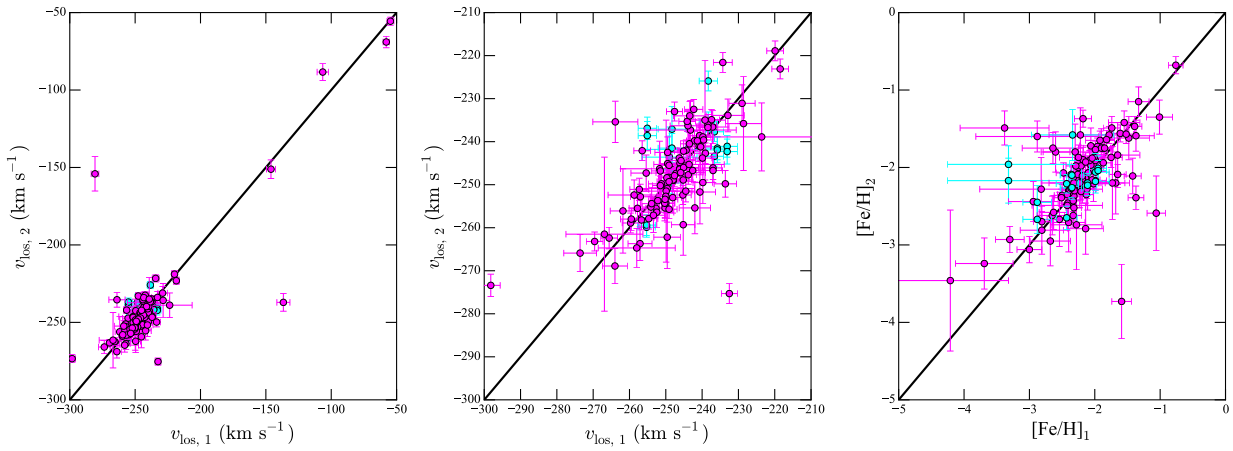

Figure 3.4: Comparison of first line-of-sight velocity and [Fe/H] measurements compared to additional measurements. Stars with two (three) measurements are magenta (cyan). The line denotes one-to-one measurements. **Left:** Line-of-sight velocity for all stars with repeated measurements. **middle:** Zoom-in velocity region centered around UMi lline-of-sight velocity. **right:** Comparison of [Fe/H] for repeated measurements.

3.3 Multi-Population Methodology

To disentangle chemo-dynamical populations, we need a statistical framework and a method for model selection. This analysis builds upon the statistical framework of WP11 by extending both the stellar distribution and selection function to axisymmetric systems and by including a dynamical Milky Way model. We address the significance of additional populations by computing the Bayes' Factor between single and multi-population models (see Section 3.3.4).

The probability of observing a data point, $\boldsymbol{x}_i$, assuming a particular hypothesis or model, H, characterized by parameters, $\mathscr{M}$, is given by the likelihood: $\mathscr{L}(\boldsymbol{x}_i|\mathscr{M}) = \mathscr{P}(\boldsymbol{x}_i|\mathscr{M},H)$. This generalizes to a data set: $\boldsymbol{x} = \{\boldsymbol{x}_i\}$ and $\mathscr{L}(\boldsymbol{x}|\mathscr{M}) = \prod_i \mathscr{L}(\boldsymbol{x}_i|\mathscr{M})$. We are interested in solving for the model parameters, found by determining the posterior distribution, $\mathscr{P}(\mathscr{M}|\boldsymbol{x},H)$. The posterior and likelihood are related via Bayes' Theorem:

$$\mathscr{P}(\mathscr{M}|\boldsymbol{x},H) = \frac{\mathscr{L}(\boldsymbol{x}|\mathscr{M})Pr(\mathscr{M},H)}{\mathscr{P}(\boldsymbol{x},H)}, \tag{3.1}$$

where $Pr(\mathscr{M},H)$, is the prior distribution representing any previously known information about the model under consideration and $\mathscr{P}(\boldsymbol{x},H)$, is the marginal likelihood, a normalizing factor. The marginal likelihood is commonly referred to as the Bayesian Evidence in Astrophysics. It is given by:

$$Z = \mathscr{P}(\boldsymbol{x},H) = \int_{\mathscr{M}} \mathscr{P}(\boldsymbol{x}|\mathscr{M},H)Pr(\mathscr{M})d\mathscr{M}. \tag{3.2}$$

For parameter estimation, computing the normalization is unnecessary but it is useful for model

selection (see Section 3.3.4).

The likelihood of observing a star in a dSph containing two stellar components containing a Milky Way background is (e.g. Martinez et al. 2011; Walker & Peñarrubia 2011a):

$$\mathscr{L}(\boldsymbol{x}_i|\mathscr{M}) = f_{\rm MW}\mathscr{L}_{\rm MW}(\boldsymbol{x}_i|\mathscr{M}_{\rm MW}) + f_1\mathscr{L}_1(\boldsymbol{x}_i|\mathscr{M}_1) + f_2\mathscr{L}_2(\boldsymbol{x}_i|\mathscr{M}_2)\,, \tag{3.3}$$

where the subscript in $\mathscr{L}$ and f refers to the corresponding population and $\mathscr{M} = \{\mathscr{M}_{\rm MW}, \mathscr{M}_1, \mathscr{M}_2\}$. For brevity, we drop $|\mathscr{M}$ from the likelihood argument for the reminder of the section. The MW subscript denotes the foreground model which is discussed in more detail in the following subsection. The fractions are enforced to be: $f_{\rm MW} + f_1 + f_2 = 1$. This method can be extended to additional populations with the constraint $\sum_{i=1}^{\rm N_{pop}} f_i = 1$ (e.g. Amorisco & Evans 2012c).

For our analysis, we consider the datum point, $\boldsymbol{x}_i = (x, y, v_{\rm los}, \varepsilon_{\rm los}, m, \varepsilon_m)_i$, containing spatial, velocity, and metallicity information. We refer to a general metallicity tracer as m in this section. Our analysis utilizes measurements of the iron abundance, [Fe/H]. Other works have utilized different metallicity tracers, for example, the Ca II triplet (Battaglia et al. 2008a), or the ΣMg index (WP11).

We assume that the spatial, velocity, and metallicity likelihoods in a stellar population in a dSph are independent of one another, therefore:

$$\mathscr{L}_n(\boldsymbol{x}_i) = \mathscr{L}_n^{\rm velocity}(v_i, \varepsilon_{{\rm los},i})\mathscr{L}_n^{\rm spatial}(x_i, y_i)\mathscr{L}_n^{\rm metallicity}(m_i, \varepsilon_{m,i})\,, \tag{3.4}$$

where the superscript refers to the likelihood for the velocity, spatial, or metallicity distributions. We model the velocity and metallicity likelihoods as Gaussian distributions. The velocity likeli-

hood of a population with average line-of-sight velocity, $\overline{v}$, and velocity dispersion, $\sigma_{\rm los}$, is:

$$\mathscr{L}^{\rm velocity}(v_i, \varepsilon_{{\rm los},i}) = \frac{1}{\sqrt{2\pi(\sigma_{\rm los}^2 + \varepsilon_{{\rm los},i}^2)}} \exp\left[-\frac{1}{2}\frac{(v_i - \overline{v})^2}{\sigma_{\rm los}^2 + \varepsilon_{{\rm los},i}^2}\right]. \tag{3.5}$$

We assume that there is no offset in average line-of-sight velocity between the two populations, $\overline{v} = \overline{v_1} = \overline{v_2}$, and assume that the stars within each population have an isothermal distribution. The metallicity distribution form is identical to Equation 3.5 with the velocity data replaced with metallicity data and $\overline{v} \rightarrow \overline{m}$ and $\sigma_{\rm los} \rightarrow \sigma_m$.

The likelihood for the spatial distribution is:

$$\mathscr{L}^{\rm spatial}(x_i, y_i) = \frac{S(x_i, y_i)\Sigma(x_i, y_i)}{\int S(x,y)\Sigma(x,y)dA}\,, \tag{3.6}$$

where $\Sigma(x,y)$ is the projected stellar distribution and S(x,y) is the selection function (Wang et al. 2005, WP11). The denominator insures that the positional likelihood is normalized and acts as a weight for spatial profile reconstruction (WP11). We use an elliptical Plummer profile for the projected stellar distribution (Plummer 1911):

$$\Sigma(x,y) = \frac{1}{q\pi r_h^2}\frac{1}{\left(1 + R_e^2/r_h^2\right)^2}\,, \tag{3.7}$$

where $R_e = (x^2 + y^2/q^2)$ is the elliptical radius, r_h is the stellar half-light radius, and q is the axis ratio. The Plummer profile is normalized such that $\int {\rm d}x{\rm d}y\Sigma(x,y) = 1$.

In summary, our method concurrently calculates the velocity, metallicity, and spatial properties of two dSph stellar populations in a Milky Way background. It contains 13 free parameters: 3 parameters in the velocity likelihood: $\bar{v}$, $\sigma_{v,1}$, and $\sigma_{v,2}$; 4 parameters to characterize the metallicity distribution: m_1, m_2, $\sigma_{m,1}$, and $\sigma_{m,2}$; 4 parameters for the spatial components: $r_{h,1}$, q_1, $r_{h,2}$, and q_2; and two parameter to distinguish the relative sizes of the stellar populations: f_2, $f_{\rm MW}$. The parameters and prior ranges are summarized in Table 3.3. In Section 3.4.4 we explore extensions to the metallicity, spatial, and velocity likelihoods.

3.3.1 Milky Way Distribution

The velocity and metallicity distributions for the Milky Way are non-Gaussian as the Milky Way is itself a multi-component system. Assuming the metallicty, spatial, and velocity distributions are independent for the Milky Way, the likelihood is:

$$\mathscr{L}_{MW}(\boldsymbol{x}_i) = \mathscr{P}_{\rm Bes}^{\rm velocity}(v_i)\,\mathscr{P}_{\rm Bes}^{\rm metallicity}(m_i)\,\mathscr{P}^{\rm spatial}(x_i, y_i). \tag{3.8}$$

The velocity and metallicity distributions are constructed by drawing stars from the Besançon model[3] at UMi's location (Robin et al. 2003). The same color-magnitude cuts as Section 3.2.5 are applied to the Besançon stars [4]. The remaining Besançon stars form the velocity and metallicity distributions of the Milky Way background in the UMi field. We smooth the velocity distribution;

[3] `http://model.obs-besancon.fr/`

[4] Three different Besançon models constructed are constructed corresponding to the three different photometric systems used: V-I vs I, g-i vs r, and g-r vs r. Each set is weighted by the number of spectroscopic observations within the color-magnitude cuts.

the probability for observing a MW star with velocity, v, (assuming no observation error) is:

$$\mathscr{P}_{\rm Bes}^{\rm velocity}(v) = \sum_{j=1}^{N_{Bes}} \frac{w_j}{\sqrt{2\pi k_v^2}} \exp\left[-\frac{\left(v-v_j\right)^2}{2k_v^2}\right]. \tag{3.9}$$

Where k_v is the velocity smoothing parameter and w_j is the weight each Besançon star is assigned. A similar distribution follows for the metallicity distribution. In Figure 3.5, we bin the velocity (left) and metallicity (right) of the Besançon stars. Overlaid is the smoothed distribution from Equation 3.9. Dotted cyan lines show the approximate location of the UMi.

When including the observational error, Equation 3.9 is convoluted with a Gaussian error kernel:

$$\begin{aligned}\mathscr{P}_{\rm Bes}^{\rm velocity}(v_i, \varepsilon_{{\rm los},i}) = &\int_{-\infty}^{+\infty} \frac{\mathrm{dv}}{\sqrt{2\pi\varepsilon_i^2}} \exp\left[-\frac{(v-v_i)^2}{2\varepsilon_i^2}\right] \\ &\times \sum_{j=1}^{N_{\rm Bes}} \frac{w_j}{\sqrt{2\pi k_v^2}} \exp\left[-\frac{\left(v-v_j\right)^2}{2k_v^2}\right].\end{aligned} \tag{3.10}$$

The integral is analytic:

$$\mathscr{P}_{\rm Bes}^{\rm velocity}(v_i, \varepsilon_{{\rm los},i}) = \sum_{j=1}^{N_{\rm Bes}} \frac{w_j}{\sqrt{2\pi\left(\varepsilon_{{\rm los},i}^2 + k_v^2\right)}} \exp\left[-\frac{\left(v_i-v_j\right)^2}{2\left(\varepsilon_{{\rm los},i}^2 + k_v^2\right)}\right]. \tag{3.11}$$

The summation can be precomputed for each observed star once the smoothing scale and Besançon

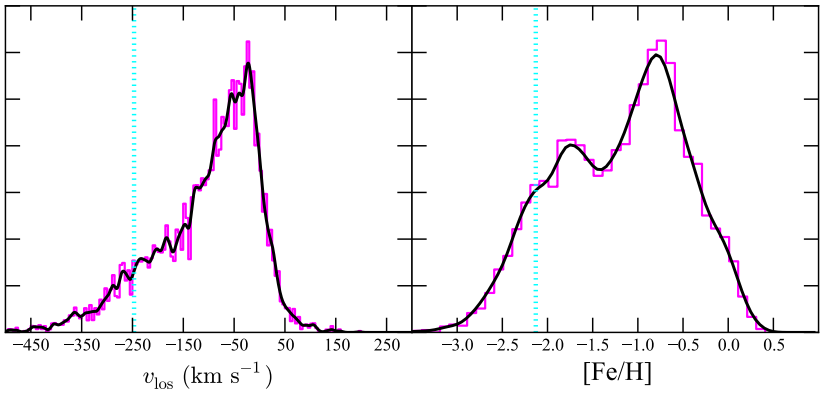

Figure 3.5: The binned velocity (right) and metallicity (left) distributions of stars from Besançon model in UMi field within the same color-magnitude cuts. Overlaid each distribution is the smoothed model from Equation 3.9. The smoothing scales are 5 km s^{-1} and 0.1 dex for the velocity and metallicity distributions respectively. The literature values of the velocity and metallicity of UMi are plotted in dotted cyan lines from McConnachie (2012).

distribution are determined. The metallicity distribution has a similar form:

$$\mathscr{P}_{\rm Bes}^{\rm metallicity}(m_i,\varepsilon_{m,i}) = \sum_{j=1}^{N_{\rm Bes}} \frac{w_j}{\sqrt{2\pi\left(\varepsilon_{m,i}^2+k_m^2\right)}} \exp\left[-\frac{\left(v_j-v_i\right)^2}{2\left(\varepsilon_{m,i}^2+k_m^2\right)}\right]. \tag{3.12}$$

We fix the smoothing scale parameters, k_v and k_m, to 5 km s^{-1} and 0.1 dex respectively. The spatial probability is assumed to be uniform throughout the observed area but the selection function still needs to be considered:

$$\mathscr{P}^{\rm spatial}(x_i,y_i) = \frac{S(x_i,y_i)}{\int S(x_i,y_i)dA}. \tag{3.13}$$

With fixed smoothing scale parameters, the only free parameter of the MW model is the normalization factor, $f_{\rm MW}$.

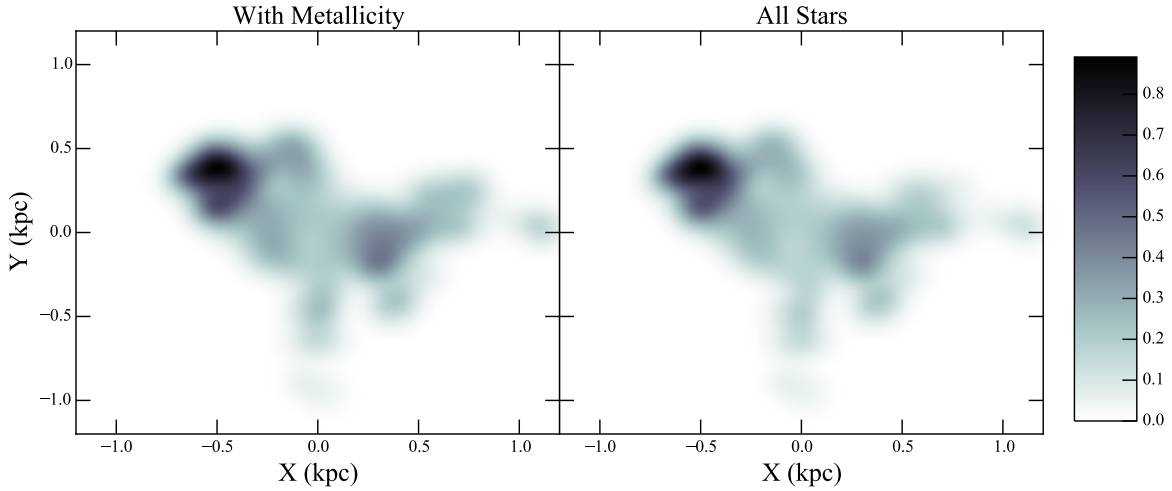

Figure 3.6: The spatial selection function for UMi. It represents the transformation from the spectroscopic spatial distribution to intrinsic spatial distribution. Regions with a larger value are well sampled spectroscopically. The smoothing scale length is set to 75 pc and we align the x-axis with the major axis. **right:** Stars with velocity measurements **left:** Stars with metallicity and velocity measurements; roughly 100 fewer.

3.3.2 Selection Function

Due to limited telescope time, not all spectroscopic candidates can be observed. The spatial distribution of stars with spectroscopic measurements generally does not follow the intrinsic spatial distribution of stars. The selection function, S, acts as a mapping between the observed and intrinsic spatial distribution of stars (Wang et al. 2005, WP11).

For a set of observed stars, $N_{\rm obs}$, drawn from a number of candidate stars, $N_{\rm cand}$, the selection function at each stellar position is:

$$S(x,y) = \frac{d\mathrm{N}_{\rm obs}(x,y)}{d\mathrm{N}_{\rm cand}(x,y)} \approx \frac{\sum_{i=1}^{\mathrm{N}_{\rm obs}} exp\left[-\frac{1}{2}\frac{(x_i-x)^2+(y_i-y)^2}{k^2}\right]}{\sum_{i=1}^{\mathrm{N}_{\rm cand}} exp\left[-\frac{1}{2}\frac{(x_i-x)^2+(y_i-y)^2}{k^2}\right]}, \tag{3.14}$$

where k is the smoothing scale (WP11). $N_{\rm cand}$ are all stars within the Umi field-of-view that fall

within the photometric selection in Section 3.2.5 while $N_{\rm obs}$ are all spectroscopically observed stars within the same color-magnitude selection. We use the projected spatial positions (x,y) instead of the projected radial positions ($R = \sqrt{x^2+y^2}$) because Umi is more aspherical than Fornax and Sculptor ($\varepsilon = 0.56$ compared to $\varepsilon = 0.3, 0.32$ Irwin & Hatzidimitriou 1995). In addition, different stellar populations will not necessarily have the same axis ratio. To removed stars repeated between photometric catalogs, we combine all stars within $1''$ of one other.

To set k, we construct and observe mock data sets with different values of k ranging from 25 to 400 parsecs ($1'$ to $18'$ at $d = 76$ kpc). We find, that for spherically symmetric systems, the choice of k, does not make an appreciable difference[5]. Whereas, for axisymmetric systems, an incorrect choice in k will strongly bias the recovered structural parameters. Our tests, with Umi-like mock data[6], show that $50\,{\rm pc} \leq k \leq 75\,{\rm pc}$ ($2' \leq k \leq 3'$) correctly recovers structural parameters. A larger choice of k will bias the structural posteriors. The spatial scale will be underestimated and q overestimated. The spatial bias increases as k increases.

In Figure 3.6, we plot the selection function we use for the Umi analysis with $k = 75$ pc. We align the x-axis and the major axis (the angle between the x-axis and the major axis, is measured East from North, and is $\theta = 53^\circ$ Irwin & Hatzidimitriou 1995). We fix $k = 75$ pc for the main analysis.

The selection function also impacts the fraction of observed stars within each population. In Equation 3.3, f_2 is the fraction of stars in population 2 within the observed sample. To recover the intrinsic fraction of stars in population 2, $f_{T,2}$, we need to consider the distribution of stars. The total normalization of the stellar profile of population n with and without the selection function is: $M_n = \int_0^\infty \Sigma_n(x,y)dA$ and $M_n^S = \int_0^\infty \Sigma_n(x,y)S(x,y)dA$. The intrinsic fraction of stars in population 2

[5]WP11 reach the same conclusion.

[6]We create a dSph with similar properties to Umi and observe it with randomly placed rectangular "masks." In Section 3.3.5, we create a Umi-like observation pattern. This was not used for the selection scale tests.

is:

$$f_{T,2} = \frac{f_2 M_2 / M_2^S}{f_2 M_1 / M_1^S + (1 - f_2) M_2 / M_2^S} \tag{3.15}$$

This transformation is required to compare to posterior of f_2 to the input values in mock data sets.

3.3.3 Missing Data

There are 93 stars that pass our color-magnitude selection that do not contain metallicity measurements. These stars can still be included in the analysis provided they are properly handled. For data points without metallicity measurements, the metallicity term must be integrated out (i.e. all possible metallicity values are considered). As the dSph and MW metallicity likelihood terms are normalized to unity, integrating over all metallicity drops the terms from the likelihood. For example, integrating Eq. 3.9, over all m, results in $\int \mathrm{d}m \, \mathscr{P}_{\mathrm{Bes}}^{\mathrm{metallicity}}(m) = \sum_j w_j = 1$.

3.3.4 Sampler and Model Selection

We utilize the Multimodal Nested Sampling algorithm to compute the Bayesian evidence for each model considered (Skilling 2004b; Feroz & Hobson 2008; Feroz et al. 2009). The nested sampling algorithm transforms the multi-dimensional evidence integral (Equation 3.2) into a one-dimensional integral over the 'prior volume.' The integral is evaluated by sampling the likelihood in a decreasing sequence of prior volumes, assuming that the inverse of the prior volume exists and is a monotonically decreasing function. As a by-product of sampling the likelihood, the posterior is also computed (For a detailed description, see Feroz & Hobson 2008; Feroz et al. 2009).

The Bayes' factor compares the relative odds in favoring model A over model B after examining the data. It is the ratio of the evidences computed for each model (with the assumption that apriori both models are equally favored),

$$B_{AB} = \frac{\mathscr{P}(x, H_A)}{\mathscr{P}(x, H_B)} = \frac{Z_A}{Z_B}. \tag{3.16}$$

It naturally incorporates Occams' razor as larger or more complicated model spaces are penalized. We compute the Bayes' factor in log space; where $\ln B_{AB} = \ln B > 0$ favors model A and $\ln B < 0$ favors model B. We use Jefferys' scale to interpret the signficance of the Bayes' factor. The of regions of $\ln B =: 0 \rightarrow 1$, $1 \rightarrow 2.5$, $2.5 \rightarrow 5$, and > 5 correspond to inconclusive, weak, moderate, and strong significance respectively (see Trotta 2008). To address significance, we compute the Bayes' factors between single and two-component models.

To assign a star into a particular stellar population we compare the star's likelihood in that stellar population to the total likelihood. This can be interpreted as a membership probability for individual stars (Martinez et al. 2011; Pace et al. 2014). The membership, m_i, for star x_i, to be in population 1 is:

$$m_i(x_i) = \frac{f_1 \mathscr{L}_1(x_i)}{f_{MW} \mathscr{L}_{MW}(x_i) + f_1 \mathscr{L}_1(x_i) + f_2 \mathscr{L}_2(x_i)}. \tag{3.17}$$

Each star will have a probability distribution of membership, for practicality, we use the median membership. We will utilize $\ln B$ to compare models and membership to examine properties the stellar populations.

3.3.5 Tests with Mock Data

To verify our methodology, we examine mock data sets containing two stellar populations. We check detection by checking for parameter recovery and a significant Bayes' Factor.

We construct mock sets by drawing the positions, velocity, and metallicity from distributions matching the models in Section 3.3. Stellar spatial location are randomly selected according to an axisymmetric projected plummer distribution (Equation 3.6). The metallicities and velocities are drawn from Gaussian distributions assuming the mean and dispersion are constant within a population. The intrinsic values are observed by measuring them from a Gaussian centered on the intrinsic value with dispersion set by velocity and metallicity error pairs from the Umi data. Pairs are chosen because the accuracy of the velocity and metallicity measurements are not independent.

We construct five groups of mock data sets; summarized in Table 3.2. The first group is created to validate our methodology. The input metallicity, kinematics, and spatial distributions are chosen to not overlap. We additionally include a radial metallicity gradient of 0.1 $\mathrm{dex\,kpc^{-1}}$ to simulate data similar to a dSph. In each set, we observe 800 stars within 1 kpc. In all 10 mock sets, the two populations are detected with high significance. The average Bayes' Factor is $\ln B = 81.1$, and the minimum is $\ln B = 59.2$. We verify that the posteriors and input parameters match. We conclude that our methodology can detect two stellar populations.

We now specialize to mock sets that are observed in a Umi-like observation pattern to search for potential biases. Each mock set is placed at the same location as Umi and observed with the masks from Table **??**. We approximate a Keck/DEIMOS mask as a $5'$ by $16.7'$ box. Within each mask, we observe the same number of stars as Umi members within the actual mask.

Groups 2-4 have fixed parameters for $\sigma_{[\mathrm{Fe/H}]}$, $\bar{v}$, and f_2. We then either vary σ_v and $\langle[\mathrm{Fe/H}]\rangle$ or vary r_h and q. For each variation of parameters, 5 mock sets are constructed and observed. In group 2 and 3, we vary σ_v and $\langle[\mathrm{Fe/H}]\rangle$, in steps of $\Delta\sigma_v = 1.25\,\mathrm{km\,s^{-1}}$ and $\Delta\langle[\mathrm{Fe/H}]\rangle = 0.1$. In

Table 3.2: Parameter of the mock data sets. Groups 2-4 have varied properties. For all models we fix $\overline{v_1} = \overline{v_2} = 100\,\mathrm{km\,s^{-1}}$. σ_v is in units of $\mathrm{km\,s^{-1}}$ and r_h is kpc.

Group	Notes	$\sigma_{v,1}$	$\sigma_{v,2}$	$\langle[\mathrm{Fe/H}]\rangle_1$	$\langle[\mathrm{Fe/H}]\rangle_2$	$\sigma_{[\mathrm{Fe/H}],1}$	$\sigma_{[\mathrm{Fe/H}],2}$	$r_{h,1}$	$r_{h,2}$	q_1	q_2	$f_{T,2}$	N
1	Methodology Test	5.0	10.0	-2.0	-2.5	0.25	0.25	0.2	0.5	0.7	0.7	0.5	10
2	$\Delta\sigma = 1.25$, $\Delta\langle[\mathrm{Fe/H}]\rangle = 0.1$	8.0	8.0	-2.0	-2.0	0.25	0.25	0.25	0.5	0.5	0.5	0.5	125
3	$\Delta\sigma = 1.25$, $\Delta\langle[\mathrm{Fe/H}]\rangle = 0.1$	8.0	8.0	-2.0	-2.0	0.22	0.44	0.34	0.35	0.3	0.73	0.5	125
4	$\Delta r_h = 0.1$, $\Delta q = 0.1$	5.1	9.8	-2.1	-2.23	0.22	0.44	0.35	0.35	0.5	0.5	0.5	125
5	Best fit Umi parameters	5.1	9.8	-2.1	-2.23	0.22	0.44	0.34	0.35	0.3	0.73	0.5	100

Group 4, we vary the spatial parameters in steps of $\Delta r_h = 0.1$ (kpc) and $\Delta q = 0.1$.

To correctly infer the existence of two populations, there must be a separation in metallicity. For a parameter recovery there must also be a difference in σ_v. The posteriors of the structural parameters are biased for Umi-like observations. The axis ratio of the centrally concentrated population tends to be lower while the axis ratio of the extended population tends to be larger. The measured difference between half-light radii tends to be smaller than the input value. Averaged over 10 mock data sets, there is not an systematic offset between the Umi and random observations for [Fe/H] and σ. In Umi-like observations, there is a systematic offset for q and r_h in the posteriors of each stellar population. The centrally concentrated structural posterior is biased to smaller q values and larger r_h values. The opposite effect is observed for the extended population.

The last group has parameters selected to mimic the UMi results. We constructed and observed 100 sets with a Umi-like observation pattern. In all set, both stellar populations were detected with high significance. Structural offsets were observed in the posteriors.

In summary, our method can detect two stellar populations but the UMi–like observation pattern can introduce biases in the structural posteriors in multi-component analysis.

3.4 Results

3.4.1 Single Component Analysis

The center, position angle, and distance adopted in this analysis are: $(\alpha_o, \delta_o) = (15^{\rm h}09^{\rm m}08^{\rm s}5, +67^{\rm d}13^{\rm m}21^{\rm s})$ (J2000.0), $\theta = 53^\circ$ (Irwin & Hatzidimitriou 1995), and d=76 (kpc) (Carrera et al. 2002). The posteriors of the single component analysis are listed in the last column of Table 3.3.

In Figure 3.7, we show the derived membership probability versus spatial and chemodynamic

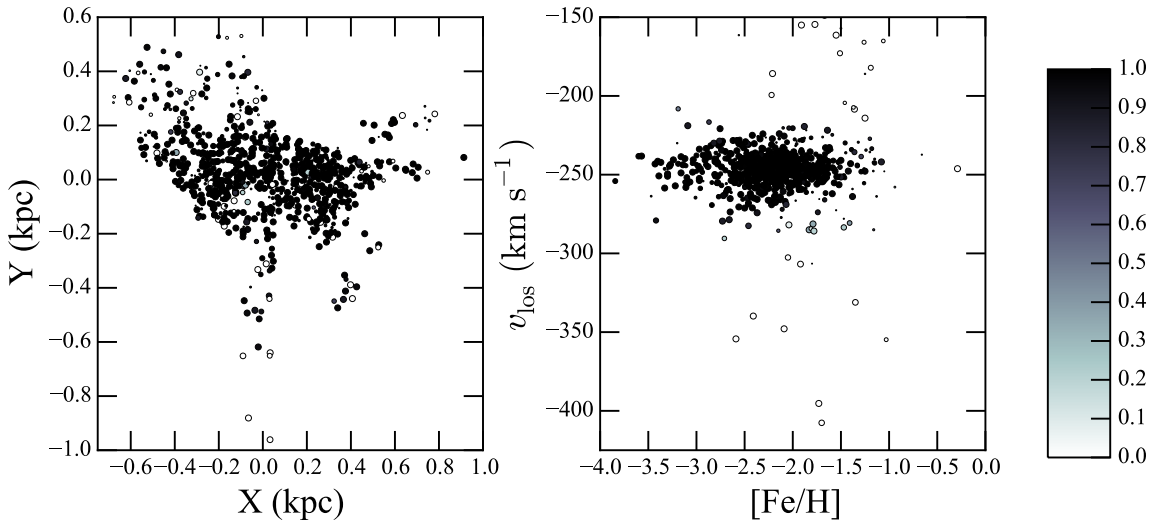

Figure 3.7: Position, velocity, and metallicity of stars in the UMi field. The colorbar denotes the membership probability to be an UMi member.

properties. The righthand figure shows the spatial distribution of observed stars (where the x-axis corresponds to the major axis) with stars shaded by the median probability to be a UMi member. The lefthand figure displays $\overline{v_{los}}$ versus [Fe/H] shaded by membership probability. The size of the points is inversely proportional to the velocity error. Our model places high (relative to Ursa Minor) metallicity stars into the Milky Way population.

3.4.2 Properties of the Two Stellar Populations

The parameters, priors, and posteriors of the single and two population analysis are listed in Table 3.3. We find, at high significance ($\ln B = 41.36$), two stellar populations with distinct chemical, kinematic, and spatial distributions. Although the metallicity distributions overlap, the two stellar populations have distinct distributions in kinematics, metallicity, and spatial positions. We will refer to the stellar populations as the metal rich and metal poor populations, in reference to the populations uncovered in Fornax and Sculptor (Battaglia et al. 2008a, Wp11).

In Figure 3.8, we show the distribution of stars weighted by their membership in each of the two

Table 3.3: Parameters, priors, and posteriors of the two component model for UMi. The last column displays the results for a one component model. The two component model is significantly favored over the single component with $\log B = 41.36$. See Section 3.3 for a description of the parameters. Extended models are explored in Section 3.4.4.

Parameter	Prior[a]	Units	Posterior	Single
$\overline{v}$	-230 - -260	$\mathrm{km\,s^{-1}}$	$-246.7^{+0.3}_{-0.3}$	$-246.9^{+0.4}_{-0.4}$
$\sigma_{v,MR}$	0 - 30	$\mathrm{km\,s^{-1}}$	$5.2^{+0.5}_{-0.5}$	$9.1^{+0.4}_{-0.3}$
$\sigma_{v,MP}$	0 - 30	$\mathrm{km\,s^{-1}}$	$13.8^{+1.0}_{-0.9}$	-
$\langle[Fe/H]\rangle_{MR}$	0 - -4.0[b]	dex	$-2.09^{+0.02}_{-0.02}$	$-2.18^{+0.02}_{-0.02}$
$\langle[Fe/H]\rangle_{MP}$	0 - -4.0[b]	dex	$-2.32^{+0.05}_{-0.05}$	-
$\sigma_{[Fe/H]}(MR)$	0 - 1	dex	$0.25^{+0.03}_{-0.03}$	$0.33^{+0.01}_{-0.01}$
$\sigma_{[Fe/H]}(MP)$	0 - 1	dex	$0.38^{+0.04}_{-0.04}$	-
f_2	0 - 1	-	$0.38^{+0.06}_{-0.05}$	-
f_{MW}	0 - 1	-	$0.08^{+0.01}_{-0.01}$	$0.09^{+0.01}_{-0.01}$
$r_{h,MR}$	0 - 1.2	kpc	$0.41^{+0.04}_{-0.03}$	$0.39^{+0.02}_{-0.02}$
q_{MR}	0 - 1	-	$0.28^{+0.03}_{-0.03}$	$0.44^{+0.03}_{-0.03}$
$r_{e,MR}$	-	kpc	$0.22^{+0.01}_{-0.01}$	$0.26^{+0.01}_{-0.01}$
$r_{h,MP}$	0 - 1.2	kpc	$0.36^{+0.04}_{-0.03}$	-
q_{MP}	0 - 1	-	$0.80^{+0.11}_{-0.10}$	-
$r_{e,MP}$	-	kpc	$0.32^{+0.03}_{-0.02}$	

a) All priors are uniform within the range specified. b) A hard cut prior in metallicity between the two stellar populations is chosen: $\langle[Fe/H]\rangle_{MR} > \langle[Fe/H]\rangle_{MP}$.

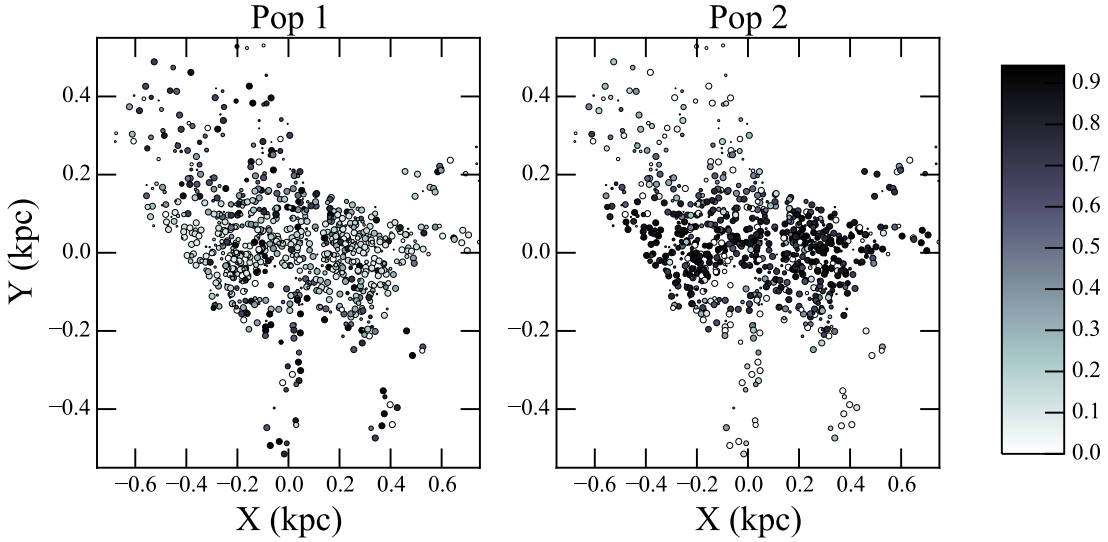

Figure 3.8: Spatial distribution of stars in the two stellar populations. The size of the points is inversely proportional to the velocity error. **right:** The colorbar denotes median membership probability for the metal poor population. **left:** Median membership to be in the metal rich population.

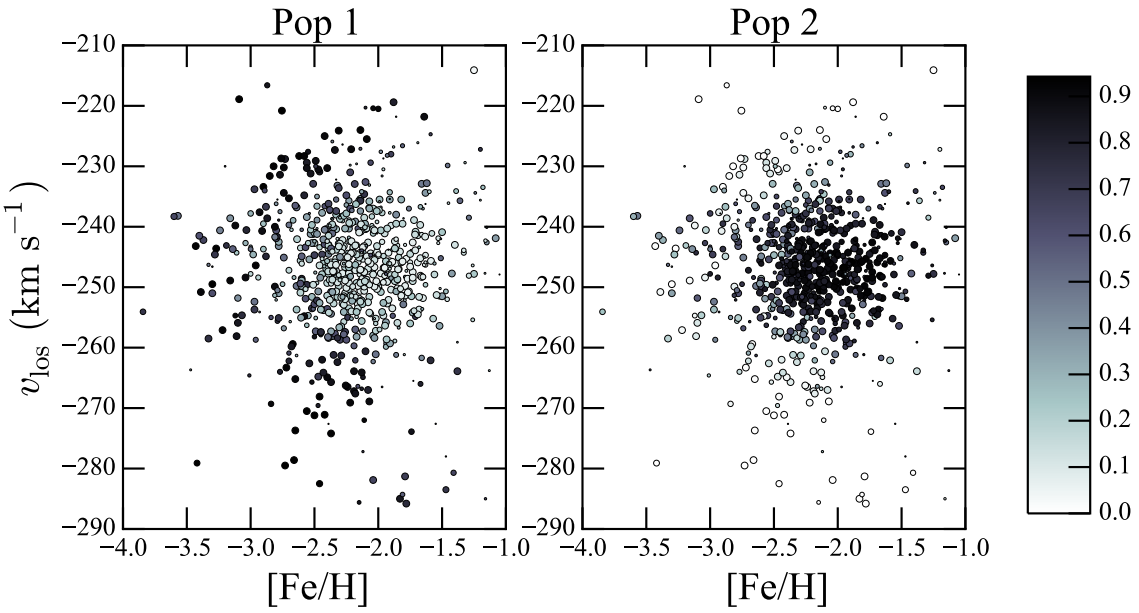

Figure 3.9: Comparison of the velocity and metallicity for stars in the two stellar populations. **right:** The colorbar denotes median membership probability for the metal poor population. **left:** Median membership to be in the metal rich population.

stellar population. The metal rich population is elongated and centrally concentrated but the central region is not devoid of stars in the metal poor population. From mock data observed in a Umi-like observation pattern, we found that the spatial parameters are likely biased. The axis ratios are biased towards smaller or larger values for the centrally concentrated and extended populations respectively. The measured separation in half-light radii is likely smaller than the intrinsic value. The metal rich population's extreme axis ratio is likely a result of the spatial bias introduced with a non-uniform observation pattern.

In Figure 3.9, we show velocity versus metallicity for all stars weighted by the membership probability for each stellar population. The metal rich population shows a distinct peak in the velocity-metallicity space. The metal poor population has large dispersions and many of the metal rich stars have a non-zero probability to be metal poor members.

We examine the radial properties of kinematics and metallicity by binning the metal poor and metal rich stars in elliptical radii ($\varepsilon = 0.56$) in Figures 3.10 and 3.11. We bin the data by sorting in

elliptical radii and creating bins when there the star's membership sums to 40. We find the velocity dispersion of the metal rich population is constant while the metal poor population decreases with radius (this excludes the anomalous bins from 500-700 pc). The average velocity is mostly constant but some bins display $\sim 5\,\mathrm{km\,s^{-1}}$ variation. Mock tests with various transverse velocity vectors show that this is likely due to the both exclusion of perspective motion in computing the average velocity and the radial projection. The average metallicities of both populations show a decrease with radius and they differ by ~ 0.2 dex within a given bin.

3.4.3 Null Tests for Calibrating $\ln B$

We address the detection of false positives by examining null data sets (mock data with a single stellar population). The creation of the null sets is identical to the mock sets in Section 3.3.5 and we observe all sets with a Umi-like observation pattern. All classical dSphs have a metallicity gradient (Kirby et al. 2011), therefore, we include a metallicity gradient in all null models. The functional form for the average metallicity we use is: $\langle[\mathrm{Fe/H}]\rangle(R_e) = \langle[\mathrm{Fe/H}]\rangle_0 + mR_e$, where $\langle[\mathrm{Fe/H}]\rangle_0$ is the metallicity at $R_e = 0$ and m is the radial metallicity gradient (in $\mathrm{dex\,kpc^{-1}}$).

The best fit single population parameters are used as the input values for the null data. The parameters[7] are: $\bar{v} = 100\,\mathrm{km\,s^{-1}}$, $\sigma_v = 8\,\mathrm{km\,s^{-1}}$, $[\mathrm{Fe/H}] = -2.17$, $\sigma_{[\mathrm{Fe/H}]} = 0.36$, $m = 0.2\,\mathrm{dex\,kpc^{-1}}$, $r_h = 0.34$ kpc, and $q = 0.49$. The value of the metallicity gradient is chosen by adding it as a free parameter to the single population model. We construct 100 null sets and model them with single and two component models. There are no null models that can mimic the two stellar populations uncovered in the Umi data. The distribution of null set Bayes' factors is: $\ln B = -0.69^{+1.95}_{-1.06}$ with a minimum and maximum of -2.28 and 7.1 respectively. Note that these null sets do not include a Milky Way background model.

[7]The metallicity gradient is found from an extended single component model.

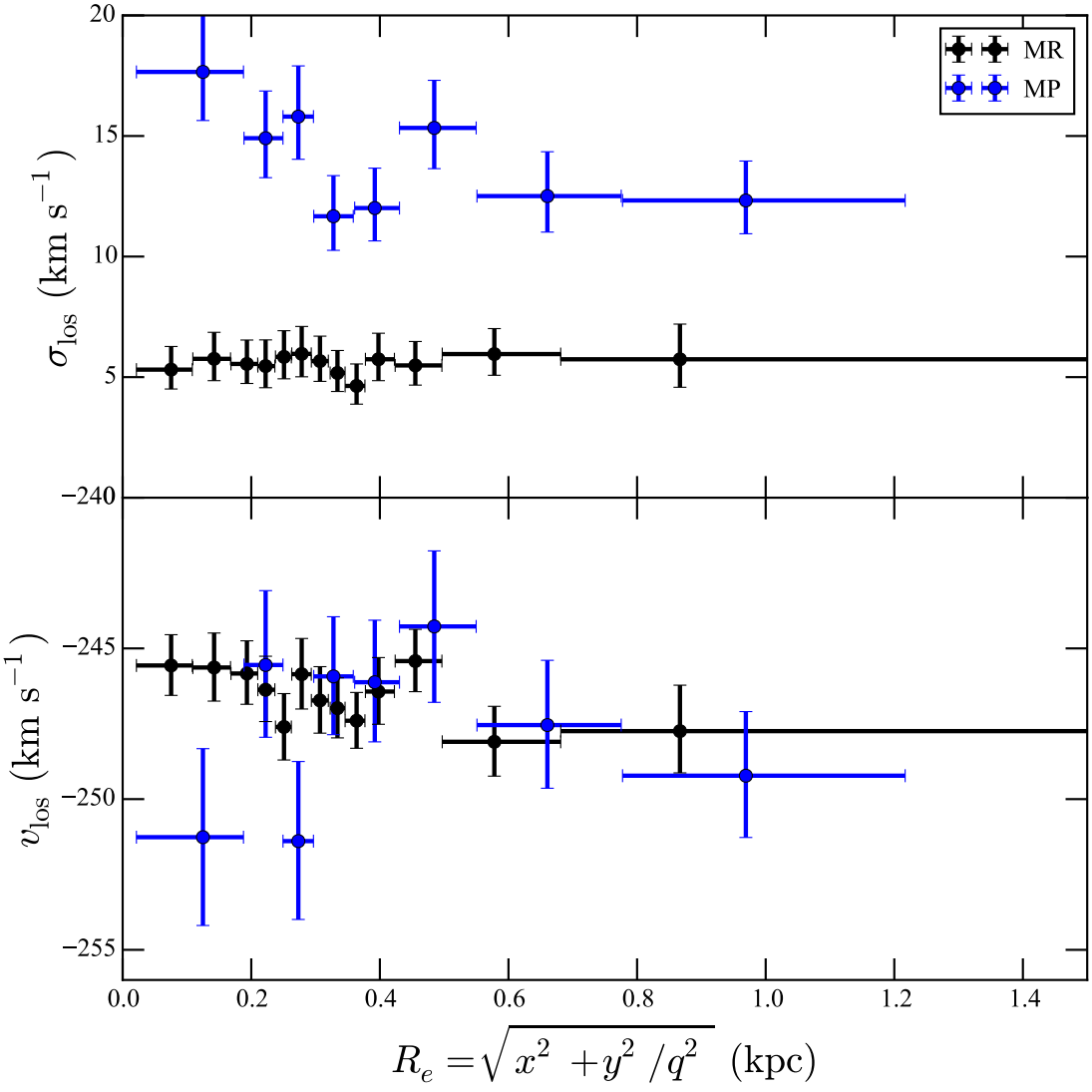

Figure 3.10: Properties of the kinematics with elliptical radius. The axis ratio is fixed to the photometric value ($\varepsilon = 0.56$). Each bin is contains 40 membership from the stellar population (metal rich or metal poor). The radial error bars denote the minimum and maximum radius of stars in the bin.

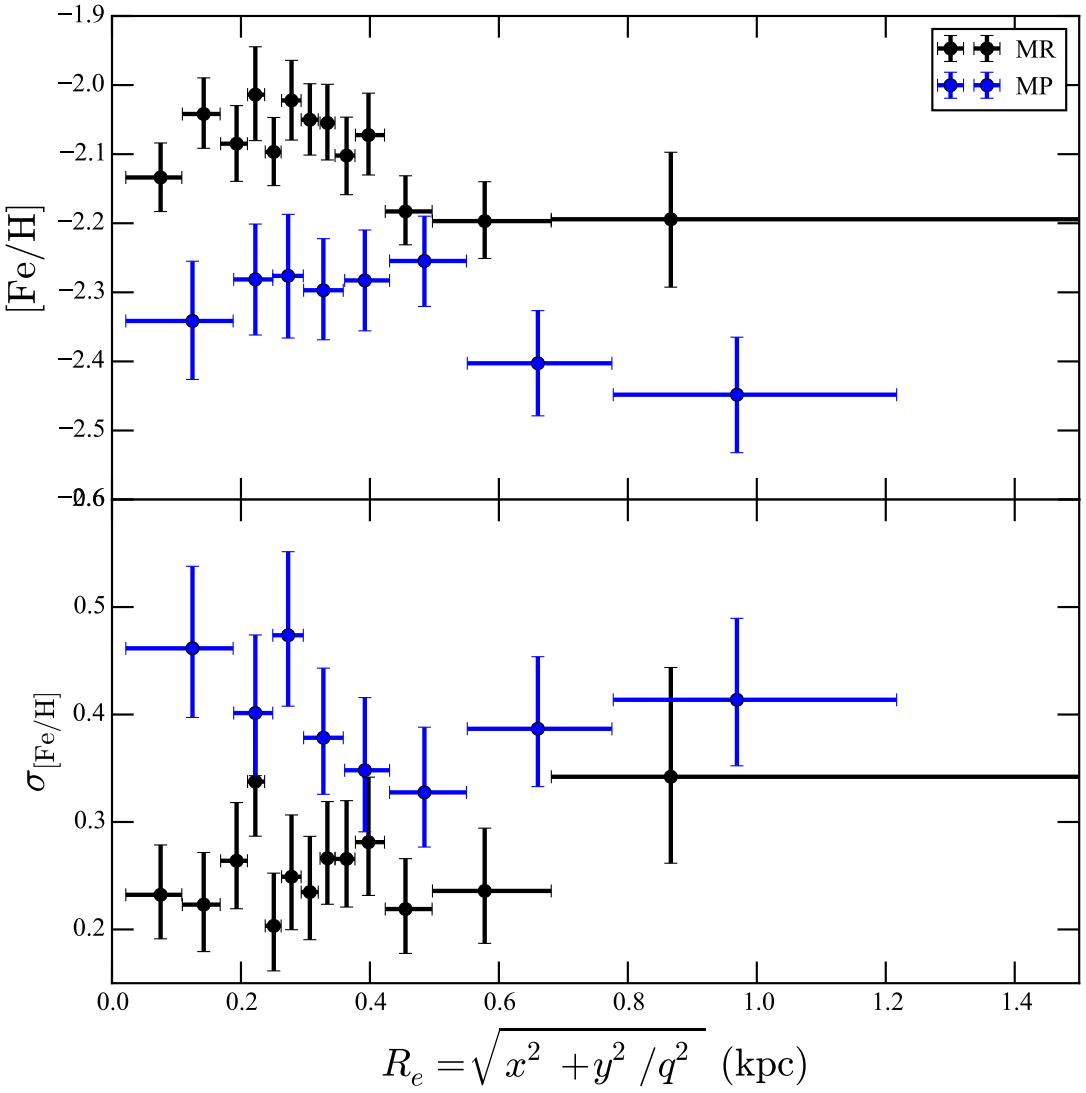

Figure 3.11: Properties of the metallicity parameters of each stellar population with elliptical radius. The construction of bins is the same as Figure 3.10.

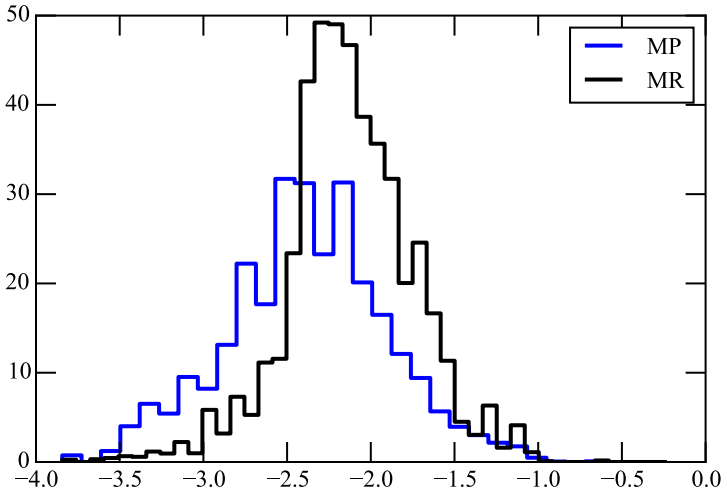

Figure 3.12: Metallicity Distribution of two stellar populations. The metal rich (MR) and metal poor (MP) populations are colored black and blue respectively. The metal rich population is non-Gaussian.

3.4.4 Model Extensions

We explore simple model extensions to better describe the properties of the two populations. In Figure 3.12, we show the binned metallicity distribution of each stellar population. The metal rich population has a clear non-Gaussian component that overlaps with the metal poor population. We explore a model where the metallicity distribution of the metal rich population is composed of two Gaussians: $\mathscr{L}(m,\varepsilon_m) = f_m \mathscr{N}(m_1,\sigma_{m,1}) + (1-f_m)\mathscr{N}(m_2,\sigma_{m,2})$, where $\mathscr{N}$ is the Gaussian distribution. This model better describes the data ($\ln \mathrm{B} = 6.4$). We measure $m_1 = -2.25^{+0.03}_{-0.03}$, $m_2 = -1.90^{+0.08}_{-0.07}$, $\sigma_{m,1} = 0.06^{+0.05}_{-0.04}$, $\sigma_{m,1} = 0.23^{+0.04}_{-0.06}$, and $f_m = 0.48^{+0.12}_{-0.13}$. The metallicity of the metal poor population does not change.

The metal poor population in Figure 3.10 has a falling velocity dispersion. We consider a model where each stellar population has a functional velocity dispersion parameterized by: $\sigma(R_e = \sqrt{x^2+y^2/q^2}) = \sigma_o \left(\frac{R_e}{R_\sigma}\right)^\alpha / \left(1+\left(\frac{R_e}{R_\sigma}\right)^\alpha\right)$. We measure: $\sigma_{v,1} = 10.7^{4.8}_{-3.1}\,\mathrm{km\,s^{-1}}$, $\sigma_{v,2} - \sigma_{v,1} = 17.1^{12.4}_{-9.5}\,\mathrm{km\,s^{-1}}$, $\log_{10} r_{s,1} = -0.4^{+1.0}_{-1.1}$, $\alpha_1 = 0.11^{+0.31}_{-.44}$, $\log_{10} r_{s,2} = 0.1^{+0.3}_{-0.4}$, and $\alpha_1 = -0.56^{+0.87}_{-.81}$. This results in a decreasing velocity dispersion for the metal poor population while the metal rich

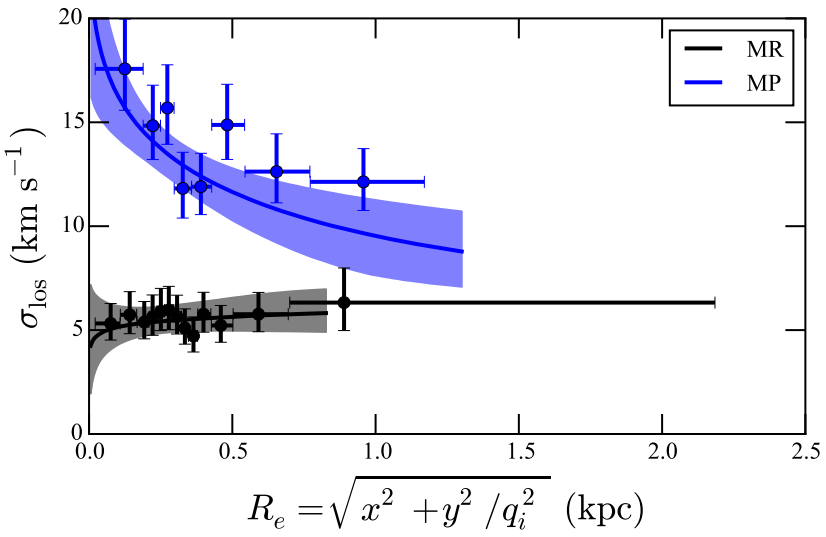

Figure 3.13: Velocity dispersion profiles of the two stellar populations. The lines and shaded bands show the median and $1-\sigma$ region. The binned distribution is the same as the top panel in Figure 3.10. The metal rich (MR) and metal poor (MP) populations are colored black and blue respectively.

population increases quickly in the center to a flat value. In Figure 3.13, we show the velocity dispersion profiles with this models. The line represents the median value while the shaded band is the $1-\sigma$ region. The velocity dispersions agree with the binned distribution in Figure 3.10. The stars assigned to each stellar population are not significantly changed by breaking the assumption of an isothermal velocity distribution.

Both model extensions are applied to the single component model. Neither model extension removes the detection of two chemodynamical populations. The model extensions illustrate that the detections are significant and that the kinematics may be more complicated than an isothermal velocity profile.

3.5 Slope of Dark Matter Profile

The measurement of the slope of the mass profile relies on the fact that the mass within the stellar half-light radius, $M_h = M(r_h)$, is well-determined for spherical systems (Walker et al. 2009c; Wolf et al. 2010)[8]. The difference in mass at the different half-light radii provides an estimate for the slope: $\Gamma = \Delta M_h / \Delta r_h$. Through mock data sets, WP11 argued that Γ is robust to systematics. Γ assumes spherical symmetry, we use the geometric mean of the major and minor axes as a "spherical" half-light radius to accommodate this assumption. In terms of model parameters the mass-slope is (a modified version of Equation 5 in WP11):

$$\Gamma = 1 + \frac{\log_{10}\left(\sigma_{v,1}^2 / \sigma_{v,2}^2\right)}{\log_{10}\left[\left(r_{h,1}\sqrt{q_1}\right) / \left(r_{h,2}\sqrt{q_2}\right)\right]}. \tag{3.18}$$

The benefit of this method is that no additional dynamical modeling is required; only quantities directly measured in our model are utilized in determining the mass slope. Note that Γ is not a direct measurement of the inner density profile (at $r = 0$) but a measurement of the average slope of the mass profile between r_h for the two populations. For a mass profile scaling as $M(r) \propto r^{-\gamma}$ in the central region, Γ places an upper limit on the density-slope as $\gamma < 3 - \Gamma$ (WP11). For an NFW profile: $\gamma = 1$, $\Gamma = 2$. For a constant density profile: $\gamma = 0$, $\Gamma = 3$.

We measure $\Gamma = 6.75^{+2.76}_{-1.51}$. This disfavors a cuspy NFW halo ($\Gamma = 2$) at greater than $3 - \sigma$ but almost the entirety of the posterior is within the region $\Gamma > 3$. We measure density-slope greater than zero (assuming $M(r) \propto r^{-\gamma}$), implying a system not in dynamical equilibrium or a break down of the mass-slope estimator. There are two systematics we have identified that affect this measurement. From the mock data tests in Section 3.3.5, we found that the spatial properties of

[8] This has been tested in a wide range of systems (Walker & Peñarrubia 2011a; Laporte et al. 2013; Kowalczyk et al. 2013; Lyskova et al. 2015; Campbell et al. 2016).

both populations are systematically offset. The metal rich population is generally less concentrated while the metal poor population is generally more concentrated. In Figure 3.10, we find the velocity dispersion of the metal poor population to decrease with radius. The invalidates the assumptions for the mass estimators but we estimate that it is overestimating the mass in the outer parts. Accounting for both of these systematics will lower Γ but it is unclear by how much.

Is Γ a robust measurement of the inner density slope? WP11 created mock data sets that contained two stellar populations drawn from Osipkov-Merritt distribution functions ($f(x,v) = f(E - L/2r_a^2)$). Cored and cuspy potentials and different stellar distribution were investigated. They concluded that their method tends to infer the value of Γ correctly or underestimate it (see Section 4 of WP11 for more details); a higher value of Γ implies the dark matter density profile is more core-like.

Laporte et al. (2013) also investigated this issue by embedding spherically symmetric stellar systems with isotropic velocity distributions into triaxial dark matter halos from cosmological simulations. They also found that the inferred Γ is either correct or underestimated. Note that the stellar populations in UMi are significantly aspherical.

The simulations of Kowalczyk et al. (2013) with axisymmetric stellar systems, in contrast, find that Γ can be either underestimated or overestimated by a factor of up to 2 depending on the viewing angle (major, minor, or intermediate axis). They create simulated dSphs with the tidal stirring mechanism (Mayer et al. 2001a,b). An initial rotation supported dwarf galaxy is transformed into a dispersion supported dSph by the Milky Way's tidal forces over several Gyrs. In contrast to the MW dSphs (except possibly Sculptor, see Battaglia et al. 2008a), many of their simulated dSphs still retain coherent rotation, even after 10 Gyrs. This rotation is excluded from their mass inference, which can bias the mass estimate. A similar set of simulated halos without remnant stellar rotation would be very useful to understand the true uncertainties in using Γ to estimate the average dark matter halo mass slope.

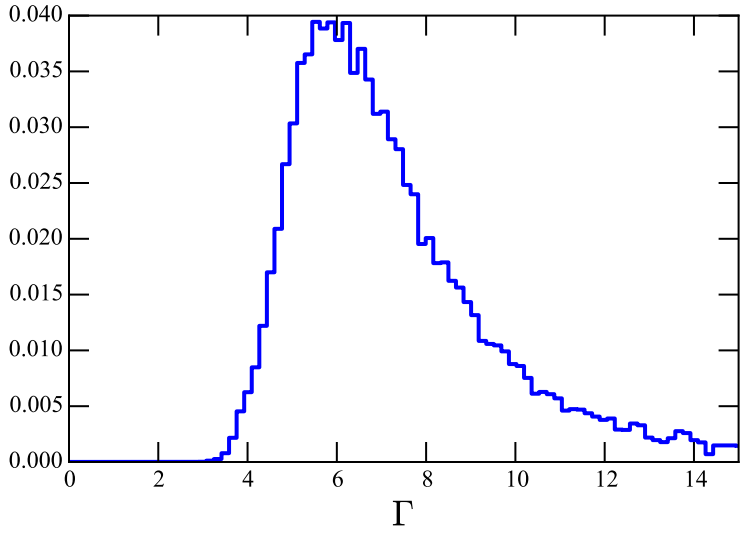

Figure 3.14: Posterior distribution of the slope of the mass profile for the standard analysis. The slope is calculated via Equation 3.18 (Equation 5 of WP11) with spherically averaged half-light radii.

It is clear that we need more simulations and mock data sets of aspherical systems to bracket the systematic uncertainty in the measurement of Γ. More realistic axisymmetric mass models with either Jeans models or distribution function models should also be considered to determine the slope of the mass profile in Umi but is beyond the scope of the present analysis.

3.5.1 Comparison to the Dynamics of other dSphs with Multiple Stellar Populations

Chemo-dynamical analyses similar in spirit to the present analysis have confirmed multiple stellar populations in Fornax and Sculptor (Tolstoy et al. 2004; Battaglia et al. 2008a; Walker & Peñarrubia 2011a; Hendricks et al. 2014). All three dwarfs contain a kinematically hot, spatially extended, and metal poor stellar population and a second stellar population that is kinematically cold, centrally concentrated, and metal rich [9]. To examine the mass profiles of dSphs as an en-

[9]In Carina, three stellar population have been uncovered (Kordopatis et al. 2016) and the metal rich and intermediate populations have velocity dispersions that do not follow the chemodynamical ordering. There are conflicting analysis on the state of chemodynamics in Carina (Wilkinson et al. 2006; Koch et al. 2006; Walker & Peñarrubia

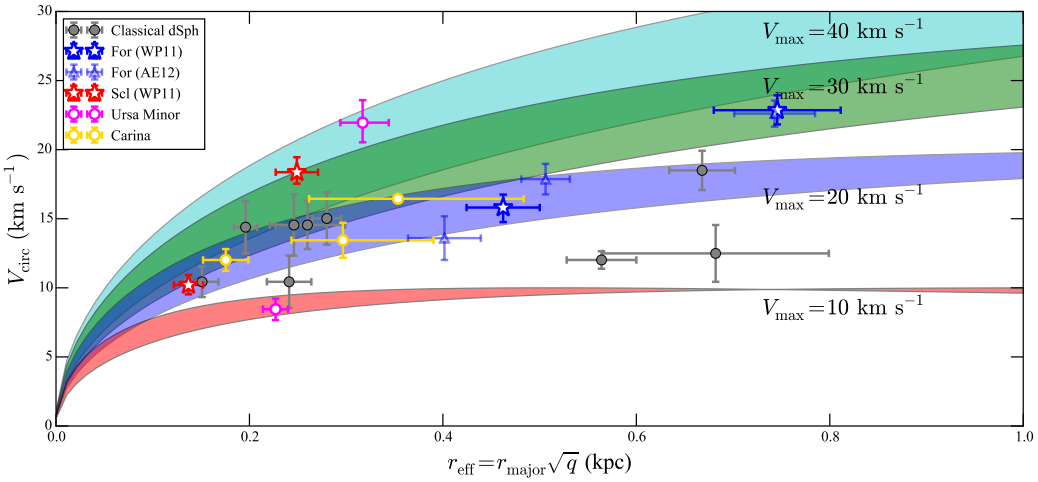

Figure 3.15: Elliptical radius $r_{\rm major}\sqrt{q}$ versus circular velocity for bright Milky Way dSphs. Multiple stellar populations are shown for Carina (gold Kordopatis et al. 2016), Fornax (blue; WP11 Amorisco & Evans 2012c), Sculptor (red; WP11), and Ursa Minor (magenta; this work). The bright dSphs (gray) are shown in gray (Walker et al. 2009c). The shaded bands are the $V_{\rm circ}$ profiles for NFW halos with $V_{\rm max} = 10, 20, 30, 40\,{\rm km\,s^{-1}}$. Some dSphs with multiple stellar populations display tension with NFW halos.

semble (both with and without confirmed multiple populations) we compare the inferred circular velocities ($V_{\rm circ}$) of the dSphs to predicted $V_{\rm circ}$ profiles of NFW halos. In Figure 3.15, we plot the half light radius r_h (geometric mean of the major and minor axes) versus $V_{\rm circ}$ for: Carina (gold), Fornax (blue), Sculptor (red), Umi (black), and all MW dSphs with $L > 10^5 L_\odot$ (gray). In shaded bands, we plot the predicted NFW halo $V_{\rm circ}$ profiles with $V_{\rm max} = 10, 20, 30, 40\,{\rm km\,s^{-1}}$. The uncertainties in the band correspond to scatter in the $R_{\rm max} - V_{\rm max}$ from Local Group simulations of Garrison-Kimmel et al. (2014c). The $V_{\rm circ}$ profiles of Fornax, Sculptor, and Umi are all in tension with NFW predictions in the way that Boylan-Kolchin et al. (2011b, 2012b) described. A cored halo can explain the slow rise but there are caveats to this resulting from the model assumptions (Strigari et al. 2014). Previous analyses of Sculptor and Fornax also favor cored dark matter profiles (Battaglia et al. 2008a; Walker & Peñarrubia 2011a; Amorisco & Evans 2012a; Agnello & Evans 2012; Amorisco et al. 2013).

2011a; Kordopatis et al. 2016; Fabrizio et al. 2015, 2016). We show the results of the Kordopatis et al. (2016) analysis in Figure 3.15

3.6 Conclusion

We have presented a new spectroscopic data set for the classical dSph Ursa Minor using the Keck/DEIMOS instrument. The data set contains the largest collection of the line-of-sight velocity and metallicity for Ursa Minor members ($N \sim 826$).

We have presented a new method for disentangling stellar populations in dSph galaxies. The method builds upon the work of WP11 by extending the analysis to axisymmetry and utilizes Bayesian evidence to compare models with and without multiple populations. We detect two chemo-dynamical stellar populations in Umi at high significance ($\ln B \sim 38$). The metal rich ($\langle [\mathrm{Fe/H}] \rangle \approx -2.1$) population has a kinematically cold velocity dispersion ($\sigma_v \approx 5\,\mathrm{km\,s^{-1}}$) compared to metal poor ($\langle [\mathrm{Fe/H}] \rangle \approx -2.32$) population ($\sigma_v \approx 13\,\mathrm{km\,s^{-1}}$). The metal rich population is more centrally concentrated and elongated than the metal poor population.

We are able exclude the hypothesis that Umi has one homogeneous chemo-dynamical population at greater than 99% confidence level. The properties of Umi are similar to Fornax and Sculptor. Each dSph has a centrally concentrated, metal rich, and kinematically cold stellar population and an extended, metal poor and kinematically hot stellar population.

Our methodology can be applied to search for chemo-dynamical structure in other dSphs with large spectroscopic data sets. We have tested our method and the influence of systematics using a large number of mock data sets. We urge caution in interpreting the preference for the significantly more elliptical surface density for the colder (centrally concentrated) population as our mock data analysis reveals that this inference is very sensitive to the selection function. This is an important area for future studies because differences in the shapes of surface densities of the metal-rich and metal-poor populations that are common across the different dSphs may provide hints about how the multiple populations arose.

We have summarized the mass measurements from the multiple populations in Carina, Fornax,

Sculptor and Ursa Minor, as well the single populations of the other classical Milky Way dSphs in Figure 3.15. The dark matter halo of Ursa Minor is inconsistent with an NFW form but this conclusion suffers from spatial systematics and has a decreasing velocity dispersion. This low density is symptomatic of the "too big to fail" problem (Boylan-Kolchin et al. 2011b, 2012b), which is clearly evident in Figure 3.15 and whose solution requires a mechanism to reduce the central dark matter densities of galaxies.

Chapter 4

Comparing rotation curve observations to hydrodynamic ΛCDM simulations of galaxies.

Based on Pace (2016)

4.1 Summary

The formation of the disk and feedback from supernova winds impacts the distribution of dark matter in galaxies. Recently, Di Cintio et al. (2014b) characterized the halo response from baryonic processes in hydrodynamical simulations via a dependence on the ratio of stellar-to-halo mass ($M_\star/M_{\rm halo}$). The (stellar) mass dependent halo profile links together the local and global properties of the halo (e.g. inner slope and $M_{\rm halo}$) which allows for measurements of $M_{\rm halo}$ without virial tracers. We compile a large sample of rotation curves from the literature to test this halo profile. We find that this halo profile can explain rotation curve observations over a wide range of $M_\star$. However, the global results from our sample are inconsistent with a Λ cold dark matter universe. We do not

find the expected correlation between the halo concentration and $M_{\rm halo}$ and there is significantly larger scatter than expected. Furthermore, a large portion of galaxies below $M_\star \sim 10^9 M_\odot$ are found to be hosted by smaller halos than expectations from the abundance matching technique. We find our results are robust to statistical priors and systematic effects such as inclination angle, asymmetric drift correction, data source, and uncertainties in stellar mass-to-light ratios. This suggests either a mischaracterization of the halo response due to baryonic processes or additional non-standard dark matter physics.

4.2 Additional Background

The Λ cold dark matter (ΛCDM) paradigm successfully explains the distribution of matter on large scales (e.g. the 2dF Galaxy Redshift Survey; Percival et al. 2001) by postulating that dark matter halos are the sites of galaxy formation (White & Rees 1978; Blumenthal et al. 1984). There are several indirect, statistical methods utilized to associate galaxies and dark matter halos such as halo occupation distribution modeling (Peacock & Smith 2000; Benson et al. 2000; Berlind & Weinberg 2002; Bullock et al. 2002; Kravtsov et al. 2004), the conditional luminosity function (Yang et al. 2003), and the abundance matching technique (Vale & Ostriker 2004, 2006; Conroy et al. 2006; Guo et al. 2010; Moster et al. 2010, 2013; Behroozi et al. 2013). Abundance matching assumes that the cumulative number distributions of galaxies and halos are related in a monotonic manner; the most luminous galaxy is hosted by the most massive halo (within a given volume). At cluster scales ($M_\star > 10^{12} M_\odot$), X-ray mass measurements and virial scale tracers agree with abundance matching (e.g. Kravtsov et al. 2014). At lower masses and smaller scales there is a lack of virial tracers to make direct halo mass ($M_{\rm halo}$) measurements.

Other authors have suggested that rotation curves do not accurately trace the potential. Ignoring pressure support (generally accounted for with the application of the asymmetric drift correction) can bias the implied potential, especially for lower mass systems (Rhee et al. 2004; Dutton et al.

2005; Valenzuela et al. 2007). There are several other systematics that have been discussed in the literature, for example: non-circular motions (Swaters et al. 2003), beam-smearing from the finite beam width in HI observations (van den Bosch et al. 2000; Swaters et al. 2003), and axisymmetry issues (Hayashi et al. 2004). Rotation curve tests have been carried out by constructing realistic mock observations of hydrodynamic simulations (Rhee et al. 2004; Dutton et al. 2005; Valenzuela et al. 2007; Kuzio de Naray & Kaufmann 2011; Oh et al. 2011b; Pineda et al. 2016). Several works have recovered the input halos and their slopes (Kuzio de Naray & Kaufmann 2011; Oh et al. 2011b) while others have inferred small cores in a cuspy halo when ignoring pressure support (Pineda et al. 2016). While addressing the validity of rotation curve measurements and examining exotic dark matter models are fruitful endeavors in this work we address baryonic solutions.

Hydrodynamic simulations are required to test whether baryonic processes will alleviate small scale problems with the constraint that realistic galaxies are still formed (e.g. extremely efficient supernova feedback will remove dark matter and create a core but may destroy the galaxy in the process). There are several state-of-the-art hydrodynamic simulation projects (e.g. Stinson et al. 2013; Hopkins et al. 2014; Vogelsberger et al. 2014a; Schaye et al. 2015; Wang et al. 2015) that utilize different star formation and feedback prescriptions constructed with the aim to understand the formation and evolution of galaxies. Hydrodynamic simulations are able to produce galaxies with realistic disks that lie on the Tully-Fisher relationship (Robertson et al. 2004; Governato et al. 2007; Stinson et al. 2010; Piontek & Steinmetz 2011; Guedes et al. 2011; Christensen et al. 2012; Vogelsberger et al. 2014a; Sales et al. 2016). They can create both bulgeless and realistic bulges (Governato et al. 2010; Christensen et al. 2014; Snyder et al. 2015), match observed colors (Stinson et al. 2010; Sales et al. 2015), match the size-luminosity relation (Brooks et al. 2011), and reproduce the stellar-to-halo mass relationship (Guedes et al. 2011; Munshi et al. 2013; Hopkins et al. 2014; Di Cintio et al. 2014a; Wang et al. 2015). When stellar feedback is included, dark matter cores can be created (Governato et al. 2010; Macciò et al. 2012b; Governato et al. 2012; Teyssier et al. 2013; Di Cintio et al. 2014a; Oñorbe et al. 2015; Read et al. 2015; Chan et al. 2015; Tollet et al. 2016) but this is not ubiquitous as it depends on the particular feedback prescription as some

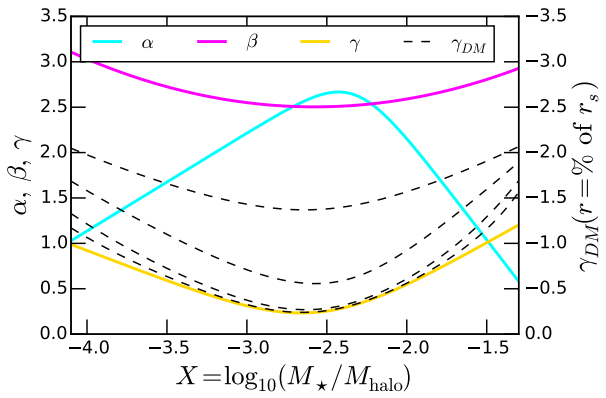

Figure 4.1: The dependence of the inner (γ, gold), outer (β, magenta), and transition (α, cyan) slope parameters on $X \equiv \log_{10}(M_\star/M_{\rm halo})$ for the DC14 profile (the values correspond to left y-axis; see Equation 4.2). The dashed black lines show log-slope dependence on X for the DC14 profile at different values of r/r_s (the values are shown on the right y-axis; see Equation 4.3). From bottom to top, the dashed lines correspond to $r/r_s = 0.1, 0.2, 0.5, 1.0$ respectively.

projects lack cores (Vogelsberger et al. 2014a; Schaye et al. 2015). Hydrodynamic simulations of Milky Way-sized halos or Local Group-like objects have been found to alleviate the TBTF problem (Zhu et al. 2016; Sawala et al. 2016; Wetzel et al. 2016).

Simulations have shown that they are able to create dark matter cores but do these simulated cored galaxies correspond to cores in observed galaxies? We address this by examining a (stellar) mass dependent halo profile. In Section 4.3, we introduce the halo profile, our rotation curve-fitting methodology, and the observational sample. In Section 4.4, we show that the observed rotation curves are well reproduced and compare the results to cosmological relationships. In Section 4.5, we discuss the potential systematics, the validity of the halo profile, and the implications of our findings.

4.3 The Halo Response due to Baryonic Processes

Di Cintio et al. (2014b, hereafter DC14) examined hydrodynamic simulations from the Making

Galaxies In a Cosmological Context (MAGICC) project (Stinson et al. 2013) to determine how the dark matter distribution responds to baryonic processes and galaxy formation. They determine the response by fitting $z \sim 0$ halos with an $\alpha\beta\gamma$ density profile (Jaffe 1983; Hernquist 1990; Merritt et al. 2006):

$$\rho(r) = \rho_s \, (r/r_s)^{-\gamma} \left[1 + (r/r_s)^{\alpha}\right]^{-(\beta-\gamma)/\alpha}, \tag{4.1}$$

and assuming α, β, and γ are functions of the integrated star formation efficiency (parameterized by $X \equiv \log_{10}(M_\star/M_{\rm halo})$). The functional forms with best fit values of α, β, and γ are (Equation 3 of DC14):

$$\begin{aligned}
\alpha(X) &= 2.94 - \log_{10}\left[\left(10^{X+2.33}\right)^{-1.08} + \left(10^{X+2.33}\right)^{2.29}\right] \\
\beta(X) &= 4.23 + 1.34X + 0.26X^2 \\
\gamma(X) &= -0.06 + \log_{10}\left[\left(10^{X+2.56}\right)^{-0.68} + \left(10^{X+2.56}\right)\right].
\end{aligned} \tag{4.2}$$

The X dependence shows the interplay between supernova feedback and adiabatic contraction. At high X values the halo profile steepens due to the large baryonic content, while intermediate values have the shallowest inner slope due to efficient feedback. At low X values the profile steepens again due to the inefficiency of star formation.

The log-slope of the α, β, γ profile is:

$$\gamma_{DM}(r) \equiv \left.\frac{{\rm d}\ln\rho}{{\rm d}\ln r'}\right|_{r'=r} = -\frac{\gamma + \beta\,(r/r_s)^{\alpha}}{1 + (r/r_s)^{\alpha}} = \gamma_{DM}(r; r_s, X), \tag{4.3}$$

where the last line follows for the DC14 profile. In Figure 4.1, we show α, β, and γ as a function of X. Overlaid are (dotted-black) lines showing the γ_{DM} dependence of a function of X for fixed values of $r/r_s = 0.1, 0.2, 0.5, 1.0$. The minimum slope occurs at $X \sim -2.7$.

We follow DC14 to define the halo concentration [1] as: $c_{\rm vir} \equiv r_{\rm vir}/r_{-2}$, where r_{-2} is $\gamma_{DM}(r = r_{-2}) \equiv -2$. DC14 show that $c_{\rm vir}$ is roughly equivalent between dark matter-only and hydrodynamic simulations if $X \lesssim -1.5$. Similarly, the EAGLE project finds the dark matter-only and hydrodynamic $c_{\rm vir}$ are consistent with one another (Schaller et al. 2015a).

The MAGICC simulations fall within the following ranges: $-4.1 < X < -1.3$, $2 \times 10^5 M_\odot < M_\star < 2.7 \times 10^{10} M_\odot$, and $9.4 \times 10^9 M_\odot < M_{\rm halo} < 7.2 \times 10^{11} M_\odot$ (For exploration of the halo response for larger halos see Dutton et al. 2015; Schaller et al. 2015b; Cui et al. 2016). This profile has one additional parameter when compared to standard halo profiles and it encapsulates non-trivial baryonic processes. The (stellar) mass-dependent halo profile ties together the inner properties (γ_{DM}) with the global properties ($M_{\rm halo}$). We exploit this to infer $M_{\rm halo}$ without tracers at the virial radius, $r_{\rm vir}$.

This profile has already been used to model rotation curves for several galaxies (Karukes et al. 2015; Repetto et al. 2015) but not with a large sample. It can potentially solve the TBTF problem in the Local Group (Brook & Di Cintio 2015a) and explain the Tully-Fisher relation (Brook & Di Cintio 2015b). When combined with scaling relations, it can potentially explain the scatter in rotation curve shapes (Brook 2015), and the mass discrepancy acceleration relation (Di Cintio & Lelli 2016). Papastergis & Shankar (2015) test abundance matching using the velocity measured at the outermost radii from the Arecibo legacy fast ALFA 21 cm survey. Even after accounting for baryonic effects with the DC14 profile they find abundance matching breaks down in the field at low rotation velocities ($V_{\rm max} \lesssim 25\,{\rm km\,s^{-1}}$). The DC14 profile was created with fits to hydrodynamic simulations and has been utilized in statistical studies. We aim to remedy a weaknesses of the previous analysis by testing this profile with a large observational sample of galactic rotation curves.

[1] This differs from the conventional definition but is identical for an NFW halo profile.

4.3.1 Determining $M_{\rm halo}$ and ρ_s

In order to facilitate present and future comparisons an explicit definition of $M_{\rm halo}$ is required. We follow DC14 with updates to the latest Planck cosmology. We define: $M_{\rm halo} = \frac{4\pi}{3}\Delta\rho_{\rm crit}r_{\rm vir}^3$, where $\Delta = 18\pi^2 + 82x - 39x^2 = 102.356$ ($x = \Omega_m - 1$) (Bryan & Norman 1998) and $\rho_{\rm crit} = 127.351\,{\rm M}_\odot\,{\rm kpc}^{-3}$ ($\Omega_m = 0.3089$, h $= 0.6774$; Planck Collaboration et al. 2015)[2].

To fully specify the halo profile, values of r_s, ρ_s, $M_{\rm halo}$, and $M_\star$ are required. $M_\star$ is defined as: $M_\star = L_x\Upsilon_{{\rm photo},x}\Upsilon_{\rm kinematic}$, where L_x corresponds to the luminosity in the photometric band x. L_x and $\Upsilon_{{\rm photo},x}$ are determined from the literature and $\Upsilon_{\rm kinematic}$ is treated as a free parameter.

The remaining parameters overdetermine the system; either ρ_s or $M_{\rm halo}$ can be eliminated. We treat $M_{\rm halo}$ as a free parameter and utilize the following prescription to determine ρ_s (which is a modified form of the DC14 Appendix):

- Determine r_s, $M_{\rm halo}$, and $M_\star$ (via $\Upsilon_{\rm kinematic}$) from points in parameter space
- Determine $r_{\rm vir}$ from $M_{\rm halo}$
- Evaluate $M(r_{\rm vir})$ via the density profile: $M(r_{\rm vir}) = 4\pi\rho_s\int_0^{r_{\rm vir}}(r/r_s)^{-\gamma}\left[1+(r/r_s)^\alpha\right]^{-(\beta-\gamma)/\alpha}r^2{\rm d}r$.
- Solve for ρ_s assuming $M(r_{\rm vir}) = M_{\rm halo}$.

Note that treating ρ_s as a free parameter is numerically impractical; as determining $M_{\rm halo}$ from r_s and ρ_s involves solving an integral-differential equation.

[2]For comparison, DC14 assumes a WMAP3 cosmology with $\Delta = 93.6$, $\rho_{\rm crit} = 147.896\,{\rm M}_\odot\,{\rm kpc}^{-3}$. We have verified that our results do not change between the WMAP3 and Planck cosmologies.

4.3.2 Priors and Parameter Estimation

The rotation curve includes contributions from the dark matter halo, gas disk, stellar disk, and potential stellar bulge:

$$V_{\rm tot}^2 = V_{\rm DM}^2 + V_{\rm Gas}^2 + \Upsilon_{\rm Disk} V_{\rm Disk}^2 \left(+ \Upsilon_{\rm Bulge} V_{\rm Bulge}^2 \right). \tag{4.4}$$

The baryonic components ($V_{\rm Gas}$, $V_{\rm Disk}$, $V_{\rm Bulge}$) are determined from the literature. We assume a factor of 1.4 when converting between the HI and gas surface densities to account for primordial Helium and other elements. $V_{\rm DM}$ is determined from the halo circular velocity: $V_{\rm DM}^2(r) = GM_{\rm DM}(r)/r$.

To explore the parameter space and compute the Bayesian evidence for model selection, we utilize the Multi-Nested Sampling routine (Feroz & Hobson 2008; Feroz et al. 2009). Our likelihood is:

$$-2\ln\mathscr{L} \propto \chi^2 = \sum_{i=1}^{N} \frac{\left[V_{i,\rm obs} - V_{\rm tot}(r_i)\right]^2}{\sigma_i^2}. \tag{4.5}$$

We compute the Bayes' Factor for model comparison tests[3]. We generally do not compare the reduced χ^2 as it only considers the best fit point and not the posterior distribution. The Bayes' Factor is the ratio of the Bayesian evidence for two models[4]: $\ln {\rm B}_{10} = \ln Z_1 - \ln Z_0$. For $\ln {\rm B}_{10} > 0$, model 1 is favored compared to model 0. The significance is interpreted via Jefferys' scale; the $\ln {\rm B}_{10}$ ranges of 0-1, 1-2.5, 2.5-5, and > 5 correspond to insignificant, mild, moderate, and significant evidence in favor of model 1 compared to model 0. The Bayes' Factor only considers comparisons of models and not overall goodness of fit.

Our prior distributions are:

- r_s: uniform in the range: $-1 < \log_{10}(r_s/{\rm kpc}) < 3$.

[3]See Trotta (2008) for a review of Bayesian model selection in astrophysics.

[4]We refer to the logarithm of the Bayes factor as the Bayes factor in this manuscript.

- $M_{\rm halo}$: uniform in the range: $5 < \log_{10}(M_{\rm halo}/M_{\odot}) < 14$.
- $\Upsilon_{\rm kinematic}$: uniform in the range: $0.5 < \Upsilon_{\rm kinematic} < 2$. The prior range is doubled for galaxies without $\Upsilon_{\rm photometric}$ inferred from stellar population synthesis analysis. For galaxies with a stellar bulge a second $\Upsilon_{\rm kinematic}$ is included.
- $M_{\star}$ and $M_{\rm halo}$ are kept within the range: $-4.1 < X < -1.3$.
- No cosmological priors are assumed between the halo parameters.

We assume the DC14 profile is valid throughout the entire $M_{\rm halo}$ range. We discuss enforcing the DC14 simulation limits in $M_{\star}$ and $M_{\rm halo}$ in Section 4.4.2. When available, $\Upsilon_{\rm photometric}$ values are set by stellar population synthesis models (Bell & de Jong 2001).

4.3.3 Observational Sample

Our sample includes rotation curves from the following sources: LITTLE THINGS (Hunter et al. 2012; Oh et al. 2015), THINGS (Walter et al. 2008; de Blok et al. 2008; Oh et al. 2008; Trachternach et al. 2008; Oh et al. 2011a), WHISP (Swaters et al. 2002; Swaters & Balcells 2002; Noordermeer et al. 2005; Swaters et al. 2009), the Ursa Major cluster (Tully et al. 1996; Tully & Verheijen 1997; Sanders & Verheijen 1998; Trentham et al. 2001; Verheijen & Sancisi 2001; Verheijen 2001; Bottema & Verheijen 2002; Bottema 2002), low surface brightness galaxies (van der Hulst et al. 1993; de Blok et al. 1996; McGaugh et al. 2001; de Blok & Bosma 2002; Swaters et al. 2003; Kuzio de Naray et al. 2006, 2008), and a miscellaneous sample (Begeman 1987; Carignan et al. 1988; Jobin & Carignan 1990; Lake et al. 1990; Côté et al. 1991; Gonzalez-Serrano & Valentijn 1991; Blais-Ouellette et al. 1999; van Zee & Bryant 1999; Weiner et al. 2001; Blais-Ouellette et al. 2001; Weldrake et al. 2003; Gentile et al. 2004, 2007, 2010; Elson et al. 2010; Kreckel et al. 2011; Frusciante et al. 2012; Lelli et al. 2012; Fraternali et al. 2011; Carignan et al. 2013; Elson et al. 2013; Corbelli et al. 2014; Lelli et al. 2014b; Kam et al. 2015; Richards et al. 2015; Randriamam-

Table 4.1: Galaxy sample and general properties. See Section 4.3.3 for explanation of columns. This table is available in its entirety in the online journal. The references are: a) Sorce et al. (2014); b) Jacobs et al. (2009); c) Dalcanton et al. (2009); d) Chemin et al. (2006); e) Puche et al. (1991a); f) Carignan & Puche (1990); g) Hlavacek-Larrondo et al. (2011b);

Galaxy	D	Method	Ref.	$\langle i \rangle$	$M_{\rm Disk}$ ($M_{\rm Bulge}$)	Sample	ADC	$M_\star$ Band	h_d/r_d	Υ	Q	RC Ref.
(1)	(2)	(3)	(4)	(5)	(6)	(7)	(8)	(9)	(10)	(11)	(12)	(13)
NGC 24	9.60	TF	a	64.0	9.47	Misc	N	I	0	Y	1	d
NGC 45	6.64	TRGB	b	41.0	9.40	Misc	N	B	0	Y	1	d
NGC 55	2.11	TRGB	c	77.0	9.67	Misc	N	B	0	N	2	e
NGC 247	3.54	TRGB	c	74.0	9.01	Misc	N	B	0	Y	1	f, g

pandry et al. 2015; Karachentsev et al. 2015; Bottema & Pestaña 2015; Carignan & Puche 1990; Puche et al. 1990, 1991a,b; Chemin et al. 2006; Hlavacek-Larrondo et al. 2011b,a; Westmeier et al. 2011, 2013; Lucero et al. 2015; Verdes-Montenegro et al. 1995). Galaxies with multiple rotation curve measurements are combined in non-overlapping regions and higher resolution data is used in overlapping regions[5].

We define the rotation curve quality tag, Q (varying between 1-3 with 1=best), to tag systems that may have misestimated errors or systematics that indicate an untrustworthy rotation curve. The quality decreases for galaxies containing the following: low kinematic inclination angles, $i < 35^{\circ}$, non-circular motions, disturbed velocity fields, asymmetries between the receding and ascending sides, or the presence of a star-burst phase. Q=1 systems contain none of these systematics, Q=2 systems contain 1-2 systematics, and Q=3 systems contain 3-4 systematics. In addition, the galaxies UGC 668 (IC 1613; Oh et al. 2015), UGC 4305 (DDO 50; Oh et al. 2015), and NGC 4736 (de Blok et al. 2008) are removed from the analysis.

The galaxy sample and properties are summarized in Table 4.1. The columns denote: (1) galaxy name; (2) distance in Mpc; (3) distance method; (4) distance reference; (5) average kinematic inclination angle, $\langle i \rangle$; (6) mass of the stellar disk in $M_{\odot}$ (and potential stellar bulge); (7) data source/survey; (8) asymmetric drift correction (ADC); (9) photometric band utilized for $M_{\star}$ measurements; (10) ratio of scale height to scale length; (11) stellar population synthesis model application for $\Upsilon_{\rm photometric}$; (12) rotation curve quality tag; (13) rotation curve citation. The distance methods are: Tully-Fisher (TF), tip of the red giant branch (TRGB), and Cepheid (Cep). The asymmetric drift correction options are: application (Y), not applied (N), and note required (NR). In the later case the effect was calculated and found to be sub-dominant. The ratio of scale height to scale length is denoted h_d/r_d and $h_d/r_d = 0$ denotes an infinitely-thin disk. Rotation curve sources listed in parenthesis are unused.

Different photometric bands and methods are utilized to determine $M_{\star}$ and $\Upsilon_{\rm photometric}$. For ex-

[5]Typically, optical Hα is used in the inner regions and radio HI measurements in the outer regions.

ample, THINGS and LITTLE THINGS utilize Spitzer Space telescope 3.6μm measurements and stellar population synthesis models to determine $M_\star$. The WHISP survey uses R-Band photometry and assumes $\Upsilon_{\rm photometric} = 1$ for each galaxy. For some galaxies, $\Upsilon_{\rm photometric}$ corresponds to the best fit value to the rotation curve (e.g. Côté et al. 2000; Gentile et al. 2004). In all cases we include a $\Upsilon_{\rm kinematic}$ as a free parameter.

4.4 Results

We apply the DC14 halo profile to our literature rotation curve sample and provide example fits in Figure 4.2. The sample galaxies were chosen from the Q=1 subset to highlight the variety of rotation curves in the sample and to show examples of both good and poor fits.

The majority of the sample is well explained using the DC14 halo profile. We quantify this by computing the reduced chi squared, χ^2_r, which indicates good fits for most of the sample; $\chi^2_r < 1$ for 76% out of 177 galaxies.

We conduct comparisons between the DC14 profile and the Pseudo-Isothermal sphere[6] (PISO; in terms of Equation 4.1, $\alpha = 2$, $\beta = 2$, $\gamma = 0$). The PISO profile is a commonly utilized 'cored' halo profile in rotation curve analysis and generally provides good fits to rotation curves. For our sample, the PISO profile provides a similar number of good fits with $\chi^2_{r,PISO} < 1$ (72%) and the median difference between the DC14 χ^2_r and PISO χ^2_r is $\langle \chi^2_{r,DC14} - \chi^2_{r,PISO} \rangle = 0.00^{+0.07}_{-0.09}$. We turn to the Bayes' Factor which considers the entire posterior distribution, the size of the prior distribution, and number of parameters. We the PISO profile we used a density scale, ρ_s, as a free parameter instead of $M_{\rm halo}$.

Comparisons with the Bayes' Factor are similar; roughly half the sample has an indeterminate

[6]We also conducted fits with the Navarro-Frenk-White (NFW; 1997; $\alpha = 1$, $\beta = 3$, $\gamma = 1$), and Burkert (1995) profiles. For most systems, the PISO provides better fits than the NFW and Burkert profiles, therefore we only conduct comparisons with the PISO profile in the main text. $\ln$B comparisons with the DC14 profile are listed in Table 4.2.

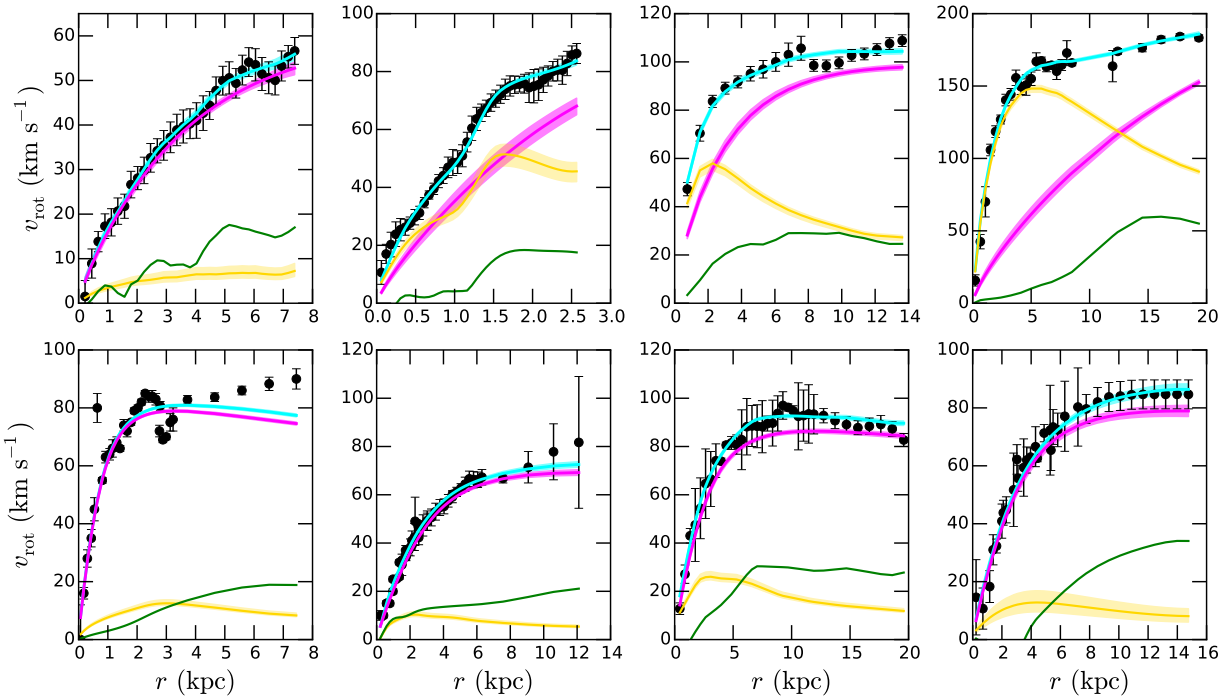

Figure 4.2: Examples of rotation curve fits with the DC14 (stellar) mass dependent halo profile. Galaxies are chosen from the $Q = 1$ sample (see Section 4.3.3) to highlight the variety in the sample and both good and poor fits. The observational data is shown as black points with error bars. The lines and shaded bands represent the following contributions: dark matter (magenta), stellar disk (gold), gas disk (green), and total fit (cyan). The shaded bands correspond to the 68% confidence interval (1-sigma region). From left to right the galaxies are, **top:** UGC 5918 (LITTLE THINGS; Oh et al. 2015), NGC 2976 (THINGS; de Blok et al. 2008), NGC 4288 (WHISP; Swaters et al. 2009), ESO 287-G15 (Gentile et al. 2004), **bottom:** UGC 2259 (Carignan et al. 1988; Blais-Ouellette et al. 2004), NGC 3109 (Jobin & Carignan 1990; Blais-Ouellette et al. 2001; Carignan et al. 2013), NGC 300 (Puche et al. 1990; Westmeier et al. 2011; Hlavacek-Larrondo et al. 2011b), and F583-01 (de Blok et al. 1996; McGaugh et al. 2001; Kuzio de Naray et al. 2006).

Table 4.2: Posteriors and model selection tests. $\ln \mathrm{B} > 0$ favors the DC14 model over the listed model. This table is available in its entirety in the online journal.

Galaxy	$\log_{10}(r_s/\mathrm{kpc})$	$\log_{10}(M_{\mathrm{halo}}/M_\odot)$	$\Upsilon_{\mathrm{kinematic}}$	$\log_{10}(X)$	$\gamma_{DM}(1\,\mathrm{kpc})$	$\gamma_{DM}(2\,\mathrm{kpc})$	$\ln \mathrm{B}_{\mathrm{PISO}}$	$\ln \mathrm{B}_{\mathrm{NFW}}$	$\ln \mathrm{B}_{\mathrm{Burkert}}$	$\chi^2_{r,DC14}$	$\chi^2_{r,PISO}$
NGC 24	$0.96^{+0.08}_{-0.09}$	$11.50^{+0.09}_{-0.08}$	$1.25^{+0.27}_{-0.28}$	$-1.94^{+0.04}_{-0.04}$	$-0.62^{+0.04}_{-0.04}$	$-0.69^{+0.05}_{-0.05}$	-0.47	0.27	-0.43	0.30	0.26
NGC 45	$0.67^{+0.02}_{-0.02}$	$11.17^{+0.01}_{-0.01}$	$0.72^{+0.09}_{-0.08}$	$-1.92^{+0.05}_{-0.05}$	$-0.71^{+0.05}_{-0.05}$	$-0.94^{+0.04}_{-0.04}$	39.90	-9.63	38.44	10.69	18.64
NGC 55	$0.97^{+0.16}_{-0.08}$	$11.29^{+0.21}_{-0.09}$	$0.38^{+0.17}_{-0.09}$	$-2.06^{+0.06}_{-0.07}$	$-0.52^{+0.05}_{-0.05}$	$-0.58^{+0.06}_{-0.06}$	1.18	1.14	6.31	0.22	0.35
NGC 247	$0.78^{+0.03}_{-0.05}$	$11.10^{+0.03}_{-0.04}$	$1.80^{+0.14}_{-0.22}$	$-1.84^{+0.03}_{-0.03}$	$-0.76^{+0.03}_{-0.03}$	$-0.92^{+0.04}_{-0.04}$	0.48	13.33	0.73	2.16	2.23

Bayes' Factor ($-1 < \ln \mathrm{B} < 1$, 52%). The reminder is divided between favoring the DC14 model ($\ln \mathrm{B} > 1$, 20%) and favoring the PISO model ($\ln \mathrm{B} < -1$, 29%), although several systems significantly favor the PISO profile ($\ln \mathrm{B} < -5$, 7%).

In Table 4.2, we tabulate the median posterior values for $\log_{10}(r_s/\mathrm{kpc})$, $\log_{10}(M_{\mathrm{halo}}/M_{\odot})$, $\Upsilon_{\mathrm{kinematic}}$, X, $\gamma_{DM}(1\mathrm{kpc})$, and $\gamma_{DM}(2\mathrm{kpc})$. Additionally included, are the Bayes' Factors and χ^2_r.

We reiterate that the X dependence links together γ_{DM} and M_{halo} for the DC14 halo profile. The physically motivated DC14 halo profile can explain rotation curve observations and is not disfavored compared to commonly utilized halo profiles.

4.4.1 Multimodal Posteriors

Measurements of the central region of a galaxies rotation curve implies a value for the inner slope. For most values of $\gamma_{DM}(r)$, there are two corresponding values of X for a fixed value of r_s (see Figure 4.1). This degeneracy is broken by measurements of the outer regions of the galaxy. Due to the variety of data quality this measurement is not available in all systems. Bi-modal M_{halo} posteriors are inferred in many systems and there are additional degeneracies with $\Upsilon_{\mathrm{kinematic}}$ and r_s.

As an example, we consider high resolution HI rotation curve of NGC 2976 from the THINGS survey (de Blok et al. 2008) where the flat component is not observed. In Figure 4.3, we examine the posterior and rotation curve fit. The upper panels display the posterior distributions of $\log_{10}(r_s/\mathrm{kpc})$, $\log_{10}(M_{\mathrm{halo}}/M_{\odot})$, X, and $\gamma_{DM}(r = 1\,\mathrm{kpc})$. The posterior is separated at $\log_{10}(M_{\mathrm{halo}}/M_{\odot}) = 11.75$. Each M_{halo} mode contains a corresponding mode in the r_s and X distributions, whereas the two modes have similar distributions for $\gamma_{DM}(r = 1\,\mathrm{kpc})$. In the lower panels, we show the rotation curve fits with the separated posterior (see Figure 4.2 for the full rotation curve). Remarkably, the total circular velocity from each M_{halo} mode is quite similar even though M_{halo} differs by an order

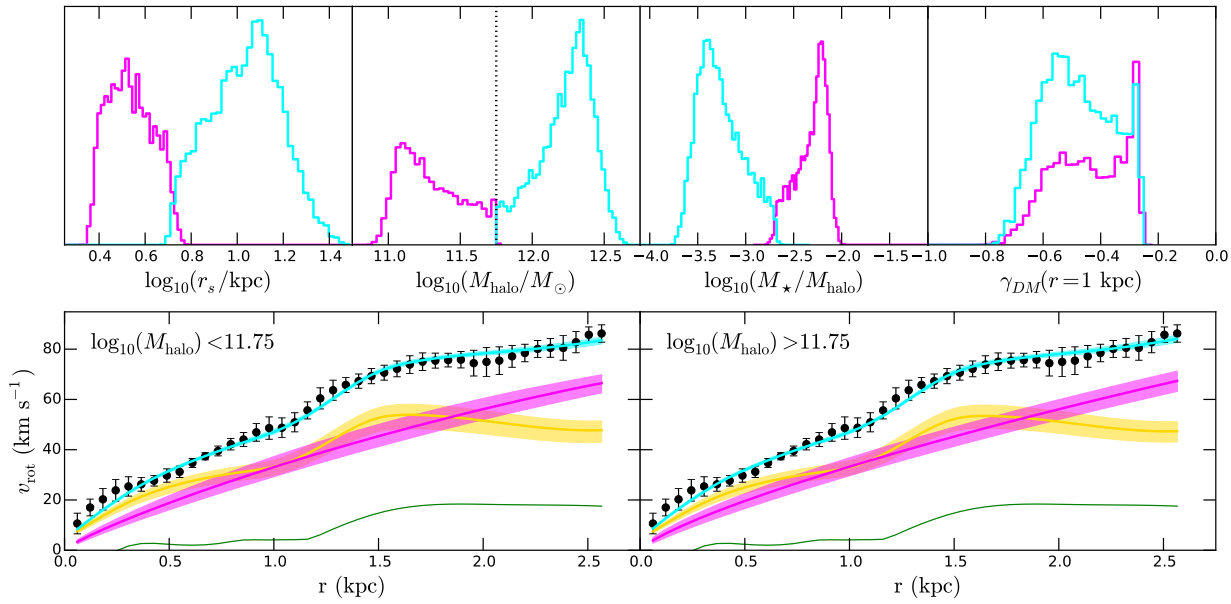

Figure 4.3: Example of a galaxy with a multimodal posterior (NGC 2976; de Blok et al. 2008). Without a well determined measurement of the flat component of the rotation curve the $M_{\rm halo}$ posterior is multimodal. **Top:** Posterior distribution split into the two $M_{\rm halo}$ modes. The posteriors from left to right are: $\log_{10}(r_s/{\rm kpc})$, $\log_{10}(M_{\rm halo}/M_\odot)$, $\log_{10}(M_\star/M_{\rm halo})$, and $\gamma_{DM}(r=1\,{\rm kpc})$. The two $M_{\rm halo}$ modes are separated by applying a cut at $\log_{10}(M_{\rm halo}/M_\odot)=11.75$. The smaller (magenta) and larger (cyan) modes contain 36% and 64% of the posterior respectively. **Bottom:** Rotation curve fits corresponding to the two $M_{\rm halo}$ modes. The left (right) panel shows the fit for $\log_{10}(M_{\rm halo}/M_\odot) < 11.75$ (> 11.75) (see Figure 4.2 for fit with the entire posterior). The shaded bands represent 68% confidence intervals for the subsets. The lines and colors follow Figure 4.2.

of magnitude.

We apply a similar analysis to all multimodal systems. The posterior is separated at the minimum $M_{\rm halo}$ value between the modes. In some galaxies, the separation is unclear. We denote these systems as poorly-separated and the former as well-separated.

4.4.2 Final Sample Selection

We consider the $M_{\rm halo}$ posteriors to construct a final sample to compare to cosmological relations. We remove single mode systems with $\sigma_{M_{\rm halo}} > 0.4\,({\rm dex})$ and refer to them as poorly-constrained systems. The remainder of the single mode posteriors are referred to as the well-constrained systems.

It is unclear whether the DC14 profile is valid outside of the simulation limits (e.g. at larger $M_{\rm halo}$ feedback from active galactic nuclei becomes important) and a suitable prior is required to enforce the simulation limits. An observationally motivated prior is to apply a cut at $V_{\rm obs,\,max} = 200\,{\rm km\,s^{-1}}$. This removes most but not all of the galaxies with large $M_{\rm halo}$ and even removes systems well within the DC14 limits. We therefore consider the $M_{\rm halo}$ and $M_\star$ posteriors for the cutoff; galaxies with median values of $M_\star$ and $M_{\rm halo}$ greater than a factor of two above the DC14 limits are excluded from the final sample. We assume the DC14 profile is valid for galaxies with $M_{\rm halo}$ smaller than the DC14 simulation limits (only 8 galaxies have median $M_{\rm halo}$ below the simulation limits).

Determining which mode to consider in multimodal systems will affect the interpretation of our results. We exclude all poorly-separated systems and consider the smaller mode of the well-separated posteriors (still considering the same cut in the median $M_\star$ and $M_{\rm halo}$ posteriors). In most cases the second (larger) $M_{\rm halo}$ mode is larger than the DC14 simulation limits and corresponds to an unrealistically large halo for the given galaxy (many of the larger modes have group or cluster $M_{\rm halo}$). The results from the first $M_{\rm halo}$ mode match the results for the well-constrained systems, providing

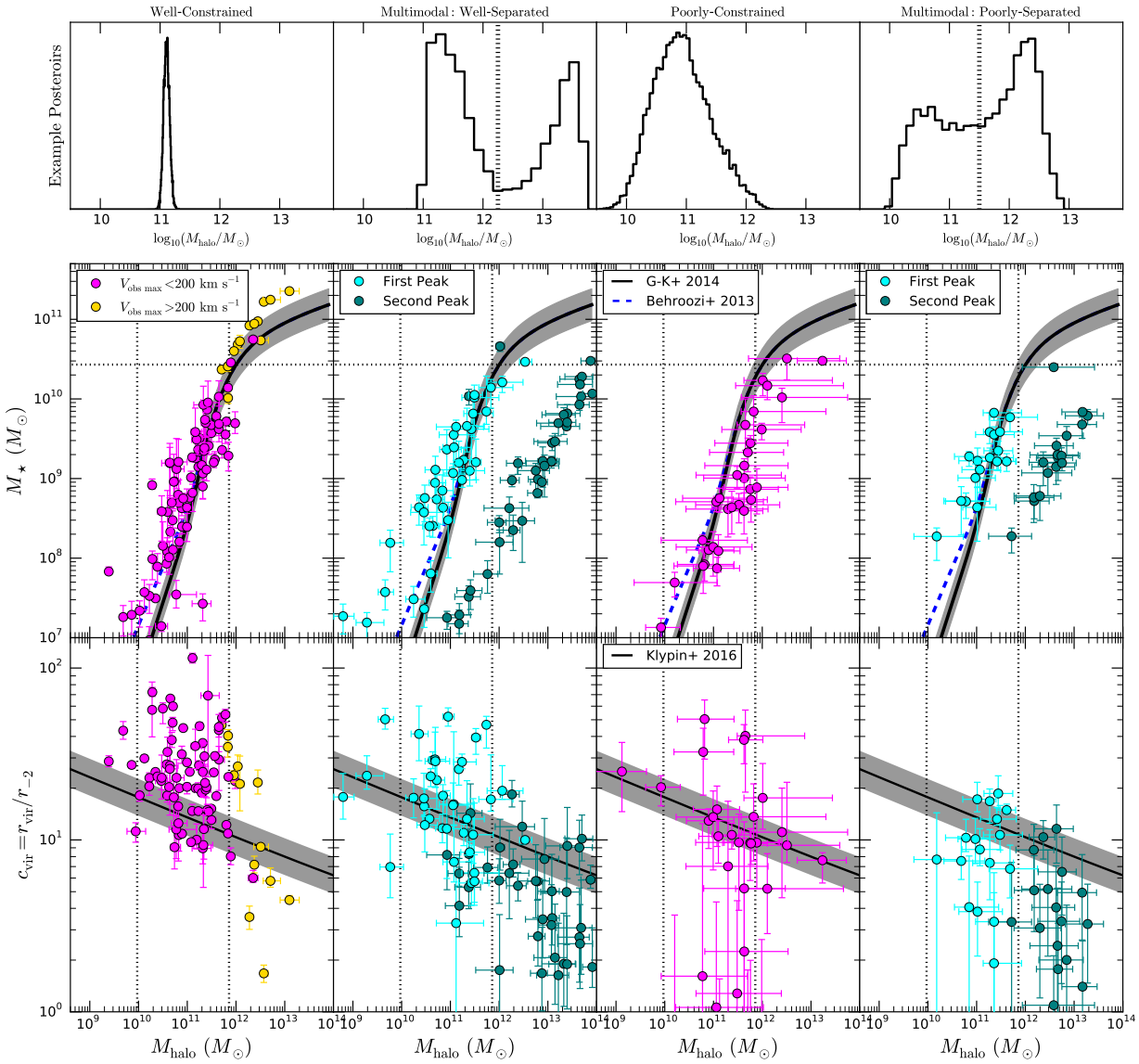

Figure 4.4: Visualization of the sample for $M_{\rm halo}$ versus $M_\star$ and $c_{\rm vir}$ (See Figure 4.5 for the results with the final sample). The sample is split based on the distribution and number of modes in the $M_{\rm halo}$ posterior. The columns show the different divisions based on $M_{\rm halo}$; from **left to right** the divisions are: single mode well-constrained, multimodal well-separated, single mode poorly-constrained, and multimodal poorly-separated. **Top:** example $M_{\rm halo}$ posteriors from each division. **Middle:** $M_{\rm halo}$ versus $M_\star$. In the left-hand column, systems with $V_{\rm obs,\,max} > 200\,{\rm km\,s^{-1}}$ are shown as gold circles. For multimodal systems, each mode is shown with different colored points. The error bars correspond to 68% confidence intervals within that mode. Overlaid are abundance matching relationships Behroozi et al. (2013); Garrison-Kimmel et al. (2014a) in blue and black respectively. Dotted black lines show the DC14 simulation limits. **Bottom:** $M_{\rm halo}$ versus $c_{\rm vir}$. Overlaid is the $c_{\rm vir} - M_{\rm halo}$ relationship from the Multidark simulations (Klypin et al. 2016). The final sample consists of the well-constrained (left-hand panel) and the first mode of the well-separated systems (cyan points in the second panel from the left) with median $M_{\rm halo}$ and $M_\star$ values less than a factor of two from the upper limits of the DC14 simulations.

circumstantial evidence that the larger $M_{\rm halo}$ mode is unrealistic. The final sample contains 119 galaxies after the application of these cuts.

We show the four $M_{\rm halo}$ subsets visually in Figure 4.4. The columns show (from left to right): well-constrained, well-separated, poorly-constrained, and poorly-separated systems. The top row shows an example posterior from each category. The middle and bottom rows show $M_\star - M_{\rm halo}$ and $c_{\rm vir} - M_{\rm halo}$ respectively. In the well-constrained column, we show the systems with $V_{\rm obs,\,max} > 200\,{\rm km\,s^{-1}}$ as gold points; displaying the issue with a $V_{\rm obs,\,max}$ cut. Overlaid are $M_\star - M_{\rm halo}$ abundance matching relations (Behroozi et al. 2013; Garrison-Kimmel et al. 2014a) and $c_{\rm vir} - M_{\rm halo}$ relations from the MultiDark simulations (Klypin et al. 2016). The multimodal systems separate in both the $M_\star - M_{\rm halo}$ and $c_{\rm vir} - M_{\rm halo}$ space. The final sample consists of the well-constrained galaxies (left-hand column) and the first mode of the well-separated multimodal systems (cyans points; second column from the left).

4.4.3 Cosmological Relations

In Figure 4.5 we show the derived cosmological relations from the final sample compared to results from the literature. The top panel shows the $M_\star - M_{\rm halo}$ relationship overlaid with the relationship derived from abundance matching (Behroozi et al. 2013; Garrison-Kimmel et al. 2014a). The galaxies are colored according to their quality tag and the symbols denote multimodal systems.

We focus our abundance matching comparison to two recent works focusing on different mass regimes (Behroozi et al. 2013; Garrison-Kimmel et al. 2014a). The first, Behroozi et al. (2013), is constructed with large volume observations of the stellar mass function, cosmic star formation rate, and specific star formation rate and is complete to $M_\star \sim 10^{8.5}\,M_\odot$ ($M_{\rm halo} \sim 10^{10.9}\,M_\odot$). The later (Garrison-Kimmel et al. 2014a), use the local group (defined as galaxies within ~ 1.2 Mpc) stellar mass function to push the completeness to $M_\star \sim 10^5 M_\odot$. They tie their relation to Behroozi et al. (2013) at large masses and find a steeper faint end slope (see also Brook et al. 2014; Garrison-

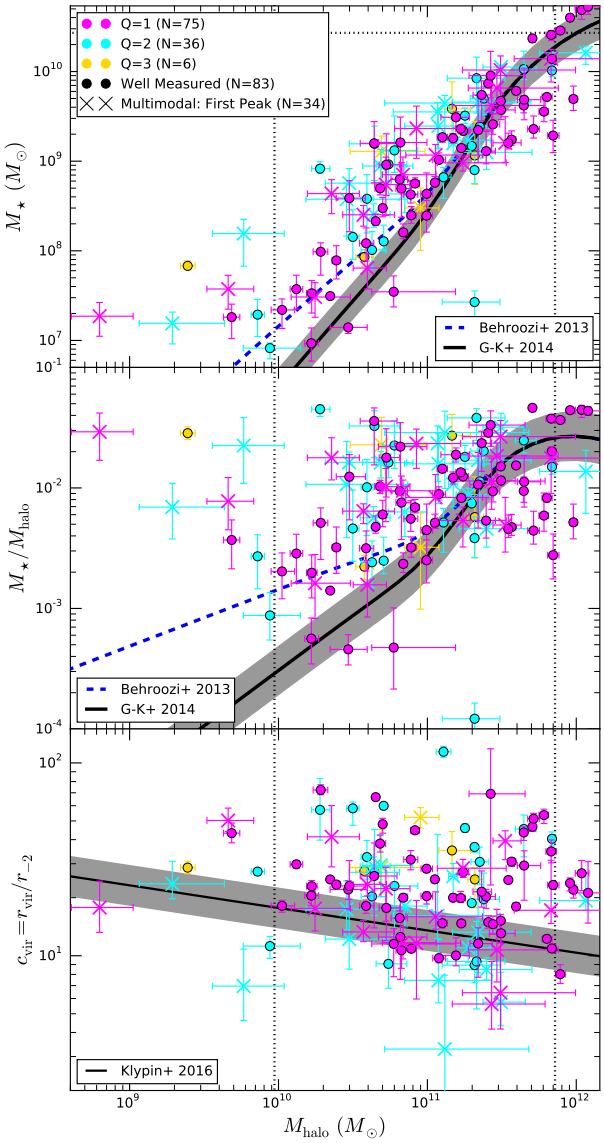

Figure 4.5: Cosmological relations inferred from galactic rotation curve fits with the DC14 profile (see Section 4.4.2 for an explanation of our sample selection). We denote potential systematics with the quality tag and separate them by color (see Section 4.3.3; Q=1 denotes trustworthy rotation curves). The symbols denote whether the $M_{\rm halo}$ posterior is multimodal. For multimodal systems we consider the first mode and errorbars denote 68% confidence intervals within the first mode's posterior (See Figure 4.3, Section 4.4.1). **Top:** $M_\star$ vs $M_{\rm halo}$. Overlaid are $M_\star - M_{\rm halo}$ relations derived from the abundance matching technique (Behroozi et al. 2013; Garrison-Kimmel et al. 2014a, are shown as blue-dashed and black-solid lines respectively). We assume 0.2 dex of spread in the $M_\star - M_{\rm halo}$ relations (Behroozi et al. 2013; Reddick et al. 2013). The dotted lines show the range of simulations in DC14. **Middle:** $M_\star/M_{\rm halo}$ versus $M_{\rm halo}$. The differences between abundance matching and the inferred halos are emphasized in this space. **Bottom:** $c_{\rm vir}$ versus $M_{\rm halo}$. The black solid lines show the expected $c_{\rm vir} - M_{\rm halo}$ relationship from the MultiDark simulations (Klypin et al. 2016).

Kimmel et al. 2016). We assume a spread of 0.2 dex (Behroozi et al. 2013; Reddick et al. 2013) in the $M_\star - M_{\rm halo}$ relation and display this relative to the Garrison-Kimmel et al. (2014a) relationship. For $M_\star > 10^9 M_\odot$, we observe scatter relative to the abundance matching relationships. Below this, the galaxies preferentially lie in smaller halos than expected from abundance matching. Our results strongly disagree with the local group stellar mass function.

The middle panel displays $X = M_\star / M_{\rm halo}$ versus $M_{\rm halo}$. Many of the systems with low $M_{\rm halo}$ have significantly larger $M_\star$ than expected. For a given $M_\star$, many galaxies are hosted by significantly smaller halos than expected. Galaxies produced in hydrodynamic simulations (including the MAGICC project) are found to match the $M_\star - M_{\rm halo}$ relationships within the regime of masses we are considering (Munshi et al. 2013; Hopkins et al. 2014; Di Cintio et al. 2014a; Wang et al. 2015). The $M_\star - M_{\rm halo}$ relationship from Behroozi et al. (2013); Garrison-Kimmel et al. (2014a) combined with the DC14 profile predicts a dark matter inner slope. This prediction is at odds with the dark matter cores and inner slopes inferred from rotation curve observations. At a given $M_{\rm halo}$, the dark matter inner slopes in the DC14 simulations do not correspond to the dark matter inner slopes in galaxy observations.

In the lower panel, we display $c_{\rm vir}$ versus $M_{\rm halo}$. Overlaid is the $c_{\rm vir} - M_{\rm halo}$ relationship from the MultiDark simulations (Klypin et al. 2016). We observe much higher $c_{\rm vir}$ than cosmological simulations. $c_{\rm vir}$ is not expected to change between hydrodynamic and dark matter-only simulations (DC14; Schaller et al. 2015a). We do not expect the baryon response to affect the $c_{\rm vir} - M_{\rm halo}$ relation. The observed $c_{\rm vir} - M_{\rm halo}$ relation contains significantly larger scatter than the relationship found in dark matter-only simulations.

Although we can explain rotation curve observations, we do not recover the $M_\star - M_{\rm halo}$ and $c_{\rm vir} - M_{\rm halo}$ cosmological relationships. In Appendix 4.6.2, we compare the deviations between the $M_\star - M_{\rm halo}$ and $c_{\rm vir} - M_{\rm halo}$ relationship. We uncover no trends in the deviations. Based on the above discussion, these relationships are not expected to differ when changing from dark matter-only to hydrodynamic simulations.

4.5 Discussion

4.5.1 Stellar Mass and other Systematics

A data sample from the literature is heterogeneous and systematic biases may be introduced. We address potential systematics by dividing the sample based on the application of different methods in interpreting the rotation curve. The first is through the quality tag; galaxies with indications that the rotation curve may not trace the underlying potential are denoted with a higher tag (see Section 4.3.3). At low inclination angles ($i < 35^{\circ}$) small changes to the inclination will result in large differences in the measured circular velocity. A galaxy in a starburst or post-starburst phase will contain gas out of equilibrium resulting in rotation curves that may not match the true circular velocity (Lelli et al. 2014b; Read et al. 2016). Disturbed velocity fields, lopsided gas distributions, and asymmetries between the receding and ascending sides may be signs of recent star formation indicating additional uncertainties unaccounted for in the standard measurement errors (Lelli et al. 2014a). We separate the sub-samples by color in Figure 4.5. Our results are robust to the removal of higher Q systems (see Figure 4.7). Furthermore, we find that our results are robust to pressure support, uncertainties in $M_{\star}$, and the combination of different surveys and data sources, as we discuss below in detail.

Pressure support in low mass systems ($V_{\rm obs,\,max} < 75\ {\rm km\,s^{-1}}$) may lead to incorrect inferences of the circular velocity; the asymmetric drift correction is commonly used to correct for pressure support (Dalcanton & Stilp 2010). Roughly half of the sample either has the asymmetric drift correction applied (21%) or pressure support has been determined and is to small to affect the rotation curve (26%) (e.g. Weldrake et al. 2003; Swaters et al. 2009; Karachentsev et al. 2015). For low mass systems ($V_{\rm obs,\,max} < 75\ {\rm km\,s^{-1}}$), 49% of the systems have the asymmetric drift correction and for 33% of the systems it is not required.

Incorrect measurements of $M_{\star}$ will change the implied effect baryons have to the halo. To address

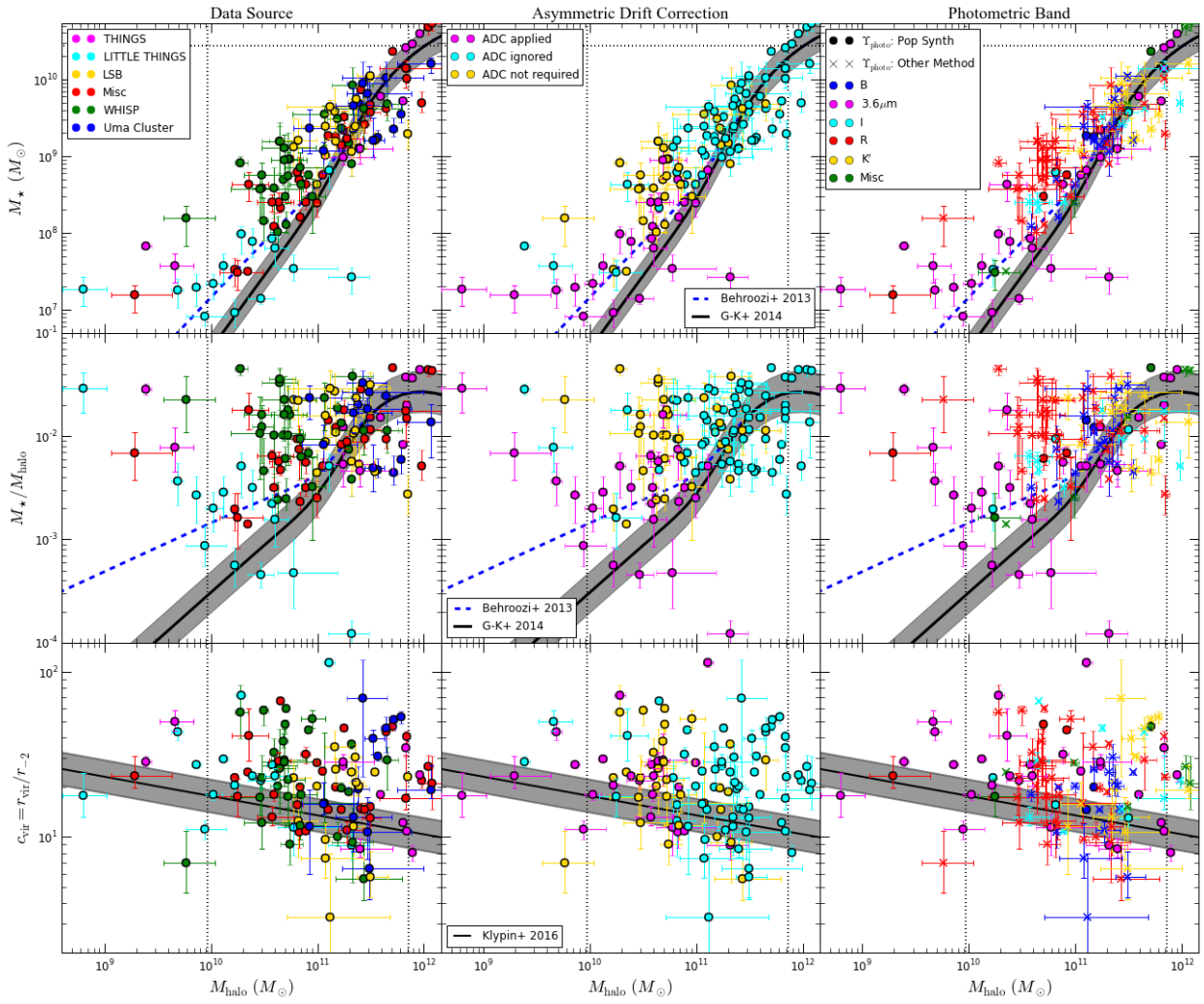

Figure 4.6: $M_\star - M_{\rm halo}$, $M_\star/M_{\rm halo} - M_{\rm halo}$, and $c_{\rm vir} - M_{\rm halo}$ relations for subsets of the sample (See Figure 4.5). The subsets are: data source (left-hand column), asymmetric drift application (middle column), and $M_\star$ photometric band (right-hand column). The data sources are (color and citation): THINGS (magenta; de Blok et al. 2008; Oh et al. 2011a), LITTLE THINGS (cyan; Oh et al. 2015), low surface brightness galaxies (LSB; gold; see Section 4.3.3 for citations), miscellaneous (Misc; red; see Section 4.3.3 for citations), WHISP (green; Swaters et al. 2009), and Ursa Major cluster (Uma; blue; Sanders & Verheijen 1998; Verheijen & Sancisi 2001). The the asymmetric drift correction (ADC) subsets are: application (magenta), disregarded (cyan), and calculated but too small to affect the results (gold). The photometric bands are: B (blue), Spizter space telescope 3.6μm (magenta), I (cyan), R (red), K$'$ (gold), and Misc/other (green). Galaxies with (without) $\Upsilon_{\rm photometric}$ values calculated from stellar population synthesis models are shown as circles (x's). The overlaid relationships follow Figure 4.5.

this we first update the distance[7] (and therefore luminosity) based on more precise measurements from the Tully-Fisher relation (Tully et al. 2008; Sorce et al. 2014), the tip of the red-giant branch (Jacobs et al. 2009; Dalcanton et al. 2009), or Cepheid variable star measurements.

Infrared photometry traces the old stellar population and is less affected by intergalactic dust (Walter et al. 2007). Ideally, Spitzer 3.6μm would be utilized (e.g. de Blok et al. 2008; Oh et al. 2015), but it is not available for all galaxies. We separate the sample by the photometric band utilized to derive the stellar surface density and stellar luminosity. This subdivision is similar to a separation on data source but the miscellaneous portion contains a wide variety of photometric bands. The primary bands utilized are: Spitzer 3.6μm (24%), B (15%), I (10 %), K$'$ (12%), and R (32%). When available, $\Upsilon_{\rm photometric}$ is pinned to stellar population synthesis models (34% of our sample).

The priors on $\Upsilon_{\rm kinematic}$ varied by a factor of 2 or 4 depending on whether $\Upsilon_{\rm photometric}$ was determined by stellar population synthesis models. We explore using a much wider (and unrealistic) prior range, $0.05 < \Upsilon_{\rm kinematic} < 10.0$. Our general results are robust to the larger prior but the results for individual galaxies are not. In some systems the posterior in $M_{\rm halo}$ becomes multimodal or significantly increases in size due to degeneracies with $\Upsilon_{\rm kinematic}$. We reconstruct Figures 4.4 and 4.5 with the results from the larger prior range in Appendix 4.6.3.

The sample contains stellar disk rotation curves constructed with both the thin disk approximation and a non-zero scale height. The common ratios of scale height-to-scale length (h_d/r_d) are: $h_d/r_d = 0, 1/5, 1/6$. An assumption of $h_d = r_d/5$ is valid for many disk-dominated galaxies (van der Kruit & Searle 1981; Kregel et al. 2002). This difference has a small effect but changes in the baryonic circular velocity will be reflected in the inferred dark matter halo. Most of the sample contains a non-zero scale height (74%) while the reminder assumes a thin disk.

Our results are robust to: pressure support (asymmetric drift correction), uncertainties in Υ, the photometric band utilized for the $M_\star$ measurement, the stellar disk circular velocity calculation, and

[7]The distances for the THINGS and LITTLE THINGS surveys are not changed.

the combination of different surveys. In Figure 4.6, we reconstruct Figure 4.5 with the sample split by the data source (left-hand column), asymmetric drift correction application (middle cloumn), and photometric band utilized for $M_\star$ measurements (right-hand column). Each subset has large scatter compared to the $M_\star - M_{\rm halo}$ and $c_{\rm vir} - M_{\rm halo}$ relations. None of the subsets have significant offsets from the main sample; our results are not driven by a particular data source or photometric band. It is unlikely that observational systematics account for our results.

There are several improvements that can be made to this work. Measurements of $M_\star$ and the stellar surface density in a single consistent photomteric band, ideally infrared photometry, would decrease uncertainties in $M_\star$ measurements and the systematics in combining different data sources. There are several methods for rotation curve construction that our sample contains (e.g. Sancisi & Allen 1979; Begeman 1987; van der Hulst et al. 1992; de Blok & McGaugh 1997; Gentile et al. 2004; Spekkens & Sellwood 2007; Oh et al. 2008, 2011a; Di Teodoro & Fraternali 2015). Construction of the rotation curve from the data cubes in a uniform manner would similarly reduce systematics. Application of the asymmetric drift correction for all galaxies, especially for systems with $V_{\rm obs,\,max} < 75\,{\rm km\,s^{-1}}$, would reduce the uncertainties from pressure support (Dalcanton & Stilp 2010).

4.5.2 Baryonic Halo Profiles

The (stellar) mass-dependent profile of DC14 is thus far the only work that has characterized the response of the *entire* halo profile due to baryonic processes. It is well established that hydrodynamic simulations with stellar feedback can create dark matter cores and the focus has been on determining the size of the dark matter core or how the dark matter inner slope scales (Governato et al. 2010; Macciò et al. 2012b; Governato et al. 2012; Teyssier et al. 2013; Di Cintio et al. 2014a; Oñorbe et al. 2015; Read et al. 2015; Chan et al. 2015; Tollet et al. 2016). For example, Governato et al. (2012) quantified the halo response of the dark matter inner slope to be:

$\rho_{DM} \propto r^{\alpha}$; $\alpha = -0.5 + 0.35 \times \log 10\big(M_{\star}/10^{8} M_{\odot}\big)$.

Recent work has focused on the dependence of the inner slope with X (Chan et al. 2015; Tollet et al. 2016). The NIHAO suite (~ 70 simulations) contains an updated star formation and feedback prescription from the MAGICC simulations and finds a dependence that agrees with the DC14 profile (Tollet et al. 2016). The FIRE project (9 simulations) uses an independent star formation and feedback prescription with a pressure-independent smoothed particle hydrodynamics code (Hopkins et al. 2014) and finds the inner slope to have a different X dependence (See Figure 4 of Chan et al. 2015). The location of the minimum inner slope is the same in both works but Chan et al. (2015) has a steeper slope at small X and shallower slope at large X compared to Tollet et al. (2016). In both cases, observed galaxies with dark matter cores will be driven to $X \sim -2.7$ regardless of $M_{\rm halo}$ or $V_{\rm obs,\,max}$ if the halo profile is of this form. With such a small sample it is unclear how significant the discrepancy is and further work is required.

We define the core radius as[8]: $r_c = r_{-1}$, then $r_c = r_s \left(\frac{1-\gamma}{\beta-1}\right)^{1/\alpha}$. With this definition, we find the maximum r_c at $X \sim -2.7$ for fixed r_s. For low mass galaxies that favor large cores, $M_{\rm halo}$ will be driven towards $X \sim -2.7$ which increases $c_{\rm vir}$ for fixed r_s. This drives the galaxies away from cosmological relations.

The core radii correlates with the stellar radial scale in hydrodynamic simulations with stellar and supernova feedback, imprinting an additional radial scale in the halo (Oñorbe et al. 2015; Read et al. 2015). To fully capture the halo response a density profile with a second radial scale may be required (Read et al. 2015). Observations find that the stellar disk size scales with $M_{\star}$ ($r_d \propto M_{\star}^{\alpha}$; e.g. Hunter & Elmegreen 2006; Courteau et al. 2007; Fathi et al. 2010), implying the X dependence in the DC14 profile may already include the dependence of the stellar radial scale. Exploring different functional forms may be a fruitful endeavor. It is possible that the MAGICC simulations have not fully captured the halo response and a refined (stellar) mass-dependent profile

[8]The core radius is commonly defined from the logarithmic slope or density. The density definition of r_c is: $\rho(r_c)/\rho(0) \equiv 1/2$. We favor the slope definition since the density is not finite at r=0. For the PISO profile the two definitions are equivalent and they agree to within 20% for the Burkert profile.

can alleviate the tension observed between the rotation curve fits and cosmological relationships. Current results from hydrodynamic simulations do not suggest strong deviations from the DC14 profile.

The breakdown of the cosmological scaling relations is indicative of the failure to solve the TBTF and diversity problems. The observed inner slopes can be explained with baryonic physics but will not simultaneously match cosmological relationships. Standard cosmological relationships breaking down at low $M_{\rm halo}$ may be pointing towards unaccounted effects and additional physics in the dark sector may help reconcile the tension. For example, warm (Lovell et al. 2014), self-interacting (Rocha et al. 2013; Kaplinghat et al. 2014), or scalar field (Robles & Matos 2013; Schive et al. 2014) dark matter can imprint another radial scale in the dark matter halo without affecting large-scale structure.

We have conducted tests of the (stellar) mass dependent halo profile from DC14 with rotation curves from the literature. The (stellar) mass dependent profile can explain rotation curve observations (i.e. solve the 'core-cusp' problem) but will not simultaneously reproduce the cosmological $M_\star - M_{\rm halo}$ or $c_{\rm vir} - M_{\rm halo}$ relationships. Directly modeling rotation curves with halo profiles set by hydrodynamic simulations is a fruitful method to test the dark matter response to baryonic processes in hydrodynamic simulations.

Acknowledgements

We thank Manoj Kaplinghat for helpful discussions and comments on the manuscript. We thank James Bullock, Sheldon Campbell, Sean Tulin, and Hai-bo Yu for helpful discussions. ABP is supported by a GAANN fellowship. We thank the following for kindly sharing rotation curve data: Erwin de Blok, Roelof Bottema, Jayaram Chengalur, Stéphanie Côté, Edward Elson, Noemi Frusciante, Gianfranco Gentile, Igor Karachentsev, Kathryn Kreckel, Federico Lelli, Stacy McGaugh,

Se-Heon Oh, Toky Randriamampandry, Emily Richards, Rob Swatters, and Ben Weiner.

Databases and software: This research has made use of the NASA/IPAC Extragalactic Database (NED) which is operated by the Jet Propulsion Laboratory, California Institute of Technology, under contract with the National Aeronautics and Space Administration and the HyperLeda database[9] (Makarov et al. 2014). Python packages: `Astropy`[10] (Astropy Collaboration et al. 2013), `NumPy` (Walt et al. 2011), `iPython` (Pérez & Granger 2007), `SciPy` (Jones et al. 2001), and `matplotlib` (Hunter 2007).

4.6 Appendix

4.6.1 High Quality Rotation Curves

In this section we consider the final sample with only the Q=1 subset. We reproduce Figure 4.5 with this subset in Figure 4.7. Our main results are robust to including the Q=2,3 subsets.

4.6.2 Deviation from Cosmological Relationships

We explore the deviations from the Behroozi et al. (2013) $M_\star - M_{\rm halo}$ and Klypin et al. (2016) $c_{\rm vir} - M_{\rm halo}$ relationships in this section. In Figure 4.8, we show the deviation from the $M_\star - M_{\rm halo}$ versus deviation from the $c_{\rm vir} - M_{\rm halo}$ relationship. Each deviation is expressed as the ratio of the measured quantity to the expected quantity at a fixed measurement. The $c_{\rm vir}$ deviation is quantified by the ratio of the measured $c_{\rm vir}$ to the expected $c_{\rm vir}$ at the measured $M_{\rm halo}$ value. We quantify the deviation from the $M_\star - M_{\rm halo}$ relationship two ways. First (left panel in Figure 4.8), we compute the ratio of the measured $M_\star$ versus the expected $M_\star$ at the measured $M_{\rm halo}$ value. Second

[9] `http://leda.univ-lyon1.fr`
[10] `http://www.astropy.org`

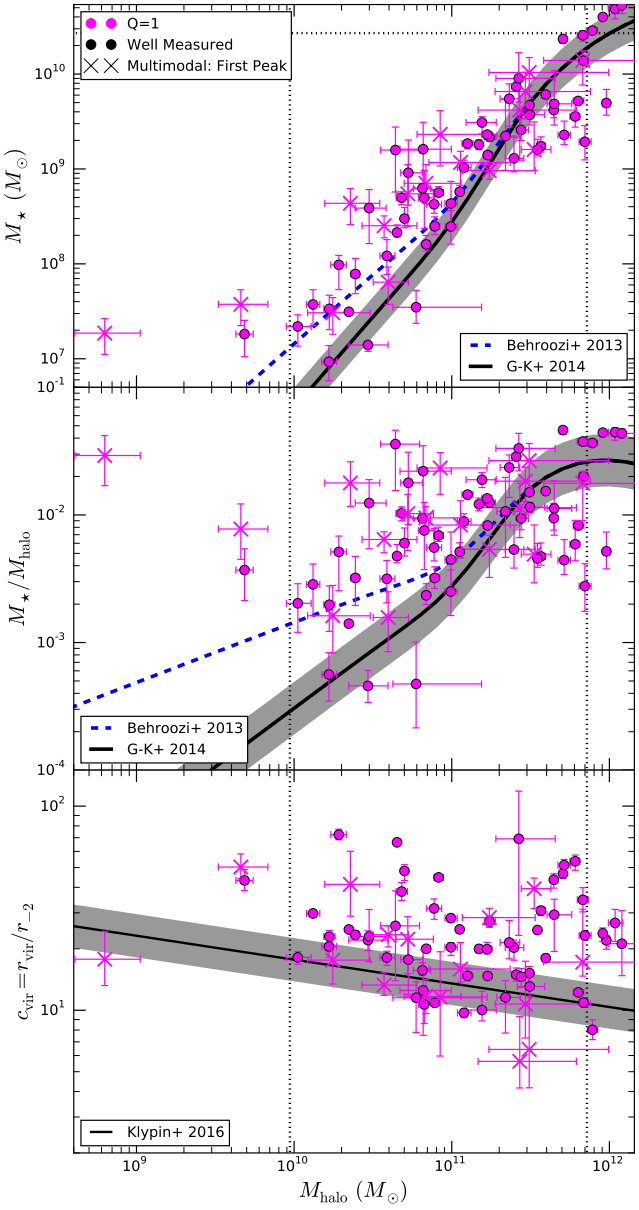

Figure 4.7: Same as Figure 4.5 with only Q=1 subset.

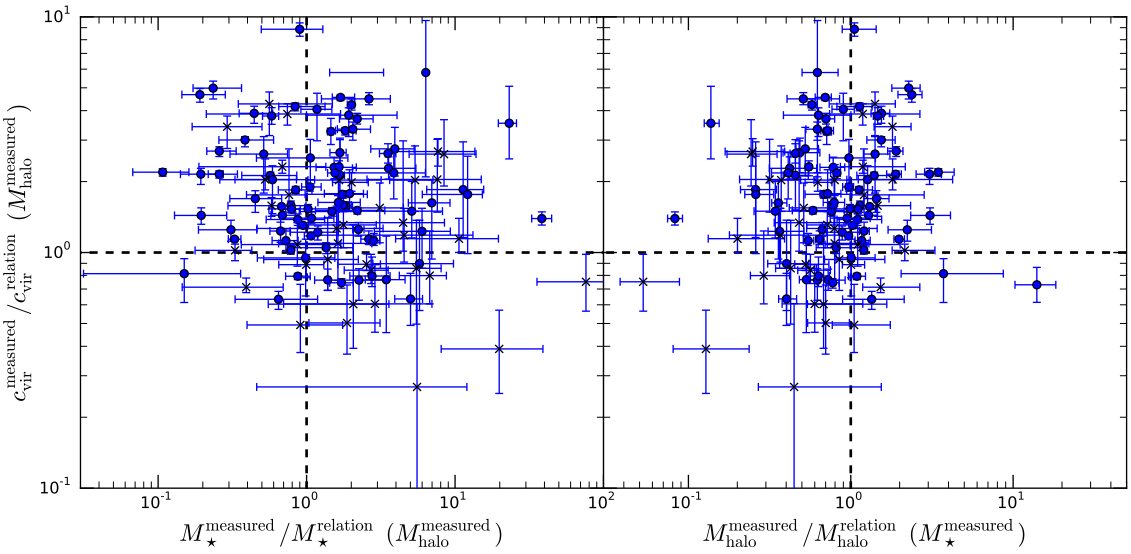

Figure 4.8: Ratio of the deviation from the Behroozi et al. (2013) $M_\star - M_{\rm halo}$ relationship versus the deviation from the Klypin et al. (2016) $c_{\rm vir} - M_{\rm halo}$ relationship. The deviation from $M_\star - M_{\rm halo}$ relation is computed by comparing the ratio of the measured $M_\star$ to the expected $M_\star$ at the measured $M_{\rm halo}$ (left panel) or comparing the ratio of the measured $M_{\rm halo}$ to the expected $M_{\rm halo}$ for the measured $M_\star$ (right panel). The deviation from $c_{\rm vir} - M_{\rm halo}$ relation is computed by comparing the ratio of the measured $c_{\rm vir}$ to the expected $c_{\rm vir}$ at the measured $M_{\rm halo}$. Multimodal systems are shown as x's while single-mode systems are circles. Dashed lines show where the measured value is equal to the relation.

(right panel in Figure 4.8), we compute the ratio of the measured $M_{\rm halo}$ versus the expected $M_{\rm halo}$ at the measured $M_\star$ value. In both cases, no trends between the deviations in the cosmological relationships are observed.

4.6.3 Larger Kinematic Υ

We explore a larger prior range in $\Upsilon_{\rm kinematic}$ is this section. The prior range is increased to $0.05 < \Upsilon_{\rm kinematic} < 10.0$. We reproduce Figures 4.4 and 4.5 with the larger prior range in Figures 4.9 and 4.10 respectively. Our main results are robust to the increased prior range but the results for individual galaxies are not. There are more systems with multimodal $M_{\rm halo}$ posteriors and several systems have three distinct modes in the $M_{\rm halo}$ posterior. We include an additonal column

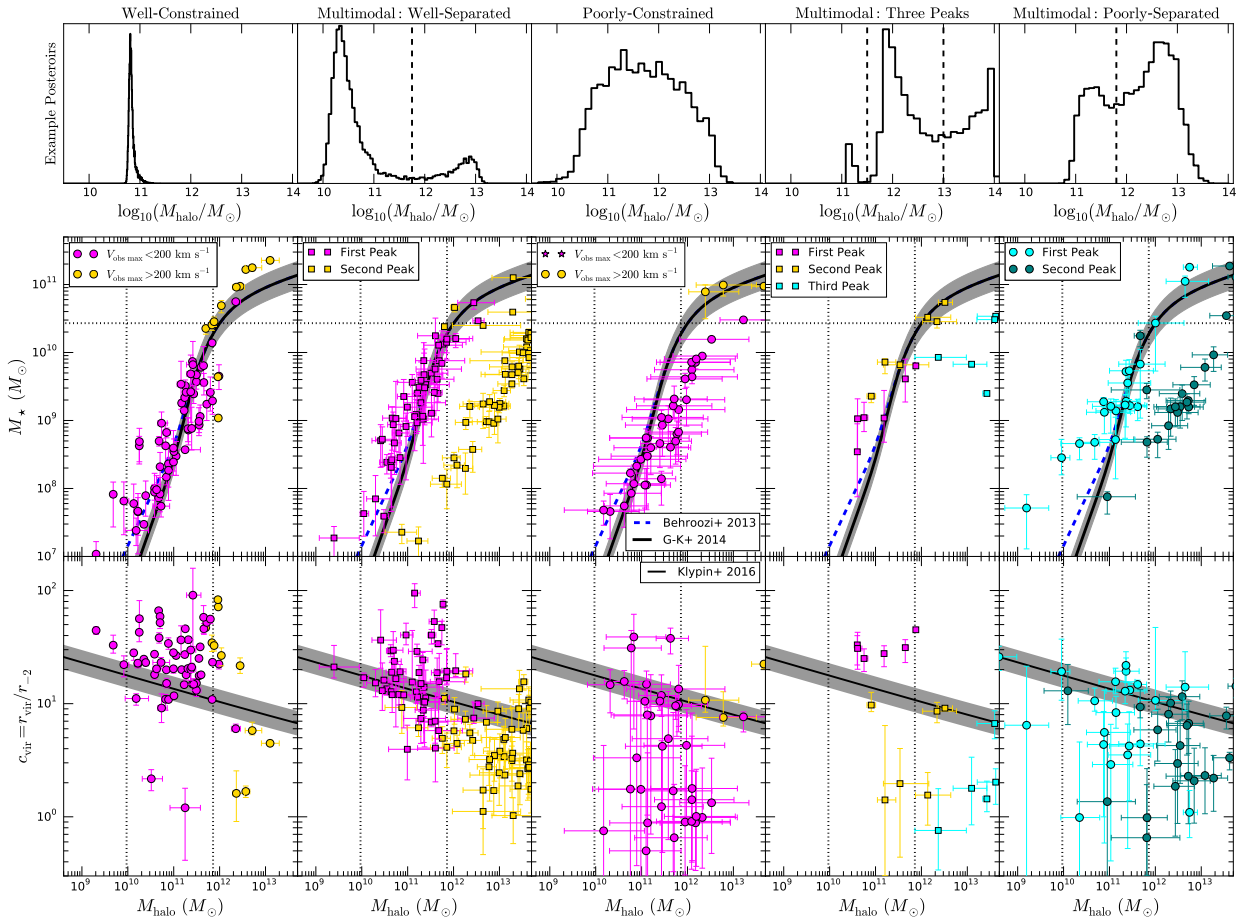

Figure 4.9: Same as Figure 4.4 but with a larger prior range on $\Upsilon_{\rm kinematic}$. There is an additional column for multimodal systems with distinct modes in the $M_{\rm halo}$ posterior.

in Figure 4.9 to show the three mode $M_{\rm halo}$ systems.

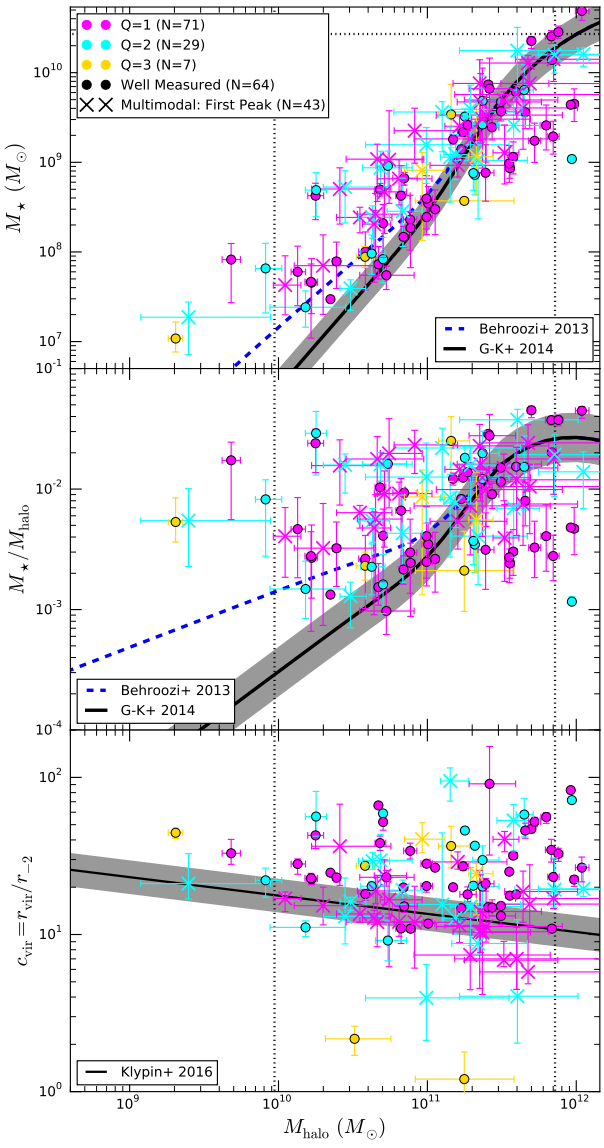

Figure 4.10: Same as Figure 4.5 but with a larger prior range on $\Upsilon_{\rm kinematic}$.

Chapter 5

Conclusion

The nature of dark matter is a one of major mysteries of modern astronomy and astrophysics. We have presented two new techniques to characterize the kinematics in dark matter dominated systems and an analysis to understand the distribution of dark matter in rotation curves.

The Bayesian object detection technique, presented in Chapter 2, uncovers localized substructure. Two substructures are detected at high significance in the dwarf spheroidal galaxy Ursa Minor. These are potential stellar systems or dark matter sub-subhalos. Either interpretation advances our understanding of dark matter.

The dynamics of multiple stellar populations in dwarf spheroidal galaxies can be utilized to uncover the mass slope. In Chapter 3, we presented an analysis to disentangle multiple stellar populations in dispersion supported systems. We introduced a novel method to remove Milky Way background stars. We uncovered two multiple stellar populations at high significance but found the mass slope to be inconsistent with dynamical equilibrium. The Ursa Minor analysis suffers from several systematics but the methodology can be applied to other systems.

In Chapter 4, we presented an compilation of literature rotation curves and an analysis with a

baryon influenced halo profile. We found that the rotation curves are well explained with this halo profile but the resulting halos do not follow well motivated cosmological relations. This suggests either the baryon influenced halo profile is incorrect or there is dark matter physics unaccounted for.

The work we have presented has increased our understanding of the kinematics in the Ursa Minor dwarf spheroidal galaxy and why dwarf and spiral galaxies contain dark matter cores. These new techniques will be key in the dynamical modeling of dwarf spheroidal as new and larger kinematic data sets are created.

Bibliography

Aaronson M., Olszewski E. W., 1987, AJ, 94, 657

Abazajian K. N., 2014, Physical Review Letters, 112, 161303

Abazajian K. N., et al., 2009, ApJS, 182, 543

Adams J. J., et al., 2014, ApJ, 789, 63

Agarwal S., Corasaniti P.-S., Das S., Rasera Y., 2015, Phys. Rev. D, 92, 063502

Agnello A., Evans N. W., 2012, ApJ, 754, L39

Ahn C. P., et al., 2012, ApJS, 203, 21

Aihara H., et al., 2011a, ApJS, 193, 29

Aihara H., et al., 2011b, ApJS, 195, 26

Akaike H., 1974, Automatic Control, IEEE Transactions on, 19, 716

Amorisco N. C., Evans N. W., 2012a, MNRAS, 419, 184

Amorisco N. C., Evans N. W., 2012b, MNRAS, 419, 184

Amorisco N. C., Evans N. W., 2012c, ApJ, 756, L2

Amorisco N. C., Agnello A., Evans N. W., 2013, MNRAS, 429, L89

Armandroff T. E., Olszewski E. W., Pryor C., 1995, AJ, 110, 2131

Arraki K. S., Klypin A., More S., Trujillo-Gomez S., 2014, MNRAS, 438, 1466

Astropy Collaboration et al., 2013, A&A, 558, A33

Battaglia G., et al., 2006a, A&A, 459, 423

Battaglia G., et al., 2006b, A&A, 459, 423

Battaglia G., Helmi A., Tolstoy E., Irwin M., Hill V., Jablonka P., 2008a, ApJ, 681, L13

Battaglia G., Helmi A., Tolstoy E., Irwin M., Hill V., Jablonka P., 2008b, ApJ, 681, L13

Battaglia G., Tolstoy E., Helmi A., Irwin M., Parisi P., Hill V., Jablonka P., 2011a, MNRAS, 411, 1013

Battaglia G., Tolstoy E., Helmi A., Irwin M., Parisi P., Hill V., Jablonka P., 2011b, MNRAS, 411, 1013

Begeman K. G., 1987, PhD thesis, , Kapteyn Institute, (1987)

Behroozi P. S., Wechsler R. H., Conroy C., 2013, ApJ, 770, 57

Bell E. F., de Jong R. S., 2001, ApJ, 550, 212

Bellazzini M., Ferraro F. R., Pancino E., 2001, MNRAS, 327, L15

Bellazzini M., Ferraro F. R., Origlia L., Pancino E., Monaco L., Oliva E., 2002a, AJ, 124, 3222

Bellazzini M., Ferraro F. R., Origlia L., Pancino E., Monaco L., Oliva E., 2002b, AJ, 124, 3222

Benson A. J., Cole S., Frenk C. S., Baugh C. M., Lacey C. G., 2000, MNRAS, 311, 793

Berlind A. A., Weinberg D. H., 2002, ApJ, 575, 587

Binney J., Mamon G. A., 1982, MNRAS, 200, 361

Binney J., Tremaine S., 2008, Galactic Dynamics: Second Edition. Princeton University Press

Blais-Ouellette S., Carignan C., Amram P., Côté S., 1999, AJ, 118, 2123

Blais-Ouellette S., Amram P., Carignan C., 2001, AJ, 121, 1952

Blais-Ouellette S., Amram P., Carignan C., Swaters R., 2004, A&A, 420, 147

Blumenthal G. R., Faber S. M., Primack J. R., Rees M. J., 1984, Nature, 311, 517

Blumenthal G. R., Faber S. M., Flores R., Primack J. R., 1986, ApJ, 301, 27

Bottema R., 2002, A&A, 388, 809

Bottema R., Pestaña J. L. G., 2015, MNRAS, 448, 2566

Bottema R., Verheijen M. A. W., 2002, A&A, 388, 793

Boylan-Kolchin M., Bullock J. S., Kaplinghat M., 2011a, MNRAS, 415, L40

Boylan-Kolchin M., Bullock J. S., Kaplinghat M., 2011b, MNRAS, 415, L40

Boylan-Kolchin M., Bullock J. S., Kaplinghat M., 2012a, MNRAS, 422, 1203

Boylan-Kolchin M., Bullock J. S., Kaplinghat M., 2012b, MNRAS, 422, 1203

Breddels M. A., Helmi A., 2013, A&A, 558, A35

Brook C. B., 2015, MNRAS, 454, 1719

Brook C. B., Di Cintio A., 2015a, MNRAS, 450, 3920

Brook C. B., Di Cintio A., 2015b, MNRAS, 453, 2133

Brook C. B., Di Cintio A., Knebe A., Gottlöber S., Hoffman Y., Yepes G., Garrison-Kimmel S., 2014, ApJ, 784, L14

Brooks A. M., Zolotov A., 2014, ApJ, 786, 87

Brooks A. M., et al., 2011, ApJ, 728, 51

Brooks A. M., Kuhlen M., Zolotov A., Hooper D., 2013, ApJ, 765, 22

Bryan G. L., Norman M. L., 1998, ApJ, 495, 80

Bullock J. S., Kolatt T. S., Sigad Y., Somerville R. S., Kravtsov A. V., Klypin A. A., Primack J. R., Dekel A., 2001, MNRAS, 321, 559

Bullock J. S., Wechsler R. H., Somerville R. S., 2002, MNRAS, 329, 246

Buonanno R., Corsi C. E., Castellani M., Marconi G., Fusi Pecci F., Zinn R., 1999, AJ, 118, 1671

Burkert A., 1995, ApJ, 447, L25

Campbell D. J. R., et al., 2016, preprint, (arXiv:1603.04443)

Caputo F., Cassisi S., Castellani M., Marconi G., Santolamazza P., 1999, AJ, 117, 2199

Carignan C., Puche D., 1990, AJ, 100, 641

Carignan C., Sancisi R., van Albada T. S., 1988, AJ, 95, 37

Carignan C., Frank B. S., Hess K. M., Lucero D. M., Randriamampandry T. H., Goedhart S., Passmoor S. S., 2013, AJ, 146, 48

Carrera R., Aparicio A., Martínez-Delgado D., Alonso-García J., 2002, AJ, 123, 3199

Cautun M., Frenk C. S., van de Weygaert R., Hellwing W. A., Jones B. J. T., 2014, MNRAS, 445, 2049

Chan T. K., Kereš D., Oñorbe J., Hopkins P. F., Muratov A. L., Faucher-Giguère C.-A., Quataert E., 2015, MNRAS, 454, 2981

Chemin L., Carignan C., Drouin N., Freeman K. C., 2006, AJ, 132, 2527

Christensen C., Quinn T., Governato F., Stilp A., Shen S., Wadsley J., 2012, MNRAS, 425, 3058

Christensen C. R., Brooks A. M., Fisher D. B., Governato F., McCleary J., Quinn T. R., Shen S., Wadsley J., 2014, MNRAS, 440, L51

Cole D. R., Dehnen W., Wilkinson M. I., 2011, MNRAS, 416, 1118

Cole D. R., Dehnen W., Read J. I., Wilkinson M. I., 2012, preprint, (arXiv:1205.6327)

Conroy C., Wechsler R. H., Kravtsov A. V., 2006, ApJ, 647, 201

Cooper M. C., Newman J. A., Davis M., Finkbeiner D. P., Gerke B. F., 2012, spec2d: DEEP2 DEIMOS Spectral Pipeline, Astrophysics Source Code Library (ascl:1203.003)

Corbelli E., Thilker D., Zibetti S., Giovanardi C., Salucci P., 2014, A&A, 572, A23

Côté S., Carignan C., Sancisi R., 1991, AJ, 102, 904

Côté S., Carignan C., Freeman K. C., 2000, AJ, 120, 3027

Courteau S., Dutton A. A., van den Bosch F. C., MacArthur L. A., Dekel A., McIntosh D. H., Dale D. A., 2007, ApJ, 671, 203

Cowsik R., Wagoner K., Berti E., Sircar A., 2009, ApJ, 699, 1389

Cui W., et al., 2016, MNRAS, 458, 4052

Dalcanton J. J., Stilp A. M., 2010, ApJ, 721, 547

Dalcanton J. J., et al., 2009, ApJS, 183, 67

Del Popolo A., Le Delliou M., 2014, J. Cosmology Astropart. Phys., 12, 051

Demarque P., Woo J.-H., Kim Y.-C., Yi S. K., 2004, ApJS, 155, 667

Demers S., Battinelli P., Irwin M. J., Kunkel W. E., 1995, MNRAS, 274, 491

Di Cintio A., Lelli F., 2016, MNRAS, 456, L127

Di Cintio A., Brook C. B., Macciò A. V., Stinson G. S., Knebe A., Dutton A. A., Wadsley J., 2014a, MNRAS, 437, 415

Di Cintio A., Brook C. B., Dutton A. A., Macciò A. V., Stinson G. S., Knebe A., 2014b, MNRAS, 441, 2986

Di Teodoro E. M., Fraternali F., 2015, MNRAS, 451, 3021

Diemand J., Kuhlen M., Madau P., 2007, ApJ, 667, 859

Diemand J., Kuhlen M., Madau P., Zemp M., Moore B., Potter D., Stadel J., 2008, Nature, 454, 735

Dotter A., Chaboyer B., Jevremović D., Baron E., Ferguson J. W., Sarajedini A., Anderson J., 2007, AJ, 134, 376

Dotter A., Chaboyer B., Jevremović D., Kostov V., Baron E., Ferguson J. W., 2008, ApJS, 178, 89

Dutton A. A., Macciò A. V., 2014, MNRAS, 441, 3359

Dutton A. A., Courteau S., de Jong R., Carignan C., 2005, ApJ, 619, 218

Dutton A. A., Macciò A. V., Stinson G. S., Gutcke T. A., Penzo C., Buck T., 2015, MNRAS, 453, 2447

El-Zant A., Shlosman I., Hoffman Y., 2001, ApJ, 560, 636

Elbert O. D., Bullock J. S., Garrison-Kimmel S., Rocha M., Oñorbe J., Peter A. H. G., 2015, MNRAS, 453, 29

Elson E. C., de Blok W. J. G., Kraan-Korteweg R. C., 2010, MNRAS, 404, 2061

Elson E. C., de Blok W. J. G., Kraan-Korteweg R. C., 2013, MNRAS, 429, 2550

Eskridge P. B., Schweitzer A. E., 2001, AJ, 122, 3106

Faber S. M., et al., 2003, in Iye M., Moorwood A. F. M., eds, Society of Photo-Optical Instrumentation Engineers (SPIE) Conference Series Vol. 4841, Instrument Design and Performance for Optical/Infrared Ground-based Telescopes. pp 1657–1669, doi:10.1117/12.460346

Fabrizio M., et al., 2015, A&A, 580, A18

Fabrizio M., et al., 2016, preprint, (arXiv:1607.03181)

Fathi K., Allen M., Boch T., Hatziminaoglou E., Peletier R. F., 2010, MNRAS, 406, 1595

Feast M. W., Thackeray A. D., Wesselink A. J., 1961, MNRAS, 122, 433

Feroz F., Hobson M. P., 2008, MNRAS, 384, 449

Feroz F., Hobson M. P., Bridges M., 2009, MNRAS, 398, 1601

Ferrero I., Abadi M. G., Navarro J. F., Sales L. V., Gurovich S., 2012, MNRAS, 425, 2817

Firmani C., D'Onghia E., Avila-Reese V., Chincarini G., Hernández X., 2000, MNRAS, 315, L29

Flores R. A., Primack J. R., 1994, ApJ, 427, L1

Fraternali F., Sancisi R., Kamphuis P., 2011, A&A, 531, A64

Frusciante N., Salucci P., Vernieri D., Cannon J. M., Elson E. C., 2012, MNRAS, 426, 751

Fry A. B., et al., 2015, MNRAS, 452, 1468

Garrison-Kimmel S., Boylan-Kolchin M., Bullock J. S., Lee K., 2014a, MNRAS, 438, 2578

Garrison-Kimmel S., Boylan-Kolchin M., Bullock J. S., Kirby E. N., 2014b, MNRAS, 444, 222

Garrison-Kimmel S., Boylan-Kolchin M., Bullock J. S., Kirby E. N., 2014c, MNRAS, 444, 222

Garrison-Kimmel S., Bullock J. S., Boylan-Kolchin M., Bardwell E., 2016, preprint, (arXiv:1603.04855)

Gentile G., Salucci P., Klein U., Vergani D., Kalberla P., 2004, MNRAS, 351, 903

Gentile G., Salucci P., Klein U., Granato G. L., 2007, MNRAS, 375, 199

Gentile G., Baes M., Famaey B., van Acoleyen K., 2010, MNRAS, 406, 2493

Ghosh J., Delampday M., Samanta T., 2006, An Introduction to Bayesian Analysis. Springer

Gilmore G., Wilkinson M. I., Wyse R. F. G., Kleyna J. T., Koch A., Evans N. W., Grebel E. K., 2007, ApJ, 663, 948

Girardi L., Grebel E. K., Odenkirchen M., Chiosi C., 2004, A&A, 422, 205

Gnedin O. Y., Zhao H., 2002, MNRAS, 333, 299

Gnedin O. Y., Kravtsov A. V., Klypin A. A., Nagai D., 2004, ApJ, 616, 16

Goerdt T., Moore B., Read J. I., Stadel J., Zemp M., 2006, MNRAS, 368, 1073

Gonzalez-Serrano J. I., Valentijn E. A., 1991, A&A, 242, 334

Governato F., Willman B., Mayer L., Brooks A., Stinson G., Valenzuela O., Wadsley J., Quinn T., 2007, MNRAS, 374, 1479

Governato F., et al., 2010, Nature, 463, 203

Governato F., et al., 2012, MNRAS, 422, 1231

Guedes J., Callegari S., Madau P., Mayer L., 2011, ApJ, 742, 76

Guo Q., White S., Li C., Boylan-Kolchin M., 2010, MNRAS, 404, 1111

Gustafsson M., Fairbairn M., Sommer-Larsen J., 2006, Phys. Rev. D, 74, 123522

Harbeck D., et al., 2001, AJ, 122, 3092

Hargreaves J. C., Gilmore G., Irwin M. J., Carter D., 1994, MNRAS, 271, 693

Hargreaves J. C., Gilmore G., Annan J. D., 1996, MNRAS, 279, 108

Hayashi E., et al., 2004, MNRAS, 355, 794

Hendricks B., Koch A., Walker M., Johnson C. I., Peñarrubia J., Gilmore G., 2014, A&A, 572, A82

Hernquist L., 1990, ApJ, 356, 359

Hlavacek-Larrondo J., Carignan C., Daigle O., de Denus-Baillargeon M.-M., Marcelin M., Epinat B., Hernandez O., 2011a, MNRAS, 411, 71

Hlavacek-Larrondo J., Marcelin M., Epinat B., Carignan C., de Denus-Baillargeon M.-M., Daigle O., Hernandez O., 2011b, MNRAS, 416, 509

Hobson M. P., McLachlan C., 2003, MNRAS, 338, 765

Hopkins P. F., Kereš D., Oñorbe J., Faucher-Giguère C.-A., Quataert E., Murray N., Bullock J. S., 2014, MNRAS, 445, 581

Horiuchi S., Bozek B., Abazajian K. N., Boylan-Kolchin M., Bullock J. S., Garrison-Kimmel S., Onorbe J., 2016, MNRAS, 456, 4346

Hunter J. D., 2007, Computing In Science & Engineering, 9, 90

Hunter D. A., Elmegreen B. G., 2006, ApJS, 162, 49

Hunter D. A., et al., 2012, AJ, 144, 134

Hurley-Keller D., Mateo M., Nemec J., 1998, AJ, 115, 1840

Ibata R., Chapman S., Irwin M., Lewis G., Martin N., 2006a, MNRAS, 373, L70

Ibata R., Chapman S., Irwin M., Lewis G., Martin N., 2006b, MNRAS, 373, L70

Irwin M., Hatzidimitriou D., 1995, MNRAS, 277, 1354

Jacobs B. A., Rizzi L., Tully R. B., Shaya E. J., Makarov D. I., Makarova L., 2009, AJ, 138, 332

Jaffe W., 1983, MNRAS, 202, 995

Jardel J. R., Gebhardt K., 2013, ApJ, 775, L30

Jardel J. R., Gebhardt K., Fabricius M. H., Drory N., Williams M. J., 2013, ApJ, 763, 91

Jiang F., van den Bosch F. C., 2015, MNRAS, 453, 3575

Jobin M., Carignan C., 1990, AJ, 100, 648

Jones E., Oliphant T., Peterson P., et al., 2001, SciPy: Open source scientific tools for Python, http://www.scipy.org/

Kam Z. S., Carignan C., Chemin L., Amram P., Epinat B., 2015, MNRAS, 449, 4048

Kaplinghat M., Strigari L. E., 2008, ApJ, 682, L93

Kaplinghat M., Keeley R. E., Linden T., Yu H.-B., 2014, Physical Review Letters, 113, 021302

Karachentsev I. D., Chengalur J. N., Tully R. B., Makarova L. N., Sharina M. E., Begum A., Rizzi L., 2015, preprint, (arXiv:1512.05907)

Karukes E. V., Salucci P., Gentile G., 2015, A&A, 578, A13

Kirby E. N., Guhathakurta P., Sneden C., 2008, ApJ, 682, 1217

Kirby E. N., et al., 2010, ApJS, 191, 352

Kirby E. N., Lanfranchi G. A., Simon J. D., Cohen J. G., Guhathakurta P., 2011, ApJ, 727, 78

Kirby E. N., Cohen J. G., Bellazzini M., 2012, ApJ, 751, 46

Kirby E. N., Bullock J. S., Boylan-Kolchin M., Kaplinghat M., Cohen J. G., 2014, MNRAS, 439, 1015

Kleyna J. T., Geller M. J., Kenyon S. J., Kurtz M. J., Thorstensen J. R., 1998, AJ, 115, 2359

Kleyna J. T., Wilkinson M. I., Gilmore G., Evans N. W., 2003, ApJ, 588, L21

Kleyna J. T., Wilkinson M. I., Evans N. W., Gilmore G., 2004, MNRAS, 354, L66

Klypin A. A., Trujillo-Gomez S., Primack J., 2011, ApJ, 740, 102

Klypin A., Karachentsev I., Makarov D., Nasonova O., 2015, MNRAS, 454, 1798

Klypin A., Yepes G., Gottlöber S., Prada F., Heß S., 2016, MNRAS, 457, 4340

Koch A., Grebel E. K., Wyse R. F. G., Kleyna J. T., Wilkinson M. I., Harbeck D. R., Gilmore G. F., Evans N. W., 2006, AJ, 131, 895

Koposov S. E., et al., 2011, ApJ, 736, 146

Kordopatis G., Amorisco N. C., Evans N. W., Gilmore G., Koposov S. E., 2016, MNRAS, 457, 1299

Kowalczyk K., Łokas E. L., Kazantzidis S., Mayer L., 2013, MNRAS, 431, 2796

Kravtsov A. V., Berlind A. A., Wechsler R. H., Klypin A. A., Gottlöber S., Allgood B., Primack J. R., 2004, ApJ, 609, 35

Kravtsov A., Vikhlinin A., Meshscheryakov A., 2014, preprint, (arXiv:1401.7329)

Kreckel K., Peebles P. J. E., van Gorkom J. H., van de Weygaert R., van der Hulst J. M., 2011, AJ, 141, 204

Kregel M., van der Kruit P. C., de Grijs R., 2002, MNRAS, 334, 646

Kuhlen M., Diemand J., Madau P., 2008, ApJ, 686, 262

Kullback S., Leibler R. A., 1951, The Annals of Mathematical Statistics, 22, pp. 79

Kuzio de Naray R., Kaufmann T., 2011, MNRAS, 414, 3617

Kuzio de Naray R., McGaugh S. S., de Blok W. J. G., Bosma A., 2006, ApJS, 165, 461

Kuzio de Naray R., McGaugh S. S., de Blok W. J. G., 2008, ApJ, 676, 920

Lake G., Schommer R. A., van Gorkom J. H., 1990, AJ, 99, 547

Laporte C. F. P., Walker M. G., Peñarrubia J., 2013, MNRAS, 433, L54

Lee M. G., Yuk I.-S., Park H. S., Harris J., Zaritsky D., 2009, ApJ, 703, 692

Lelli F., Verheijen M., Fraternali F., Sancisi R., 2012, A&A, 544, A145

Lelli F., Verheijen M., Fraternali F., 2014a, MNRAS, 445, 1694

Lelli F., Verheijen M., Fraternali F., 2014b, A&A, 566, A71

Liddle A. R., 2007, MNRAS, 377, L74

Liddle A., Mukherjee P., Parkinson D., 2006, Astronomy and Geophysics, 47, 040000

Łokas E. L., 2002, MNRAS, 333, 697

Lora V., Just A., Sanchez-Salcedo F. J., Grebel E. K., 2012, preprint, (arXiv:1207.5681)

Lovell M. R., et al., 2012, MNRAS, 420, 2318

Lovell M. R., Frenk C. S., Eke V. R., Jenkins A., Gao L., Theuns T., 2014, MNRAS, 439, 300

Lucero D. M., Carignan C., Elson E. C., Randriamampandry T. H., Jarrett T. H., Oosterloo T. A., Heald G. H., 2015, MNRAS, 450, 3935

Lyskova N., Thomas J., Churazov E., Tremaine S., Naab T., 2015, MNRAS, 450, 3442

Macciò A. V., Dutton A. A., van den Bosch F. C., Moore B., Potter D., Stadel J., 2007, MNRAS, 378, 55

Macciò A. V., Paduroiu S., Anderhalden D., Schneider A., Moore B., 2012a, MNRAS, 424, 1105

Macciò A. V., Stinson G., Brook C. B., Wadsley J., Couchman H. M. P., Shen S., Gibson B. K., Quinn T., 2012b, ApJ, 744, L9

Mackey A. D., Gilmore G. F., 2003, MNRAS, 340, 175

Madau P., Shen S., Governato F., 2014, ApJ, 789, L17

Makarov D., Prugniel P., Terekhova N., Courtois H., Vauglin I., 2014, A&A, 570, A13

Martin N. F., Ibata R. A., Chapman S. C., Irwin M., Lewis G. F., 2007, MNRAS, 380, 281

Martin N. F., de Jong J. T. A., Rix H.-W., 2008, ApJ, 684, 1075

Martinez G. D., Minor Q. E., Bullock J., Kaplinghat M., Simon J. D., Geha M., 2011, ApJ, 738, 55

Mashchenko S., Couchman H. M. P., Wadsley J., 2006, Nature, 442, 539

Mashchenko S., Wadsley J., Couchman H. M. P., 2008, Science, 319, 174

Mateo M. L., 1998, ARA&A, 36, 435

Mayer L., Governato F., Colpi M., Moore B., Quinn T., Wadsley J., Stadel J., Lake G., 2001a, ApJ, 547, L123

Mayer L., Governato F., Colpi M., Moore B., Quinn T., Wadsley J., Stadel J., Lake G., 2001b, ApJ, 559, 754

McConnachie A. W., 2012, AJ, 144, 4

McConnachie A. W., Côté P., 2010, ApJ, 722, L209

McGaugh S. S., Rubin V. C., de Blok W. J. G., 2001, AJ, 122, 2381

McGaugh S. S., de Blok W. J. G., Schombert J. M., Kuzio de Naray R., Kim J. H., 2007, ApJ, 659, 149

Merrifield M. R., Kent S. M., 1990, AJ, 99, 1548

Merritt D., 1987, ApJ, 313, 121

Merritt D., Graham A. W., Moore B., Diemand J., Terzić B., 2006, AJ, 132, 2685

Miller S. H., Ellis R. S., Newman A. B., Benson A., 2014, ApJ, 782, 115

Minor Q. E., Martinez G., Bullock J., Kaplinghat M., Trainor R., 2010, ApJ, 721, 1142

Mo H. J., Mao S., 2004, MNRAS, 353, 829

Moore B., 1994, Nature, 370, 629

Moster B. P., Somerville R. S., Maulbetsch C., van den Bosch F. C., Macciò A. V., Naab T., Oser L., 2010, ApJ, 710, 903

Moster B. P., Naab T., White S. D. M., 2013, MNRAS, 428, 3121

Muñoz R. R., et al., 2005a, ApJ, 631, L137

Muñoz R. R., et al., 2005b, ApJ, 631, L137

Muñoz R. R., Carlin J. L., Frinchaboy P. M., Nidever D. L., Majewski S. R., Patterson R. J., 2006, ApJ, 650, L51

Munshi F., et al., 2013, ApJ, 766, 56

Navarro J. F., Eke V. R., Frenk C. S., 1996a, MNRAS, 283, L72

Navarro J. F., Frenk C. S., White S. D. M., 1996b, ApJ, 462, 563

Navarro J. F., Frenk C. S., White S. D. M., 1997, ApJ, 490, 493

Navarro J. F., et al., 2010, MNRAS, 402, 21

Newman J. A., et al., 2013a, ApJS, 208, 5

Newman A. B., Treu T., Ellis R. S., Sand D. J., Nipoti C., Richard J., Jullo E., 2013b, ApJ, 765, 24

Newman A. B., Treu T., Ellis R. S., Sand D. J., 2013c, ApJ, 765, 25

Nipoti C., Binney J., 2015, MNRAS, 446, 1820

Noordermeer E., van der Hulst J. M., Sancisi R., Swaters R. A., van Albada T. S., 2005, A&A, 442, 137

Oñorbe J., Boylan-Kolchin M., Bullock J. S., Hopkins P. F., Kereš D., Faucher-Giguère C.-A., Quataert E., Murray N., 2015, MNRAS, 454, 2092

Oh K. S., Lin D. N. C., Richer H. B., 2000, ApJ, 531, 727

Oh S.-H., de Blok W. J. G., Walter F., Brinks E., Kennicutt Jr. R. C., 2008, AJ, 136, 2761

Oh S.-H., de Blok W. J. G., Brinks E., Walter F., Kennicutt Jr. R. C., 2011a, AJ, 141, 193

Oh S.-H., Brook C., Governato F., Brinks E., Mayer L., de Blok W. J. G., Brooks A., Walter F., 2011b, AJ, 142, 24

Oh S.-H., et al., 2015, AJ, 149, 180

Olszewski E. W., Aaronson M., 1985, AJ, 90, 2221

Olszewski E. W., Pryor C., Armandroff T. E., 1996, AJ, 111, 750

Oman K. A., et al., 2015, MNRAS, 452, 3650

Oman K. A., Navarro J. F., Sales L. V., Fattahi A., Frenk C. S., Sawala T., Schaller M., White S. D. M., 2016, preprint, (arXiv:1601.01026)

Pace A. B., 2016, preprint, (arXiv:1605.05326)

Pace A. B., Martinez G. D., Kaplinghat M., Muñoz R. R., 2014, MNRAS, 442, 1718

Palma C., Majewski S. R., Siegel M. H., Patterson R. J., Ostheimer J. C., Link R., 2003a, AJ, 125, 1352

Palma C., Majewski S. R., Siegel M. H., Patterson R. J., Ostheimer J. C., Link R., 2003b, AJ, 125, 1352

Papastergis E., Shankar F., 2015, preprint, (arXiv:1511.08741)

Papastergis E., Giovanelli R., Haynes M. P., Shankar F., 2015, A&A, 574, A113

Peacock J. A., Smith R. E., 2000, MNRAS, 318, 1144

Percival W. J., et al., 2001, MNRAS, 327, 1297

Pérez F., Granger B. E., 2007, Computing in Science and Engineering, 9, 21

Piatek S., Pryor C., Bristow P., Olszewski E. W., Harris H. C., Mateo M., Minniti D., Tinney C. G., 2005, AJ, 130, 95

Pineda J. C. B., Hayward C. C., Springel V., Mendes de Oliveira C., 2016, preprint, (arXiv:1602.07690)

Piontek F., Steinmetz M., 2011, MNRAS, 410, 2625

Planck Collaboration et al., 2015, preprint, (arXiv:1502.01589)

Plummer H. C., 1911, MNRAS, 71, 460

Pontzen A., Governato F., 2012, MNRAS, 421, 3464

Puche D., Carignan C., Bosma A., 1990, AJ, 100, 1468

Puche D., Carignan C., Wainscoat R. J., 1991a, AJ, 101, 447

Puche D., Carignan C., van Gorkom J. H., 1991b, AJ, 101, 456

Purcell C. W., Zentner A. R., 2012, J. Cosmology Astropart. Phys., 12, 007

Randriamampandry T., Combes F., Carignan C., Deg N., 2015, preprint, (arXiv:1509.04881)

Read J. I., Gilmore G., 2005, MNRAS, 356, 107

Read J. I., Agertz O., Collins M. L. M., 2015, preprint, (arXiv:1508.04143)

Read J. I., Iorio G., Agertz O., Fraternali F., 2016, preprint, (arXiv:1601.05821)

Reddick R. M., Wechsler R. H., Tinker J. L., Behroozi P. S., 2013, ApJ, 771, 30

Repetto P., Martínez-García E. E., Rosado M., Gabbasov R., 2015, MNRAS, 451, 353

Rhee G., Valenzuela O., Klypin A., Holtzman J., Moorthy B., 2004, ApJ, 617, 1059

Richards E. E., et al., 2015, MNRAS, 449, 3981

Richardson T., Fairbairn M., 2013, MNRAS, 432, 3361

Richardson T., Fairbairn M., 2014, MNRAS, 441, 1584

Richardson T. D., Spolyar D., Lehnert M. D., 2014, MNRAS, 440, 1680

Robertson B., Yoshida N., Springel V., Hernquist L., 2004, ApJ, 606, 32

Robin A. C., Reylé C., Derrière S., Picaud S., 2003, A&A, 409, 523

Robles V. H., Matos T., 2013, ApJ, 763, 19

Robles V. H., Lora V., Matos T., Sánchez-Salcedo F. J., 2015, ApJ, 810, 99

Rocha M., Peter A. H. G., Bullock J. S., 2011, preprint, (arXiv:1110.0464)

Rocha M., Peter A. H. G., Bullock J. S., Kaplinghat M., Garrison-Kimmel S., Oñorbe J., Moustakas L. A., 2013, MNRAS, 430, 81

Romano-Díaz E., Shlosman I., Hoffman Y., Heller C., 2008, ApJ, 685, L105

Ryden B. S., Gunn J. E., 1987, ApJ, 318, 15

Sales L. V., et al., 2015, MNRAS, 447, L6

Sales L. V., et al., 2016, preprint, (arXiv:1602.02155)

Salucci P., Burkert A., 2000, ApJ, 537, L9

Sánchez-Salcedo F. J., Reyes-Iturbide J., Hernandez X., 2006, MNRAS, 370, 1829

Sancisi R., Allen R. J., 1979, A&A, 74, 73

Sanders R. H., Verheijen M. A. W., 1998, ApJ, 503, 97

Sawala T., et al., 2016, MNRAS, 457, 1931

Schaller M., et al., 2015a, MNRAS, 451, 1247

Schaller M., et al., 2015b, MNRAS, 452, 343

Schaye J., et al., 2015, MNRAS, 446, 521

Schive H.-Y., Liao M.-H., Woo T.-P., Wong S.-K., Chiueh T., Broadhurst T., Hwang W.-Y. P., 2014, Physical Review Letters, 113, 261302

Shaw L. D., Weller J., Ostriker J. P., Bode P., 2007, ApJ, 659, 1082

Shetrone M. D., Bolte M., Stetson P. B., 1998, AJ, 115, 1888

Simon J. D., Geha M., 2007a, ApJ, 670, 313

Simon J. D., Geha M., 2007b, ApJ, 670, 313

Simon J. D., Bolatto A. D., Leroy A., Blitz L., Gates E. L., 2005, ApJ, 621, 757

Simon J. D., et al., 2011, ApJ, 733, 46

Skilling J., 2004a, in Fischer R., Preuss R., Toussaint U. V., eds, American Institute of Physics Conference Series. pp 395–405, doi:10.1063/1.1835238, http://www.inference.phy.cam.ac.uk/bayesys/

Skilling J., 2004b, in Fischer R., Preuss R., Toussaint U. V., eds, American Institute of Physics Conference Series Vol. 735, American Institute of Physics Conference Series. pp 395–405, doi:10.1063/1.1835238

Slater C. T., Bell E. F., Martin N. F., Tollerud E. J., Ho N., 2015, ApJ, 806, 230

Smecker-Hane T. A., Stetson P. B., Hesser J. E., Lehnert M. D., 1994, AJ, 108, 507

Snyder G. F., et al., 2015, MNRAS, 454, 1886

Sorce J. G., Tully R. B., Courtois H. M., Jarrett T. H., Neill J. D., Shaya E. J., 2014, MNRAS, 444, 527

Spekkens K., Sellwood J. A., 2007, ApJ, 664, 204

Spekkens K., Giovanelli R., Haynes M. P., 2005, AJ, 129, 2119

Spergel D. N., Steinhardt P. J., 2000, Physical Review Letters, 84, 3760

Spiegelhalter D. J., Best N. G., Carlin B. P., Van Der Linde A., 2002, Journal of the Royal Statistical Society: Series B (Statistical Methodology), 64, 583

Springel V., et al., 2008, MNRAS, 391, 1685

Stadel J., Potter D., Moore B., Diemand J., Madau P., Zemp M., Kuhlen M., Quilis V., 2009, MNRAS, 398, L21

Stinson G. S., Bailin J., Couchman H., Wadsley J., Shen S., Nickerson S., Brook C., Quinn T., 2010, MNRAS, 408, 812

Stinson G. S., Brook C., Macciò A. V., Wadsley J., Quinn T. R., Couchman H. M. P., 2013, MNRAS, 428, 129

Strigari L. E., Bullock J. S., Kaplinghat M., Kravtsov A. V., Gnedin O. Y., Abazajian K., Klypin A. A., 2006, ApJ, 652, 306

Strigari L. E., Koushiappas S. M., Bullock J. S., Kaplinghat M., 2007, Phys. Rev. D, 75, 083526

Strigari L. E., Frenk C. S., White S. D. M., 2014, preprint, (arXiv:1406.6079)

Swaters R. A., Balcells M., 2002, A&A, 390, 863

Swaters R. A., van Albada T. S., van der Hulst J. M., Sancisi R., 2002, A&A, 390, 829

Swaters R. A., Madore B. F., van den Bosch F. C., Balcells M., 2003, ApJ, 583, 732

Swaters R. A., Sancisi R., van Albada T. S., van der Hulst J. M., 2009, A&A, 493, 871

Takeuchi T. T., 2000, Ap&SS, 271, 213

Teyssier R., Pontzen A., Dubois Y., Read J. I., 2013, MNRAS, 429, 3068

Tissera P. B., Dominguez-Tenreiro R., 1998, MNRAS, 297, 177

Tollerud E. J., Boylan-Kolchin M., Bullock J. S., 2014, MNRAS, 440, 3511

Tollet E., et al., 2016, MNRAS, 456, 3542

Tolstoy E., Irwin M. J., Cole A. A., Pasquini L., Gilmozzi R., Gallagher J. S., 2001, MNRAS, 327, 918

Tolstoy E., et al., 2004, ApJ, 617, L119

Tonini C., Lapi A., Salucci P., 2006, ApJ, 649, 591

Tonry J., Davis M., 1979, AJ, 84, 1511

Trachternach C., de Blok W. J. G., Walter F., Brinks E., Kennicutt Jr. R. C., 2008, AJ, 136, 2720

Trentham N., Tully R. B., Verheijen M. A. W., 2001, MNRAS, 325, 385

Trotta R., 2008, Contemporary Physics, 49, 71

Tully R. B., Verheijen M. A. W., 1997, ApJ, 484, 145

Tully R. B., Verheijen M. A. W., Pierce M. J., Huang J.-S., Wainscoat R. J., 1996, AJ, 112, 2471

Tully R. B., Shaya E. J., Karachentsev I. D., Courtois H. M., Kocevski D. D., Rizzi L., Peel A., 2008, ApJ, 676, 184

Ural U., et al., 2010a, MNRAS, 402, 1357

Ural U., et al., 2010b, MNRAS, 402, 1357

Vale A., Ostriker J. P., 2004, MNRAS, 353, 189

Vale A., Ostriker J. P., 2006, MNRAS, 371, 1173

Valenzuela O., Rhee G., Klypin A., Governato F., Stinson G., Quinn T., Wadsley J., 2007, ApJ, 657, 773

Verdes-Montenegro L., Bosma A., Athanassoula E., 1995, A&A, 300, 65

Verheijen M. A. W., 2001, ApJ, 563, 694

Verheijen M. A. W., Sancisi R., 2001, A&A, 370, 765

Vogelsberger M., et al., 2014a, MNRAS, 444, 1518

Vogelsberger M., Zavala J., Simpson C., Jenkins A., 2014b, MNRAS, 444, 3684

Walker M. G., Peñarrubia J., 2011a, ApJ, 742, 20

Walker M. G., Peñarrubia J., 2011b, ApJ, 742, 20

Walker M. G., Mateo M., Olszewski E. W., Pal J. K., Sen B., Woodroofe M., 2006, ApJ, 642, L41

Walker M. G., Mateo M., Olszewski E. W., Gnedin O. Y., Wang X., Sen B., Woodroofe M., 2007, ApJ, 667, L53

Walker M. G., Mateo M., Olszewski E. W., 2008, ApJ, 688, L75

Walker M. G., Mateo M., Olszewski E. W., Sen B., Woodroofe M., 2009a, AJ, 137, 3109

Walker M. G., Mateo M., Olszewski E. W., Peñarrubia J., Wyn Evans N., Gilmore G., 2009b, ApJ, 704, 1274

Walker M. G., Mateo M., Olszewski E. W., Peñarrubia J., Wyn Evans N., Gilmore G., 2009c, ApJ, 704, 1274

Walt S. v. d., Colbert S. C., Varoquaux G., 2011, Computing in Science & Engineering, 13, 22

Walter F., et al., 2007, ApJ, 661, 102

Walter F., Brinks E., de Blok W. J. G., Bigiel F., Kennicutt Jr. R. C., Thornley M. D., Leroy A., 2008, AJ, 136, 2563

Wang X., Woodroofe M., Walker M. G., Mateo M., Olszewski E., 2005, ApJ, 626, 145

Wang M.-Y., Peter A. H. G., Strigari L. E., Zentner A. R., Arant B., Garrison-Kimmel S., Rocha M., 2014, MNRAS, 445, 614

Wang L., Dutton A. A., Stinson G. S., Macciò A. V., Penzo C., Kang X., Keller B. W., Wadsley J., 2015, MNRAS, 454, 83

Weiner B. J., Williams T. B., van Gorkom J. H., Sellwood J. A., 2001, ApJ, 546, 916

Weisz D. R., Dolphin A. E., Skillman E. D., Holtzman J., Gilbert K. M., Dalcanton J. J., Williams B. F., 2014, ApJ, 789, 147

Weldrake D. T. F., de Blok W. J. G., Walter F., 2003, MNRAS, 340, 12

Westmeier T., Braun R., Koribalski B. S., 2011, MNRAS, 410, 2217

Westmeier T., Koribalski B. S., Braun R., 2013, MNRAS, 434, 3511

Wetzel A. R., Hopkins P. F., Kim J.-h., Faucher-Giguere C.-A., Keres D., Quataert E., 2016, preprint, (arXiv:1602.05957)

White S. D. M., Rees M. J., 1978, MNRAS, 183, 341

Wilkinson M. I., Kleyna J., Evans N. W., Gilmore G., 2002, MNRAS, 330, 778

Wilkinson M. I., Kleyna J. T., Evans N. W., Gilmore G. F., Irwin M. J., Grebel E. K., 2004, ApJ, 611, L21

Wilkinson M. I., Kleyna J. T., Gilmore G. F., Evans N. W., Koch A., Grebel E. K., Wyse R. F. G., Harbeck D. R., 2006, The Messenger, 124, 25

Wolf J., Martinez G. D., Bullock J. S., Kaplinghat M., Geha M., Muñoz R. R., Simon J. D., Avedo F. F., 2010, MNRAS, 406, 1220

Yang X., Mo H. J., van den Bosch F. C., 2003, MNRAS, 339, 1057

Zhao D. H., Jing Y. P., Mo H. J., Börner G., 2009, ApJ, 707, 354

Zhu Q., Marinacci F., Maji M., Li Y., Springel V., Hernquist L., 2016, MNRAS, 458, 1559

Zolotov A., et al., 2012, ApJ, 761, 71

de Blok W. J. G., Bosma A., 2002, A&A, 385, 816

de Blok W. J. G., McGaugh S. S., 1997, MNRAS, 290, 533

de Blok W. J. G., McGaugh S. S., van der Hulst J. M., 1996, MNRAS, 283, 18

de Blok W. J. G., Walter F., Brinks E., Trachternach C., Oh S.-H., Kennicutt Jr. R. C., 2008, AJ, 136, 2648

van Zee L., Bryant J., 1999, AJ, 118, 2172

van den Bosch F. C., Robertson B. E., Dalcanton J. J., de Blok W. J. G., 2000, AJ, 119, 1579

van der Hulst J. M., Terlouw J. P., Begeman K. G., Zwitser W., Roelfsema P. R., 1992, in Worrall D. M., Biemesderfer C., Barnes J., eds, Astronomical Society of the Pacific Conference Series Vol. 25, Astronomical Data Analysis Software and Systems I. p. 131

van der Hulst J. M., Skillman E. D., Smith T. R., Bothun G. D., McGaugh S. S., de Blok W. J. G., 1993, AJ, 106, 548

van der Kruit P. C., Searle L., 1981, A&A, 95, 105